NUMERICAL SIMULATION OF CELL MOTION IN MICROCHANNELS

A Dissertation

Presented to

the Faculty of the Department of Mathematics

University of Houston

In Partial Fulfillment

of the Requirements for the Degree

Doctor of Philosophy

By

Lingling Shi

May 2013

NUMERICAL SIMULATION OF CELL MOTION IN MICROCHANNELS

Lingling Shi

APPROVED:

Dr. Tsorng-Whay Pan, Co-Chairman

Dr. Roland Glowinski, Co-Chairman

Dr. Jiwen He

Dr. Dong Liu
Department of Mechanical Engineering
University of Houston

Dr. Dan Wells
Interim Dean
College of Natural Sciences and Mathematics

... To Xiaochu, James, my parents, and sisters ...

Acknowledgements

First of all, I would like to express my deepest gratitude to my advisors, Dr. Tsorng-Whay Pan and Dr. Roland Glowinski for their guidance, advice, and financial support. I thank Dr. Pan for his patient when I made a slow progress, and the time he spent with me on the discussion of technical problems, as well as writing of papers and this dissertation. Numerical simulation was a new research area for me when I joined his group, but his direction, inspiration, and encouragement has helped me through and made this dissertation possible.

I thank fellow group members Xiting Niu, Yao Yu, and Shihai Zhao for insightful discussions and sharing their ideas and experience.

I thank my other committee members, Dr. Dong Liu, and Dr. Jiwen He for their time and helpful comments to improve my work. I also want to express my sincere thanks to Dr. Shanyu Ji for all kinds of his nice suggestions during my time at the Department of Mathematics.

Finally, I wish to express my warm and sincere thanks to my parents and my sisters for all their love and support at every stage of my life. I would like to thank my husband Xiaochu for his love, understanding and encouragement. He has been sharing the pressures and joys with me for the last few years. Without them, my accomplishments would not be possible.

NUMERICAL SIMULATION OF CELL MOTION IN MICROCHANNELS

An Abstract of a Dissertation

Presented to

the Faculty of the Department of Mathematics

University of Houston

In Partial Fulfillment

of the Requirements for the Degree

Doctor of Philosophy

By

Lingling Shi

May 2013

Abstract

An immersed boundary method combined with an elastic spring model is applied to simulate the red blood cell (RBC) motion and deformation in bounded Poiseuille flows. As a benchmarking test, the dynamical behavior of a RBC in shear flow is presented. The combined effects of the deformability, the degree of confinement, and the shear gradient of the Poiseuille flow make the RBCs migrate toward a certain cross-sectional equilibrium position, which lies at or off the center line. Two motions of oscillation and swing of RBCs are observed in the narrow channel. Parachute shape and bullet-like shape, depending on the initial angle, coexist for the elliptic shape cell with a low fluid velocity in a narrower channel. The details of the equilibrium shape and position versus the Reynolds number are investigated. Interactions of many cells in Poiseuille flows are studied to examine the size of the cell-free layer and Fahraeus-Lindqvist effect.

Contents

List of Figures

List of Tables

Chapter 1

Introduction

1.1 Motivation

The human blood is a complex non-homogeneous fluid which is composed of blood cells suspended in a liquid called blood plasma. The blood cells are mainly red blood cells (RBCs or erythrocytes), white blood cells (leukocytes), and platelets. The rheological property of the RBCs is a key factor of the blood flow characteristics in microvessels due to their large volume fraction (40%−45%), so-called hematocrit (Hct), in the whole blood. The normal RBC has a biconcave disk with a major diameter about 8 μm and thickness about 2 μm as its rest shape as shown in Figure 1.1. The mean volume is about 94 μm^3 and the average surface area of RBC is about 135 μm^2, a value greater than the surface area (97.12 μm^2) of a sphere with the same volume [12]. This excess area also contributes to RBC deformation. The RBC membrane composing of a lipid bilayer underlined by a spectrin network of

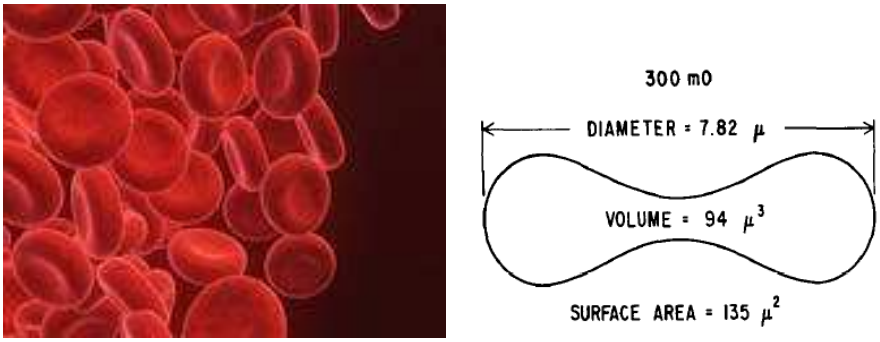

Figure 1.1: Healthy RBCs with its usual biconcave disk shape [30] (left) and the typical dimensions of the average RBC [26] (right).

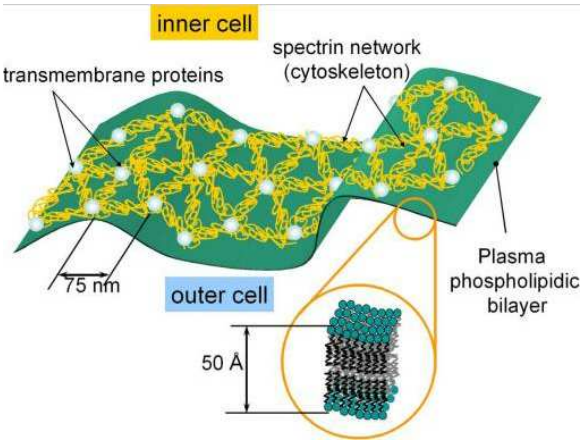

Figure 1.2: Artist's view of a RBC membrane. The cytoskeletal triangle mesh is embedded in the plasma phospholipid bilayer by the transmembrane proteins. The plasma layer (bilayer of amphifilic molecules) is believed to be responsible for the constraints of constant area and resistance to buckling. It can rearrange itself very easily, and is often referred to as a fluid membrane. The network of proteins attached underneath the plasma layer is responsible for the shear resistance (through molecular links between the proteins) and bending. The whole membrane also contains ionic pumps maintaining the inner volume of the RBC constant. ([24])

cytoskeletal proteins (see Figure 1.2) is highly deformable so that RBC can change its shape when an external force is acting on it and return to the biconcave resting shape after the removal of the force [29]. This deformability of the RBC membrane makes it can traverse 3 μm in diameter capillaries of the microcirculation. The motion and deformation of RBC have an important effect on both its physicological function in oxygen transport [92] and the hydrodynamical properties of normal human blood. Some diseases such as sickle cell anemia [23, 37, 59] and diabetes mellitus [90] are related to the RBCs with less deformability.

Starting from the pioneering work of Fahraeus and Lindqvist, the behavior of soft entities, such as capsules, vesicles and red blood cells under shear flow has been studied theoretically [28, 50, 53], experimentally [35], and numerically [8, 11, 20, 27, 39, 41, 42, 51, 56, 58, 61, 68, 85, 86, 94]. Three different types of motions have been observed for the vesicles and cells in shear flow: tank-treading (TT, the fluid membrane rotates as a tank tread while the orientation angle of the RBC remains fixed in time) [8, 25, 20, 27, 42, 50, 68], tumbling (TB, flipping motion like a rigid body behavior) [9, 39, 46, 58, 85], and vacillating-breathing (VB, the long axis undergoes oscillation about the flow while the shape shows breathing, called alternatively swing) [58, 61]. Motivated by the complex and interesting behavior of the vesicles and cells in shear flow, we focus more on exploring the complex dynamics of a single RBC and collective RBCs in Poiseuille flows in this dissertation.

Studying the dynamical behaviors (such as deformability, motion, equilibrium shape, equilibrium position, etc.) of RBCs suspended in Poiseuille flow is an essential and important problem in biomedical and biochemical industries. These studies may

serve as a useful and practical method in designing the cells separating microfluidic devices based on their mechanical properties such as size and deformability [63]. Many researchers in mathematics, physics and mechanics, biology, and medicine have studied this problem by using various entities, such as particles, drops, capsules, vesicles and RBCs theoretically [38, 40], experimentally [15, 34, 47, 48, 77, 78, 79], and numerically [15, 17, 22, 49, 53, 60, 74, 44, 45, 81, 82, 83, 93]. But most studies have been limited to the Stokes flow, or the cells are restricted to the sphere or ellipse. In this dissertation, we examine the deformable cell behavior in the flow with inertial effect, and the biconcave shape cell is also included.

Several numerical methods have been developed to study the cross-stream migration and the deformation of these entities in Poiseuille flows. Mortazavi *et al.* studied the cross-stream migration of a deformable drop in a Poiseuille flow at finite Reynolds numbers by using the finite difference and front tracking method and reported that the motion of the drop strongly depends on the viscosity ratio of the inside and outside fluids; For the viscosity ratio 1.0 it moves away from the the center until halted by the wall repulsion [60]. Pozrikidis studied the motion of spherical, oblate ellipsoidal, and biconcave capsules in tube flow by using the boundary element method and observed that spherical capsules slowly migrate to the tube center line, while oblate and biconcave capsules develop parachute and slipper shapes, respectively [74]. Kaoui *et al.* [44] studied the cross-stream noninertial migration of a suspended vesicle in an unbounded (Coupier *et al.* [15] studied the bounded case) Poiseuille flow at low Reynolds numbers by using the boundary integral method, and found that the vesicle deforms and migrates toward the center of the flow. Yoshino

et al. applied the lattice Boltzmann method to study the motion of a viscoelastic body in a Poiseuille flow and observed that the equilibrium position is very close to the center line for a low elasticity and it is at a certain position between the center line and the wall for a larger elasticity [93]. Danker *et al.* investigated the effect of viscosity ratio on the migration of vesicles in a Poiseuille flow by theoretical analysis, and predicted coexistence of two types of shapes: a bullet-like shape and a parachute-like shape [17]. Li *et al.* investigated the shape change and motion of the vesicle by using the lattice-Boltzmann method [53]. The asymmetric shape of the vesicle in an unbounded Poiseuille flow at zero Reynolds number was studied by Kaoui *et al.* [40].

In most of the above studies, the deformability of these entities was included, but no inertial effect on the cross-stream migration was considered. The effect of the inertia on the lateral motion of particles in a Poiseuille flow was first documented experimentally by Segré and Silberberg [78, 79]. They observed that rigid neutrally buoyant particles migrate away from both the wall and the center line, forming a concentrated layer at about half the distance between the wall and the center line. By using spherical particles and drops, Karnis *et al.* further studied this effect and found that the deformable drops migrate to the center line if their viscosity is low [47, 48]. The oscillatory motion for drops in pressure-driven channel flow at a finite Reynolds number by using the boundary integral method was examined by Mortazavi *et al.* [60]. Ko *et al.* investigated the migration and multiple equilibrium positions of a single particle in Poiseuille flows, and observed that the equilibrium height of a neutrally buoyant particle between the wall and the channel center line depends on

the Reynolds number [49]. Some theoretical studies of the effect of the inertia have been limited to spherical particles [38]. Recently, the inertial migration of an elastic capsule in a bounded Poiseuille flow at a finite Reynolds number was investigated by Shin [83]. But the initial shape of the capsule is limited to either a circle or an ellipse. For the circular initial shape, the equilibrium position can be either at the center of the channel or between the center and the wall (known as the Segré-Silberberg effect) depending on the Reynolds number and the ratio of the capsule size and the channel height. Noguchi *et al.* studied the shape transition of vesicles and RBCs in capillary flows by employing a three-dimensional mesoscopic simulation method and obtained the slipper shape of a RBC [62]. Doddi *et al.* studied the lateral migration of a three-dimensional deformable capsule in a Poiseuille flow based on a mixed finite-difference and Fourier transform method for the flow solver and a front-capsule method for the deformable interface and reported that the capsules without bending migrate toward the center line [22].

In this dissertation, inertial migration and equilibrium position and shape of a cell with different initial shape (convex and biconcave) in bounded two-dimensional Poiseuille flows have been studied by numerical simulation.

1.2 Research objective

The purpose of this dissertation is to investigate the rheological properties of RBCs in microvessels. To achieve this goal, an elastic spring model [89] is chosen to model the skeleton structure of a RBC membrane. An immersed boundary method

[69, 70, 71] combined with the elastic spring model is used to simulate the interaction between the cell and the fluid flow. An operator splitting technique [18, 32] is adopted to solve the fluid-cell system equations governed by the Navier-Stokes equations. The no-slip condition on the RBC membrane surface is enforced. Here are the main objectives of this dissertation:

(i) Validate the model and method by the comparison of the dynamical behavior of a single RBC in shear flow [81].

(ii) Investigate the lateral migration, deformation, and the equilibrium shape and position of a single RBC in bounded two-dimensional Poiseuille flows [81, 82].

(iii) Study the motion of many cells in Poiseuille flows, including the interaction of two kinds of cells, analyze the size of the cell-free layer, and the Fahraeus-Lindqvist effect [67, 80]. The motion of RBCs in a curved channel has been involved by using a fictitious domain method with distributed Lagrange multipliers (DLM/FD) [32, 65]. The effect of the boundary (straight or curve) on the size of the cell-free lay has been explored.

(iv) Perform the stretching force test for three-dimensional RBC membrane to tune the elastic parameters based on the comparison with the optical tweezers experimental data [57]. A coarse-grained model [72] is adopted to study the dynamics of a single RBC in three-dimensional microvessels and microfluidics.

1.3 Dissertation outline

This dissertation is devoted to investigating the motion and deformation of a single RBC and collective RBCs in microvessels and microfluidics by using numerical simulations.

In Chapter 2, we introduce the methodology used in this dissertation. An elastic spring model is chosen to model the skeleton structure of a RBC membrane. An immersed boundary method combined with the elastic spring model is applied to study the interaction between RBC and the fluid. An operator splitting technique is adopted to solve the fluid-cell system equations governed by the Navier-Stokes equations.

In Chapter 3, we validate the model and method by the comparisons of the steady inclination angles of the tank treading of a single RBC in a shear flow and analyze the effect of the viscosity ratio and the degree of confinement on the dynamical behavior of RBC in a shear flow.

In Chapter 4, we investigate the lateral migration and deformation of a single RBC in bounded two-dimensional Poiseuille flows. The combined effects of the deformability, the degree of confinement, and the shear gradient of the Poiseuille flow make the RBCs migrate toward a certain cross-sectional equilibrium position, which lies either on the center line of the channel or off the center line. Two motions of oscillation and vacillating breathing (swing) of RBCs are observed. Parachute shape and bullet-like shape, depending on the initial angle between the long axis of the cell and the horizontal direction, coexist for the elliptic shape cell with lower maximum

velocity of the fluid flow in a narrower channel. Many cells in Poiseuille flows, including the interaction of two kinds of cells, are performed for studying the size of the cell-free layer and the Fahraeus-Lindqvist effect. The circular shape cells have less deformability under the given bending property, they move to the region next to the walls and stay there just like neutrally buoyant particle. Rouleaux, red blood cells stack like coins, are observed in a very narrower channel when the force obtained from Morse potential function is adapted. The motion of RBCs in a curved channel has been investigated by combining the above methodology with a fictitious domain method with distributed Lagrange multipliers (DLM/FD). The boundary (straight or curve) has no effect on the size of the cell-free layer. Rouleaux, red blood cells stack like coins, are observed in a very narrower channel considered here.

In Chapter 5, we perform the stretching force test for three-dimensional RBC membrane to tune the elastic parameters based on the comparison with the optical tweezers experimental data and adopt a coarse-grained model to study the motion and deformability of a single RBC in three-dimensional microvessels and microfluids. A typical parachute shape is obtained in a narrow tube Poiseuille flow. Also the lateral migration and equilibrium shape and position of a single RBC in a slit Poiseuille flow has been studied. For the same cell parameters, the equilibrium shape depends on Re, and for the same Re, the change in the morphology depends on the membrane bending constant. The cell sets its equilibrium position between $0.5H$ and $0.6H$. The mass center of the equilibrium shape cell deviates away from the center line of the channel due to its asymmetric slipper shape.

In Chapter 6, we summarize our research and suggest future work.

Chapter 2

Methodology

An elastic spring network model is chosen to model the skeleton structure of RBC membrane. Such model combined with an immersed boundary method and finite element method is applied to study the RBC rheology in two-dimensional microchannels. The governing equations for the fluid-cell system are the Navier-Stokes equations

$$\rho\left(\frac{\partial \mathbf{u}}{\partial t} + \mathbf{u}\cdot\nabla\mathbf{u}\right) = -\nabla p + \nabla\cdot[\mu(\mathbf{x},t)2\mathbf{D}(\mathbf{u})] + \mathbf{f} \text{ in } \Omega\times(0,T), \tag{2.1}$$

$$\nabla\cdot\mathbf{u} = 0 \text{ in } \Omega\times(0,T). \tag{2.2}$$

Here the domain Ω is a bounded region filled with blood plasma which is incompressible, Newtonian, and contains RBC(s) (see Figure 2.1).

Equations (2.1) and (2.2) are completed by the following boundary and initial

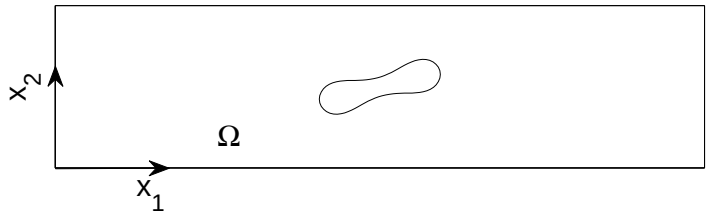

Figure 2.1: An example of computational domain with one RBC.

conditions:

$$\mathbf{u} = \mathbf{g} \text{ on the top and bottom of } \Omega$$
$$\text{and } \mathbf{u} \text{ is periodic in the } x_1 \text{ direction,} \tag{2.3}$$
$$\mathbf{u}(\mathbf{x}, 0) = \mathbf{u}_0(\mathbf{x}) \text{ in } \Omega. \tag{2.4}$$

where $\mathbf{u}$ and p are the fluid velocity and pressure, respectively, anywhere in the flow, ρ is the fluid density, and μ is the fluid viscosity. In equation (2.1), we have that $2\mathbf{D}(\mathbf{u}) = \nabla\mathbf{u} + (\nabla\mathbf{u})^t$, $\mathbf{f}$ is a body force which is the sum of $\mathbf{f}_p$ and $\mathbf{f}_B$, where $\mathbf{f}_p$ is the pressure gradient pointing in the x_1 direction and $\mathbf{f}_B$ accounts for the force acting on the fluid-cell interface which will be discussed in Section (2.2). In equation (2.4), $\mathbf{u}_0(\mathbf{x})$ is the initial fluid velocity. For the cases of shear flow, $\mathbf{f}_p$ is set to be zero. When considering Poiseuille flow, we set $\mathbf{g} = \mathbf{0}$.

2.1 Elastic spring model for the RBC membrane

A two-dimensional elastic spring model developed in [89] is adopted to describe the deformable behavior of the RBCs. Based on this model, the RBC membrane can be viewed as a network of particles connecting with the neighboring membrane particles by springs, as shown in Figure 2.2. Energy stores in the spring network due to the change of the length l of the spring with respect to its reference length l_0 and the change in angle θ between two neighboring springs. The total energy of the RBC membrane, $E = E_l + E_b$, is the sum of the total energy for stretch and compression and the total energy for the bending which, in particular, are

$$E_l = \frac{k_l}{2} \sum_{i=1}^{N} (\frac{l_i - l_0}{l_0})^2 \tag{2.5}$$

and

$$E_b = \frac{k_b}{2} \sum_{i=1}^{N} \tan^2(\frac{\theta_i}{2}). \tag{2.6}$$

In equations (2.5) and (2.6), N is the total number of the spring elements, and k_l and k_b are spring constants for changes in length and bending angle, respectively.

In the process of creating the initial shape of RBCs described in [89], the RBC is assumed to be a circle of radius $R_0 = 2.8$ μm initially. The circle is discretized into $N = 76$ membrane particles so that 76 springs are formed by connecting the neighboring particles. The shape change is stimulated by reducing the total area of the circle through a penalty function

$$\Gamma_s = \frac{k_s}{2} (\frac{s - s_e}{s_e})^2, \tag{2.7}$$

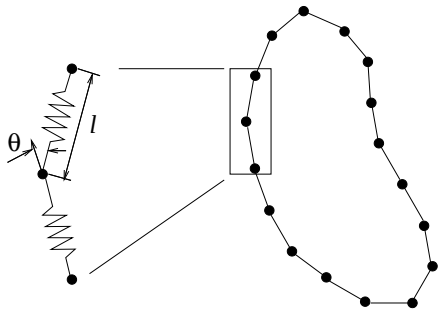

Figure 2.2: The elastic spring model of the two-dimensional RBC membrane.

where s and s_e are the time dependent area of the RBC and the equilibrium area of the RBC, respectively, and k_s is the penalty coefficient. Thus the total energy is modified as $E + \Gamma_s$. Based on the principle of virtual work the force acting on the ith membrane particle now is

$$\mathbf{F}_i = -\frac{\partial(E + \Gamma_s)}{\partial \mathbf{r}_i}, \tag{2.8}$$

where $\mathbf{r}_i$ is the position of the ith membrane particle. When the area is reduced, each RBC membrane particle moves on the basis of the following equation of motion:

$$m\ddot{\mathbf{r}}_i + \gamma\dot{\mathbf{r}}_i = \mathbf{F}_i. \tag{2.9}$$

Here, $\dot{(\,)}$ denotes the time derivative, and m and γ represent the membrane particle mass and the membrane viscosity of the RBC. The position $\mathbf{r}_i$ of the ith membrane particle is solved by discretizing equation (2.9) via a second order finite difference method. The total energy stored in the membrane decreases as the time elapses. The final shape of the RBC is obtained as the total energy is minimized [68]. The area of the final shape has less than 0.001% difference from the given equilibrium area s_e and the length of the perimeter of the final shape has less than 0.005% difference

from the circumference of the initial circle. The value of the swelling ratio of a RBC in this work is defined by $s^* = s_e/(\pi R_0^2)$.

2.2 Immersed boundary method

The immersed boundary method developed by Peskin, e.g., [69, 70, 71], is employed in this work because of its distinguishing features in dealing with the problem of fluid flow interacting with a flexible fluid-structure interface. Based on the method, the boundary of the deformable structure is discretized spatially into a set of boundary nodes. The force located at the immersed boundary node $\mathbf{X} = (X_1, X_2)$ affects the nearby fluid mesh nodes $\mathbf{x} = (x_1, x_2)$ through a two-dimensional discrete δ function $D_h(\mathbf{X} - \mathbf{x})$:

$$\mathbf{f}_B(\mathbf{x}) = \sum \mathbf{F}_i D_h(\mathbf{X}_i - \mathbf{x}) \quad \text{for } |\mathbf{X_i} - \mathbf{x}| \leq 2h, \tag{2.10}$$

where h is the uniform finite element mesh size and

$$D_h(\mathbf{X} - \mathbf{x}) = \delta_h(X_1 - x_1)\delta_h(X_2 - x_2) \tag{2.11}$$

with the one-dimensional discrete δ functions being

$$\delta_h(z) = \begin{cases} \frac{1}{8h}\left[3 - 2|z|/h + \sqrt{1 + 4|z|/h - 4(|z|/h)^2}\right], & |z| \leq h, \\ \frac{1}{8h}\left[5 - 2|z|/h - \sqrt{-7 + 12|z|/h - 4(|z|/h)^2}\right], & h \leq |z| \leq 2h, \\ 0, & \text{otherwise.} \end{cases} \tag{2.12}$$

The movement of the immersed boundary node $\mathbf{X}$ is also affected by the surrounding fluid and therefore is enforced by summing the velocities at the nearby

fluid mesh nodes $\mathbf{x}$ weighted by the same discrete δ function:

$$\mathbf{U}(\mathbf{X}) = \sum h^2 \mathbf{u}(\mathbf{x_j}) D_h(\mathbf{X} - \mathbf{x_j}) \quad \text{for } |\mathbf{X} - \mathbf{x_j}| \leq 2h. \tag{2.13}$$

After each time step, the position of the immersed boundary node is updated by

$$\mathbf{X}_{t+\Delta t} = \mathbf{X}_t + \Delta t \mathbf{U}(\mathbf{X}_t). \tag{2.14}$$

2.3 Intercellular interaction model

At lower shear rate, RBCs can aggregate and tend to obstruct the capillary entrance. With weak aggregation, RBCs form rouleaux, which look like stacks of coins. As the strength of aggregation is increased, RBCs clumps are formed which are more difficult to disrupt at the entrance to capillaries. In severe cases, these structures can increase the flow resistance and sometimes lead the formation of blood sludging [36]. To implement the simulation of rouleaux formation, we model the intercellular interaction energy by a Morse potential:

$$\phi(r) = D_e[e^{2\beta(r_0 - r)} - 2e^{\beta(r_0 - r)}], \tag{2.15}$$

where r is the surface separation, r_0 and D_e are the zero force separation and surface energy, respectively, and β is a scaling factor controlling the interaction decay behavior ([55]). Then the interaction force from the Morse potential can be obtained:

$$f(r) = -\frac{\partial \phi(r)}{\partial r} = 2D_e\beta[e^{2\beta(r_0 - r)} - e^{\beta(r_0 - r)}]. \tag{2.16}$$

The non-dimensionalized Morse potential and force are plotted in Figure 2.3.

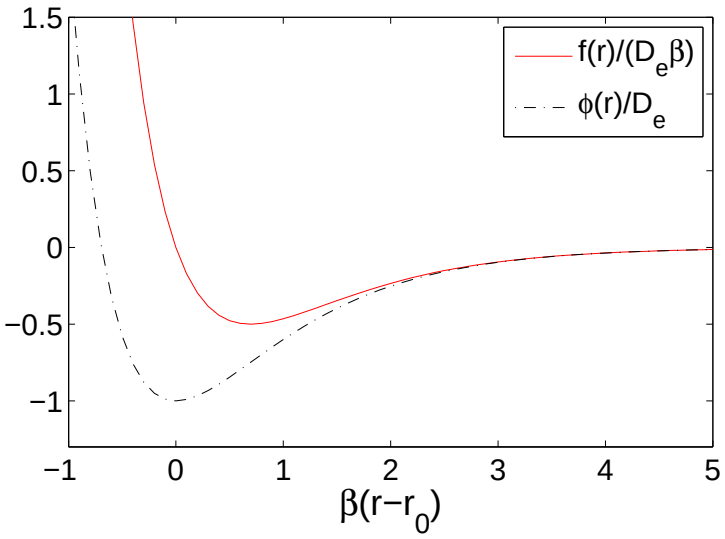

Figure 2.3: Non-dimensionalized Morse potential and force.

2.4 Viscosity function across the cell membrane

The fluids separated by the cell membrane can have different properties, such as viscosity and density. In the system considered in this dissertation, the densities of cytoplasm of RBC and plasma are same. But in some simulations, the viscosities of the cytoplasm of RBC and that of the suspending plasma are different. To describe this property, the viscosity is treated as a smoothing function instead of a piecewise constant function across the cell membrane [52, 96]. In this dissertation, we treat different viscosities when crossing the cell membrane via a Heaviside function [96]

defined as

$$\theta(d) = \begin{cases} 0, & d < -2h, \\ \frac{1}{2}(1 + \frac{d}{2h} + \frac{1}{\pi}\sin\frac{\pi d}{2h}), & -2h \le d \le 2h, \\ 1, & d > -2h, \end{cases} \tag{2.17}$$

where d denotes the index of a fluid node as the shortest distance to the cell membrane. If the node is close to two or more membrane segments, the index taken is that to the closest one. Then the viscosity function can be defined as:

$$\mu(\mathbf{x}) = \mu_{\text{out}} - (\mu_{\text{out}} - \mu_{\text{in}})\theta[d(\mathbf{x})], \tag{2.18}$$

where μ_{out} and μ_{in} are the viscosities outside and inside of the cell, respectively.

2.5 Operator splitting technique

We have applied the *Lie's Scheme* [14, 32] to equations (2.1) and (2.2) with the IBM and the backward Euler method in time for some subproblems and obtain the following fractional step subproblems:

$\mathbf{u}^0 = \mathbf{u}_0$ is given. For $n \ge 0, \mathbf{u}^n$ being known, we obtain $\mathbf{u}^{n+1}$ via:

(1) Solve

$$\begin{cases} \rho\dfrac{\mathbf{u}^{n+1/4} - \mathbf{u}^n}{\triangle t} + \nabla p^{n+1/4} = 0 \text{ in } \Omega \times (t^n, t^{n+1}), \\ \nabla \cdot \mathbf{u}^{n+1/4} = 0 \text{ in } \Omega \times (t^n, t^{n+1}), \\ \mathbf{u}^{n+1/4} = \mathbf{g}^{n+1} \text{ on the top and bottom of } \Omega \\ \text{ and is periodic in the } x_1 \text{ direction.} \end{cases} \tag{2.19}$$

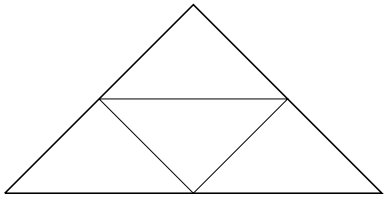

Figure 2.4: Schematic representation of a FEM triangulation and its subtriangulation.

(2) Update the position of the membrane based on $\mathbf{u}^{n+1/4}$ by (2.13) and (2.14) and then compute the force $\mathbf{f}_B$ on the fluid-cell interface by (2.8) and (2.10). Find the Heaviside function $\theta(d)$ (2.17) to define the viscosity function $\mu(\mathbf{x})$ (2.18).

(3) Solve

$$\begin{cases} \dfrac{\partial \mathbf{u}(t)}{\partial t} + (\mathbf{u}^{n+1/4} \cdot \nabla)\mathbf{u}(t) = 0 \text{ in } \Omega \times (t^n, t^{n+1}), \\ \mathbf{u}(t^n) = \mathbf{u}^{n+1/4} \text{ in } \Omega \times (t^n, t^{n+1}), \\ \mathbf{u}(t) = \mathbf{g}^{n+1} \text{ on } \Gamma_-^{n+1} \times (t^n, t^{n+1}), \end{cases} \tag{2.20}$$

here $\Gamma_-^{n+1} = \{\mathbf{x} | \mathbf{x} \in \partial\Omega, \mathbf{g^{n+1}} \cdot \mathbf{n}(\mathbf{x}) < \mathbf{0}\}$, and set $\mathbf{u}^{n+3/4} = \mathbf{u}(t^{n+1})$.

(4) Finally, solve

$$\begin{cases} \rho \dfrac{\mathbf{u}^{n+1} - \mathbf{u}^{n+3/4}}{\triangle t} - \nabla \cdot [\mu(\mathbf{x}) \mathbf{2D}(\mathbf{u^{n+1}})] = \mathbf{f}^{n+1} \text{ in } \Omega \times (t^n, t^{n+1}), \\ \mathbf{u}^{n+1} = \mathbf{g}^{n+1} \text{ on the top and bottom of } \Omega \\ \text{and is periodic in the } x_1 \text{ direction.} \end{cases} \tag{2.21}$$

2.6 Finite element approximation

Concerning the finite element based space approximation of $\{\mathbf{u}, p\}$ in problem (2.19)-(2.21), we have used the P_1-*iso*-P_2 and P_1 finite element approximation (e.g., see [32] (Chapter 5)). Suppose that a rectangular computational domain $\Omega \subset R^2$ is chosen with length L, h is a space discretization step, $\mathbf{T}_h$ is a finite element triangulation of $\overline{\Omega}$ for velocity, and $\mathbf{T}_{2h}$ is a twice coarser triangulation for pressure (see Figure 2.4). Let P_1 be the space of polynomials in two variables of degree ≤ 1, we introduce the finite dimensional spaces:

$W_{0,h} = \{\mathbf{v}_h | \mathbf{v}_h \in C^0(\overline{\Omega})^2, \mathbf{v}_h|_T \in P_1 \times P_1, \forall T \in \mathbf{T}_h, \mathbf{v}_h = \mathbf{0}$ on the top and bottom of Ω and is periodic in the x_1 direction with period L $\}$,

$W_{g_h,h} = \{\mathbf{v}_h | \mathbf{v}_h \in C^0(\overline{\Omega})^2, \mathbf{v}_h|_T \in P_1 \times P_1, \forall T \in \mathbf{T}_h, \mathbf{v}_h = \mathbf{g}_h(t)$ on the top and bottom of Ω and is periodic in the x_1 direction with period L $\}$,

$W_h = \{\mathbf{v}_h | \mathbf{v}_h \in C^0(\overline{\Omega})^2, \mathbf{v}_h|_T \in P_1 \times P_1, \forall T \in \mathbf{T}_h, \mathbf{v}_h$ is periodic in the x_1 direction with period L $\}$,

$L_h^2 = \{q_h | q_h \in C^0(\overline{\Omega}), q_h|_T \in P_1, \forall T \in \mathbf{T}_{2h}, q_h$ is periodic in the x_1 direction with period L $\}$,

$L_{h,0}^2 = \{q_h | q_h \in L_h^2, \int q_h dx = 0\}$.

Then we obtain the following subproblems (some of the subscripts h have been dropped):

$\mathbf{u}^0 = \mathbf{u}_0$ is given. For $n \geq 0, \mathbf{u}^n$ being known, we compute the approximation solution via the following fractional steps:

(1) Solve

$$\begin{cases} \rho \int_\Omega \dfrac{\mathbf{u}^{n+1/4} - \mathbf{u}^n}{\triangle t} \cdot \mathbf{v} d\mathbf{x} - \int_\Omega p^{n+1/4} (\nabla \cdot \mathbf{v}) d\mathbf{x} = 0 \ \ \forall \mathbf{v} \in W_{0,h}, \\ \int_\Omega q \nabla \cdot \mathbf{u}^{n+1/4} d\mathbf{x} = 0 \ \ \forall q \in L_h^2, \\ \mathbf{u}^{n+1/4} \in W_{g_h,h}^{n+1}, p^{n+1/4} \in L_{h,0}^2. \end{cases} \tag{2.22}$$

(2) Update the position of the membrane based on $\mathbf{u}^{n+1/4}$ by (2.13) and (2.14) and then compute the force $\mathbf{f}_B$ on the fluid-cell interface by (2.8) and (2.10). Find the Heaviside function $\theta(d)$ (2.17) to define the viscosity function $\mu(\mathbf{x})$ (2.18).

(3) Solve

$$\begin{cases} \int_\Omega \dfrac{\partial \mathbf{u}(t)}{\partial t} \cdot \mathbf{v} d\mathbf{x} + \int_\Omega (\mathbf{u}^{n+1/4} \cdot \nabla) \mathbf{u}(\mathbf{t}) \cdot \mathbf{v} d\mathbf{x} = 0 \text{ on } (t^n, t^{n+1}), \\ \forall \mathbf{v} \in W_{0,h}, \mathbf{u}(t^n) = \mathbf{u}^{n+1/4}, \\ \mathbf{u}(t) \in W_h, \mathbf{u}(t) = \mathbf{g}_h(t^{n+1}) \text{ on } \Gamma_-^{n+1} \times (t^n, t^{n+1}), \end{cases} \tag{2.23}$$

and set $\mathbf{u}^{n+3/4} = \mathbf{u}(t^{n+1})$.

(4) Finally, solve

$$\begin{cases} \rho \int_\Omega \dfrac{\mathbf{u}^{n+1} - \mathbf{u}^{n+3/4}}{\triangle t} \cdot \mathbf{v} d\mathbf{x} + 2 \int_\Omega \mu(\mathbf{x}) \mathbf{D}(\mathbf{u^{n+1}}) : \mathbf{D}(\mathbf{v}) d\mathbf{x} = \int_\Omega \mathbf{f}^{n+1} \cdot \mathbf{v} d\mathbf{x} \\ \forall \mathbf{v} \in W_{0,h}, \mathbf{u}^{n+1} \in W_{g_h,h}^{n+1}, \end{cases} \tag{2.24}$$

here $W_{g_h,h}^{n+1} = W_{g_h(t^{n+1}),h}$.

Remark 2.1. The degenerated quasi-Stokes problem (2.22) is solved by a preconditioned conjugate gradient method (e.g., see [32]), in which discrete elliptic problems from the preconditioning are solved by a matrix-free fast solver from FISHPAK by

Adams *et al.* in [3]. The advection problem (2.23) for the velocity field is solved by a wave-like equation method as in [18] and [19].

Remark 2.2. General speaking, when the viscosities μ_{out} and μ_{in} are different, the problem (2.24) is solved by the method of successive over-relaxation (SOR).

Remark 2.3. When $\mu(\mathbf{x})$ is a constant (i.e. $\mu_{\text{out}} = \mu_{\text{in}} = \mu$), the term $2\int_\Omega \mu(\mathbf{x})\mathbf{D}(\mathbf{u}) : \mathbf{D}(\mathbf{v})d\mathbf{x}$ in (2.24) can be replaced by $\mu\int_\Omega \nabla\mathbf{u} : \nabla\mathbf{v}d\mathbf{x}$ since $\mathbf{u}$ is divergence free. Then the problem (2.24) is a classical discrete elliptic problem which can be solved by the matrix-free fast solver. In this case, also we can skip the second part of step (2) in algorithm (2.22)−(2.24) and obtain the one in [68].

2.7 Fictitious domain method

In equation (2.1), if the domain Ω is shown in Figure 2.5, i.e., Ω is replaced by $\Omega \setminus \overline{\omega}$, and $\mu(\mathbf{x}, t) = \mu$ (a costant), then the fictitious domain formulation with distributed Lagrange multipliers (DLM/FD formulation) of the problems (2.1)−(2.4) in a curved boundary channel reads as follows:

For a.e. $t > 0$, find $\mathbf{u}(t) \in W_{0,P}$, $p(t) \in L^2_0, \lambda \in \Lambda$ such that

$$\begin{cases} \rho\int_\Omega \left[\dfrac{\partial\mathbf{u}}{\partial t} + (\mathbf{u}\cdot\nabla)\mathbf{u}\right]\cdot\mathbf{v}d\mathbf{x} + \mu\int_\Omega \nabla\mathbf{u} : \nabla\mathbf{v}d\mathbf{x} - \int_\Omega p\nabla\cdot\mathbf{v}d\mathbf{x} \\ = \int_\Omega \mathbf{f}\cdot\mathbf{v}d\mathbf{x} + < \lambda, \mathbf{v} > \ \ \forall\mathbf{v} \in W_{0,P}, \end{cases} \tag{2.25}$$

$$\int_\Omega q\nabla\cdot\mathbf{u}(t)d\mathbf{x} = 0 \ \forall q \in L^2(\Omega), \tag{2.26}$$

$$< \mu, \mathbf{u}(\mathbf{t}) > \ = \mathbf{0} \ \forall\mu \in \Lambda, \tag{2.27}$$

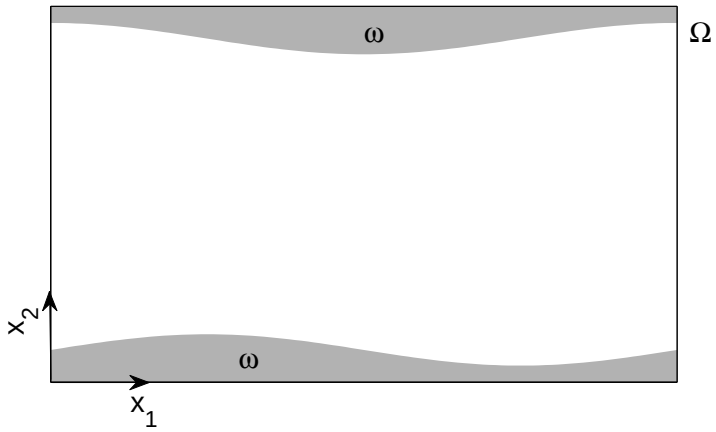

Figure 2.5: An example of computational domain with a curved boundary.

$$\mathbf{u}(\mathbf{x}, 0) = \mathbf{u}_0(\mathbf{x}). \tag{2.28}$$

with

$W_{0,P} = \{\mathbf{v} | \mathbf{v} \in (H^1(\Omega))^2, \mathbf{v} = \mathbf{0}$ on the top and bottom of Ω and is periodic in the x_1 direction with period L $\}$,

$L_0^2 = \{q | q \in L^2(\Omega), \int_\Omega q dx = 0\}$,

$\Lambda = (H^1(\omega))^2$.

In equations (2.25)$-$(2.28), λ is a Lagrange multiplier associated with relation (2.27) and $< \cdot, \cdot >$ is an inner product on Λ (see [66] for more information).

A finite dimensional space approximation Λ is defined as follows: let $\{\mathbf{x}_i\}_{i=1}^M$ be

a set of points from $\overline{\omega}$ which cover $\overline{\omega}$ (uniformly, for example); we define then

$\Lambda_h = \{\mu_h | \mu_h = \sum_{i=1}^{M} \mu_i \delta(\mathbf{x} - \mathbf{x}_i), \mu_i \in \mathbf{R}^2, \forall i = 1, \cdots, N\}$, where $\delta(\cdot)$ is the Dirac measure at $\mathbf{x} = \mathbf{0}$. Then we shall use $< \cdot, \cdot >$ defined by

$$< \mu_h, \mathbf{v}_h > \ = \sum_{i=1}^{M} \mu_i \cdot \mathbf{v}_h(\mathbf{x}_i) \ \forall \mu_h \in \Lambda_h, \mathbf{v}_h \in W_{0,h}.$$

Then we apply the *Lie's Scheme* to equations (2.25)−(2.28) with the IBM and the backward Euler method in time for some subproblems and obtain the following subproblems (some of the subscripts h have been dropped):

$\mathbf{u}^0 = \mathbf{u}_0$ is given. For $n \geq 0, \mathbf{u}^n$ being known, we compute the approximation solution via the following fractional steps:

(1) Solve

$$\begin{cases} \rho \int_\Omega \dfrac{\mathbf{u}^{n+1/4} - \mathbf{u}^n}{\triangle t} \cdot \mathbf{v} d\mathbf{x} - \int_\Omega p^{n+1/4} (\nabla \cdot \mathbf{v}) d\mathbf{x} = 0 \ \ \forall \mathbf{v} \in W_{0,h}, \\ \int_\Omega q \nabla \cdot \mathbf{u}^{n+1/4} d\mathbf{x} = 0 \ \ \forall q \in L_h^2, \\ \mathbf{u}^{n+1/4} \in W_{0,h}^{n+1}, p^{n+1/4} \in L_{h,0}^2. \end{cases} \tag{2.29}$$

(2) Update the position of the membrane based on $\mathbf{u}^{n+1/4}$ by (2.13) and (2.14) and then compute the force $\mathbf{f}_B$ on the fluid-cell interface by (2.8) and (2.10).

(3) Solve

$$\begin{cases} \int_\Omega \dfrac{\partial \mathbf{u}(\mathbf{t})}{\partial t} \cdot \mathbf{v} d\mathbf{x} + \int_\Omega (\mathbf{u}^{n+1/4} \cdot \nabla) \mathbf{u}(\mathbf{t}) \cdot \mathbf{v} d\mathbf{x} = 0 \text{ on } (t^n, t^{n+1}) \ \ \forall \mathbf{v} \in W_{0,h}, \\ \mathbf{u}(t^n) = \mathbf{u}^{n+1/4}, \\ \mathbf{u}(t) \in W_{0,h} \text{ on } (t^n, t^{n+1}), \end{cases} \tag{2.30}$$

and set $\mathbf{u}^{n+3/4} = \mathbf{u}(t^{n+1})$.

(4) Finally, solve

$$\begin{cases} \rho \int_\Omega \dfrac{\mathbf{u}^{n+1} - \mathbf{u}^{n+3/4}}{\triangle t} \cdot \mathbf{v} d\mathbf{x} + \mu \int_\Omega \nabla \mathbf{u}^{n+1} : \nabla \mathbf{v} d\mathbf{x} = \int_\Omega \mathbf{f}^{n+1} \cdot \mathbf{v} d\mathbf{x} + < \lambda, \mathbf{v} > \quad \forall \mathbf{v} \in W_{0,h}, \\ < \mu, \mathbf{u}^{n+1} > \ = 0 \ \forall \mu \in \Lambda_h, \\ \mathbf{u}^{n+1} \in W_{0,h}, \lambda \in \Lambda_h. \end{cases} \tag{2.31}$$

The degenerated quasi-Stokes problem (2.29) is solved by a preconditioned conjugate gradient method (e.g., see [32]), in which discrete elliptic problems from the preconditioning are solved by a matrix-free fast solver from FISHPAK by Adams *et al.* in [3]. The advection problem (2.30) for the velocity field is solved by a wave-like equation method as in [18] and [19]. Problem (2.31) can be solved by a conjugate gradient method ([66]).

Chapter 3

A single RBC in shear flows

In this chapter, as a validation test of the model and the method, the steady inclination angles of the tank treading of two different degrees of confinement for five values s^* in shear flow [81] are compared with the simulation results in [42], then the effect of the viscosity ratio $\lambda = \frac{\eta_{\text{in}}}{\eta_{\text{out}}}$, and the degree of confinement R_0/w (here w is the half channel height) are studied. The values of parameters for modeling cells are the same with [67, 80] as follows: The bending constant is $k_b = 5 \times 10^{-10}$ Nm, the spring constant is $k_l = 5 \times 10^{-8}$ Nm, and the penalty coefficient is $k_s = 10^{-5}$ Nm. The cells are suspended in blood plasma which has a density $\rho = 1.00$ g/cm^3 and a dynamical viscosity $\mu = 0.012$ g/(cms). The computational domain is a two-dimensional horizontal channel. A simple shear flow is produced by two walls at the top and bottom which have the same speed but move in directions opposite to each other. Different shear rate can be obtained by adjusting the wall speed. In addition, periodic conditions are imposed at the left and right boundaries of the domain. The

R_0/w	Re	C_a
0.8	0.01	0.455
0.4	0.041	0.455
0.28	0.084	0.455
0.187	0.188	0.455
0.14	0.333	0.455
0.112	0.52	0.455

Table 3.1: Reynolds number Re and capillary number C_a for different degrees of confinement R_0/w.

Reynolds number is defined by $\mathrm{Re} = \rho U H/\mu$, where U is the average velocity in the channel. The capillary number is defined by $C_a = \mu \mathrm{G_r} {\mathrm{R_0}}^3/\mathrm{B}$, where μ, $\mathrm{G_r}$, $\mathrm{R_0}$, and B represent the plasma viscosity, the shear rate of fluid flow, the effective radius of the cell, and the bending coefficient, respectively.

3.1 Tank treading in shear flows

First, we present the results on simulation of a single RBC suspended in a linear shear flow with shear rate $\gamma = 500\ \mathrm{s}^{-1}$. The dimensions of the computational domain are $112 \times 7\ \mu\mathrm{m}^2$ and $112 \times 14\ \mu\mathrm{m}^2$. The two degrees of confinement are 0.8 for the narrower domain and 0.4 for the wider domain, respectively. The associated Reynolds number and the capillary number are shown in Table 3.1. The grid resolution for the computational domain is 80 grid points per 10 μm. The time step Δt is 10^{-5} ms. The viscosity ratio $\lambda = 1$. The initial velocity of the fluid flow is zero everywhere and the initial positions of the mass center of the cell are (56,3.5) and (56,7) for the narrower domain and the wider domain, respectively. Figures 3.1 and 3.2 show the pressures and the velocity fields in the region next to the cells for two different

degrees of confinement. The blue solid lines in the left figures and the black solid lines in the right figures represent the cell membrane. In the left figures, the regions with darker color correspond to higher pressure and the lighter regions correspond to lower pressure. The figures of velocity fields indicate that the cells perform tank-treading motion in confined channels and the inner fluid of the cell undergoes a rotational flow, which is induced by the cell membrane tank treading. The outer fluid of the cell exhibits recirculations at the right side of the figure and at the left side of the figure of the cell. Such recirculations are also observed for confined rotating rigid particles in a simple shear flow [21, 39, 95] with period conditions in the shear direction.

The steady inclination angles of the tank treading as shown in Figure 3.3 and the associated frequency of two different degrees of confinement for five values s^*=0.6, 0.7, 0.8, 0.9, and 1.0 are presented in Figure 3.4, which show very good agreement with the lattice-Boltzmann simulation results of Kaoui *et al.* [42]. The inclination angle increases monotonically for both two degrees of confinement with increasing the value of the swelling ratio s^*. For the same swelling ratio, the bigger the degree of confinement, the smaller the steady inclination angle. The same qualitative tendency is reported in [7, 28, 42, 50, 53, 68]. The frequency is an increasing function of s^* for $R_0/w = 0.4$, but for $R_0/w = 0.8$, it increases first as increasing s^* then reaches a peak, and decreases when s^* increases further. Similar trend for the frequency was reported in [42]. We also keep track of the area and the perimeter of the cell during the simulations. The variation is less than $\pm 0.1\%$ in the area and $\pm 0.5\%$ in the perimeter.

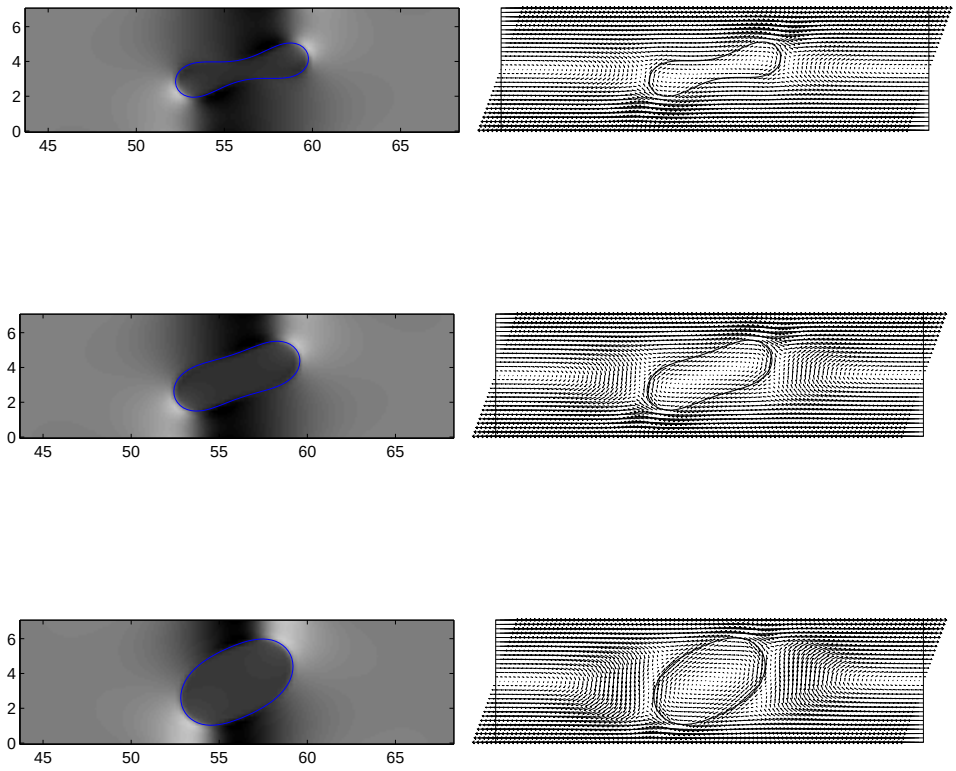

Figure 3.1: The pressure (left) and the velocity field (right) in the region next to the cell with the swelling ratio $s^* = 0.481$ (top), 0.7 (middle), and 0.9 (bottom), respectively. $R_0/w = 0.8$. The units for both axes are μm.

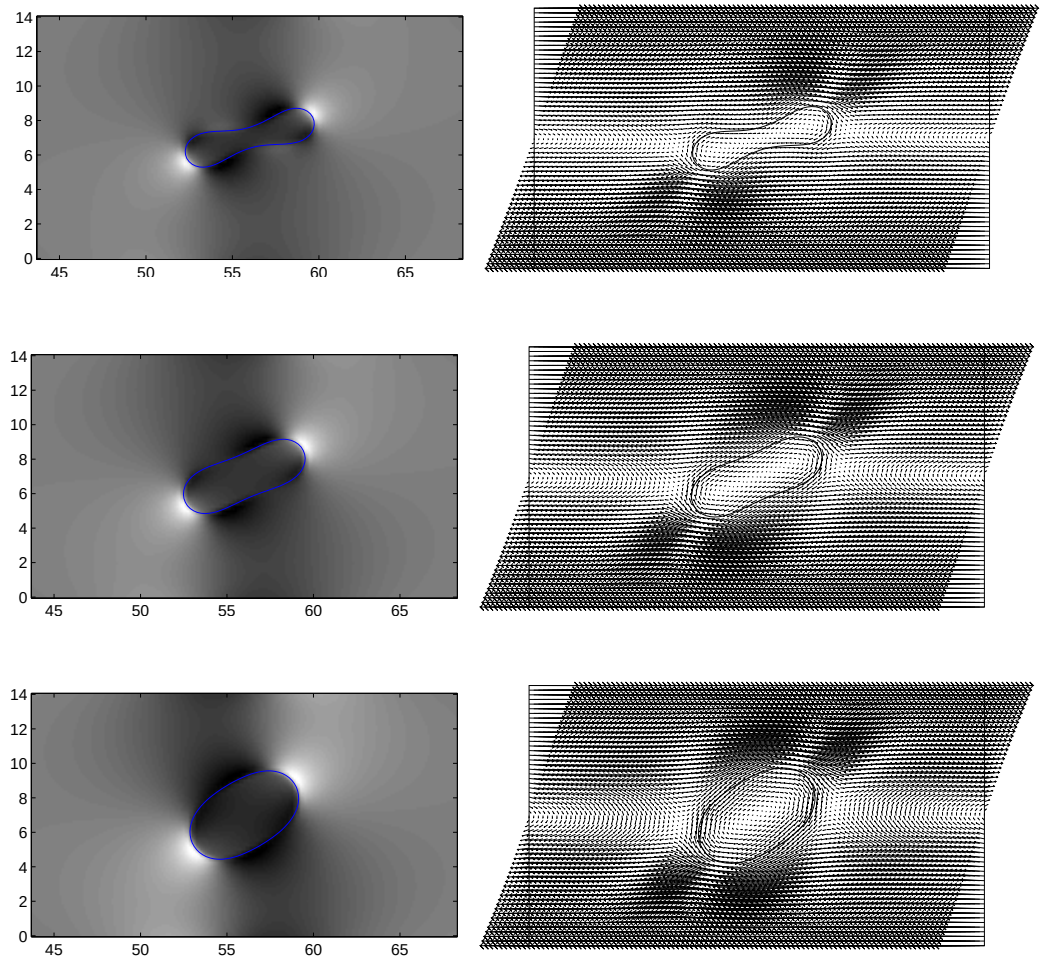

Figure 3.2: The pressure (left) and the velocity field (right) in the region next to the cell with the swelling ratio $s^* = 0.481$ (top), 0.7 (middle), and 0.9 (bottom), respectively. $R_0/w = 0.4$. The units for both axes are μm.

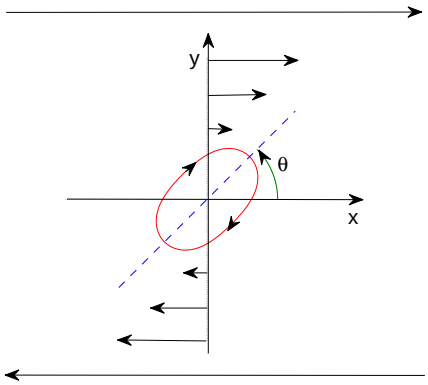

Figure 3.3: A schematic representation of tank-treading of RBC in shear flow. θ is the inclination angle.

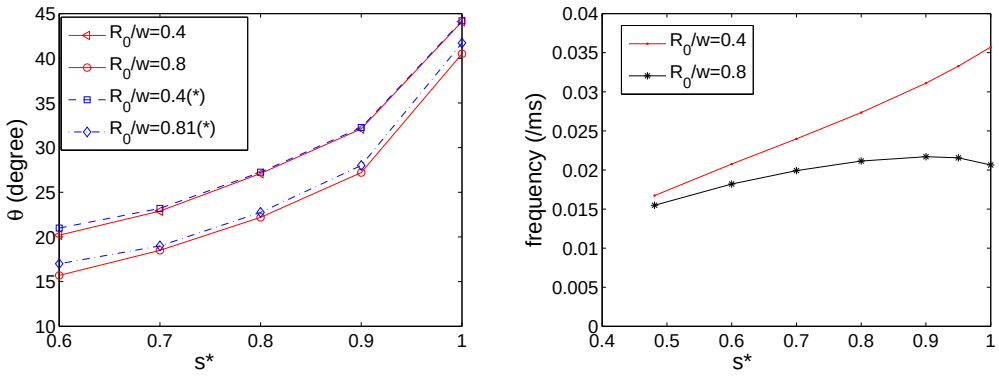

Figure 3.4: Steady inclination angle θ and the associated frequency as a function of the cell swelling ratio s^* for two degrees of confinement $R_0/w = 0.4$ and 0.8. (* from [42])

3.2 Effect of the viscosity ratio and the degree of confinement

As the first part of this section, the effect of the viscosity ratio λ on the dynamics of a single RBC in a shear flow is considered. The computational domain is a rectangular region with dimensions 112×50 μm^2 and the associated degree of confinement is 0.112. The effect of the wall is weak. The grid resolution for the computational domain is 80 grid points per 10 μm. The time step Δt is 10^{-5} ms. The initial velocity of the fluid flow is zero everywhere and the initial position of the mass center of the cell is (56,25). The shear rate is set as $\gamma = 500$ s^{-1} and the associated Re is about 0.52.

It is well known that either the vesicle or the RBC in a shear flow undergoes a tank-treading motion at its equilibrium position [8, 20, 25, 27, 42, 50, 68, 81] when the viscosity ratio λ is small. This also can be observed in the simulation results in Figure 3.5, which shows the simulation results of the tank-trading motion with a steady inclination angle for the values of the swelling ratio $s^* = 0.481$ and 0.9 with different $\lambda = 1$ and 2. The inclination angle θ between the long axis of the cell and the horizontal direction decreases as increasing the value of λ.

Over the past decades, the dependence of the inclination angle θ on the swelling ratio s^* and the viscosity ratio of λ has been studied by many researchers. For the ellipsoidal shape particle (i.e. the membrane deformation is not considered), Keller *et al.* [50] has given an evolutional equation for the inclination angle θ as shown in

Figure 3.3:

$$\frac{d\theta}{dt} = A + B\cos(2\theta) \tag{3.1}$$

where A and B are functions of the viscosity ratio λ, the shear rate γ, and the shape of the ellipsoid (see [50] for more information about A and B). There are two motions determined by the equation (3.1) namely, (1) tank-treading motion if $A/B < 1$, in this case the inclination angle θ can be calculated by

$$\theta = \frac{\arccos(-A/B)}{2}, \tag{3.2}$$

(2) tumbling motion if $A/B > 1$, in this case, the general solution of the equation (3.1) can be expressed as

$$\theta(t) = \arctan(\frac{A+B}{\sqrt{A^2 - B^2}}\tan(\sqrt{A^2 - B^2}(t - t_0))) \tag{3.3}$$

The snapshots of tumbling motion of RBC for the swelling ratio $s^* = 0.481$ and the associated inclination angle θ as a function of the time are shown in Figure 3.6.

The simulation results of the inclination angles θ as a function of the viscosity ratio λ for six different values of the swelling ratio $s^* = 0.481$, 0.6, 0.7, 0.8, 0.9, and 0.95 are displayed in Figure 3.7. In the tank-treading regime, the inclination angle θ is a decreasing function of the viscosity ratio λ for the same swelling ratio s^* , but for the same viscosity ratio λ, the inclination angle θ increases as the swelling ratio s^* increases. Our simulation results show good agreement with the numerical results reported in [52] by Kim *et al.*. The small deviation of our results from Keller *et al.* [50] is due to the fact that they assumed the cell has a fixed elliptical boundary and no deformability. A transition from tank-treading motion to tumbling motion

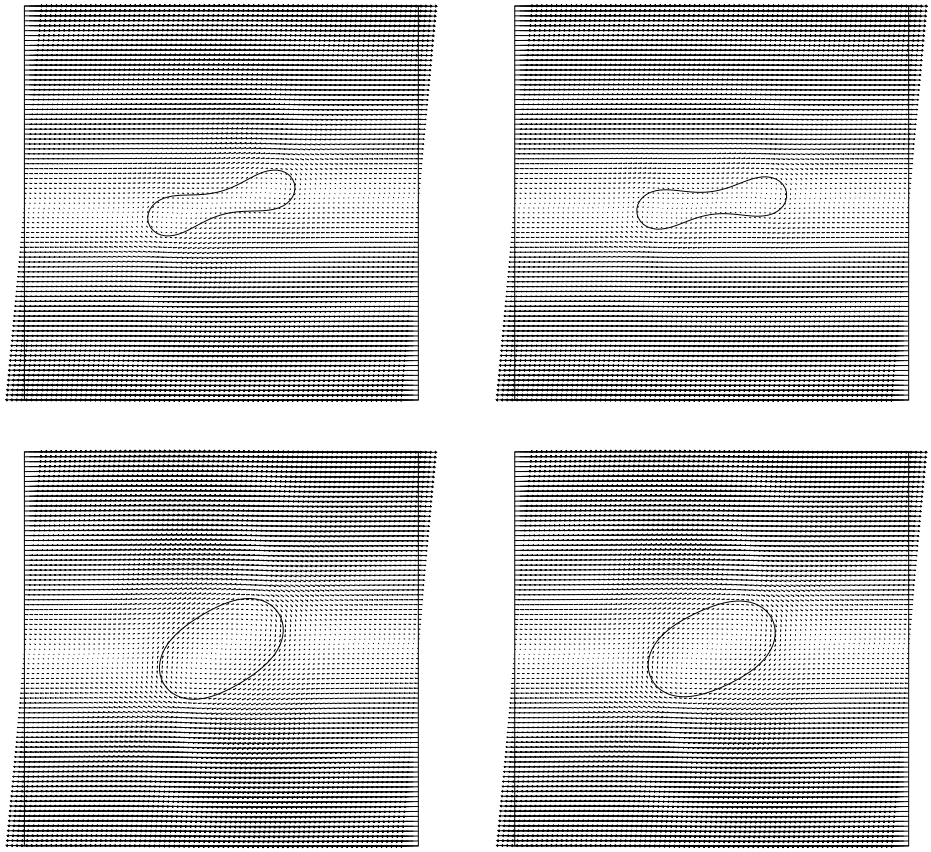

Figure 3.5: The velocity field in the region next to the cell with the swelling ratio s^* = 0.481 (top) and 0.9 (bottom), respectively. $R_0/w = 0.112$. $\lambda = 1$ (left) and $\lambda = 2$ (right).

happens as the viscosity ratio λ reaches a critical value λ_c for a given swelling ratio s^* and λ_c increases as s^* increases (see Figure 3.8). According the KS theory, the viscosity ratio λ reaches its critical value λ_c when $A = -B$, and the inclination angle θ depends on λ with a square root law. The value of the critical ratio λ_c in Figure 3.8 is obtained by interpolate at $\theta = 0$ with a square root law for the numerical results in Figure 3.7. Similar trend of the viscosity ratio versus the swelling ratio was reported in [7, 52].

But for the narrower channel with dimensions $112 \times 1.4\ \mu\text{m}^2$ ($R_0/w = 0.8$), other parameters are kept same as those at the beginning of Section (3.2). All of cells considered here undergoes the tank-treading motion. The steady inclination angle and the associated frequency as a function of λ are shown in Figure 3.9. For the same viscosity ratio λ (such as 5), the behavior of cell (such as the cell of $s^* < 0.9$) is different for these two different degrees of confinement R_0/w, and the inclination angles are also different even for the tank treading regim (as shown in Figures 3.9 (left) and 3.7). These results inspire us to explore the further dependence of inclination angle θ on the degree of confinement R_0/w. For the tank treading regim, the simulation results show that for $\lambda = 1$, the inclination angle θ is a decreasing function of R_0/w, but for $\lambda = 5$, θ increases as the increasing value of R_0/w and reaches a peak , then decreases as R_0/w increases (see Figure 3.10). The associated frequency is displayed in Figure 3.11 which shows that the frequency is a decreasing function of R_0/w for $\lambda = 1$, however, it decreases as the increasing value of R_0/w and reaches a peak , then increases as R_0/w increases further for $\lambda = 5$. The similar tendency was reported in [43].

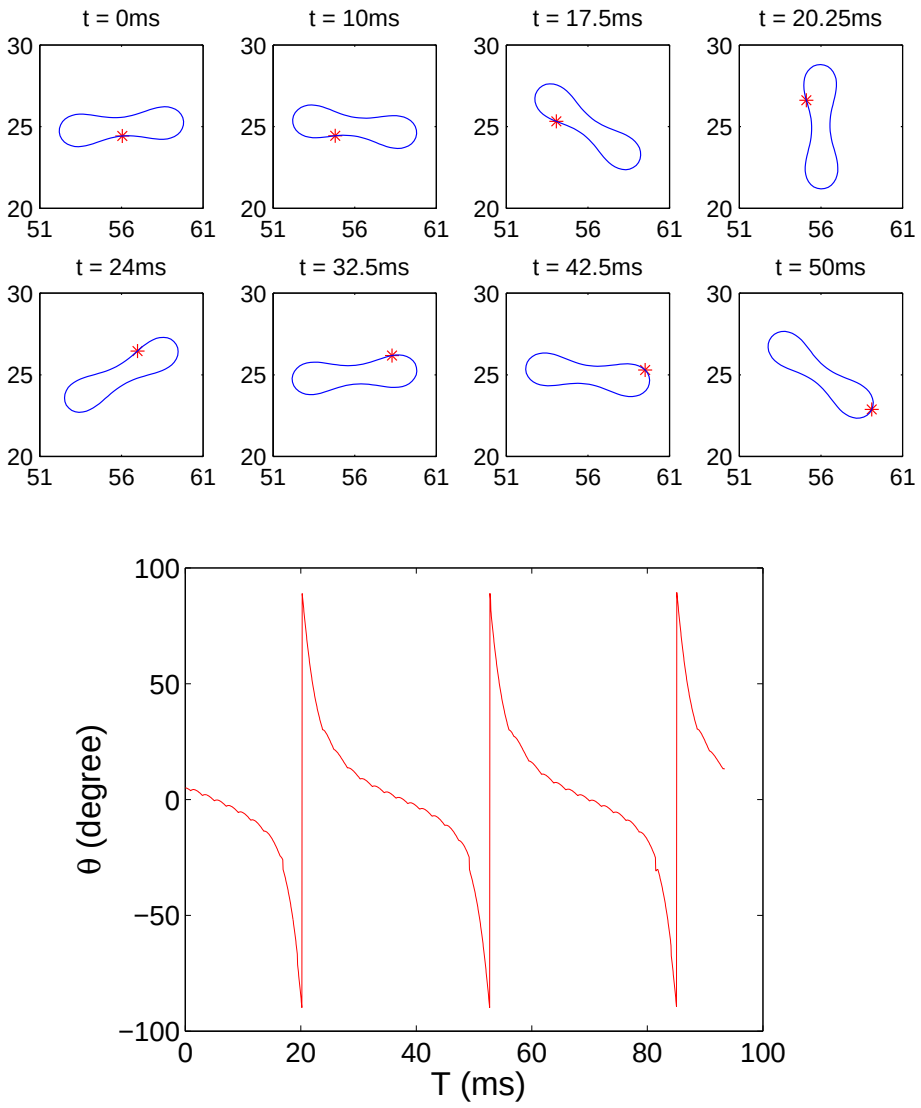

Figure 3.6: The snapshots of RBC with the swelling ratio $s^* = 0.481$ at different time (top and middle) and the associated time-dependent orientation angle θ (bottom). $\lambda = 5$.

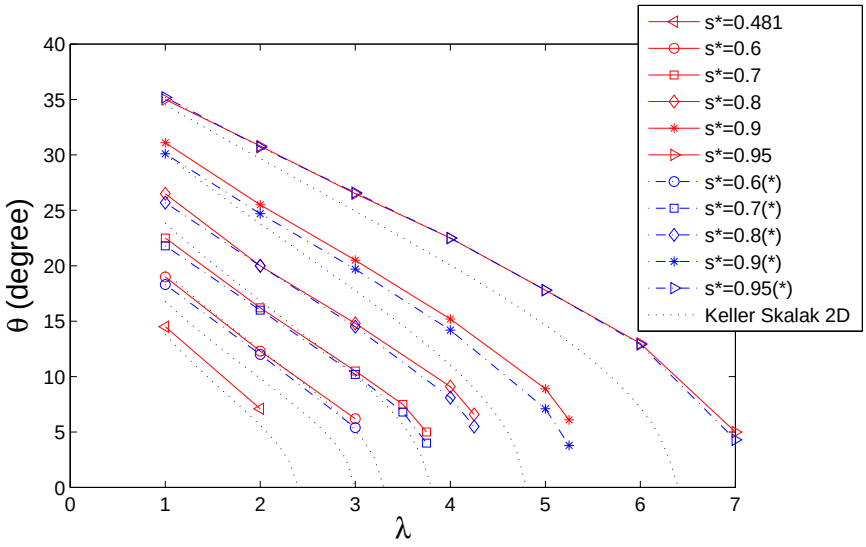

Figure 3.7: Steady inclination angle θ as a function of the viscosity ratio λ for different values of the swelling ratio s^*. The degree of confinement $R_0/w = 0.112$. (* from [52])

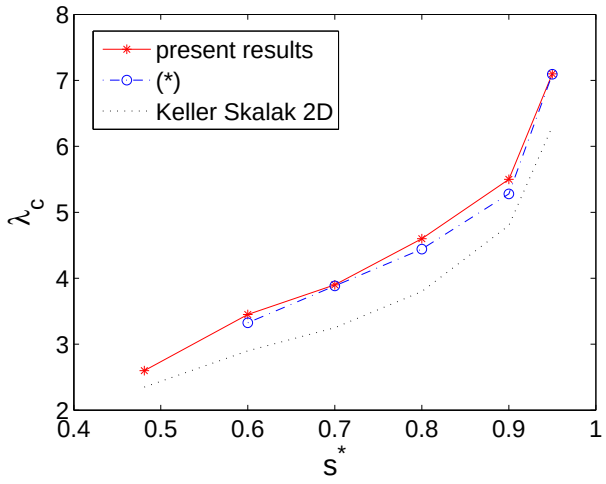

Figure 3.8: The critical viscosity ratio λ_c as a function of the swelling ratio s^*. (* from [52])

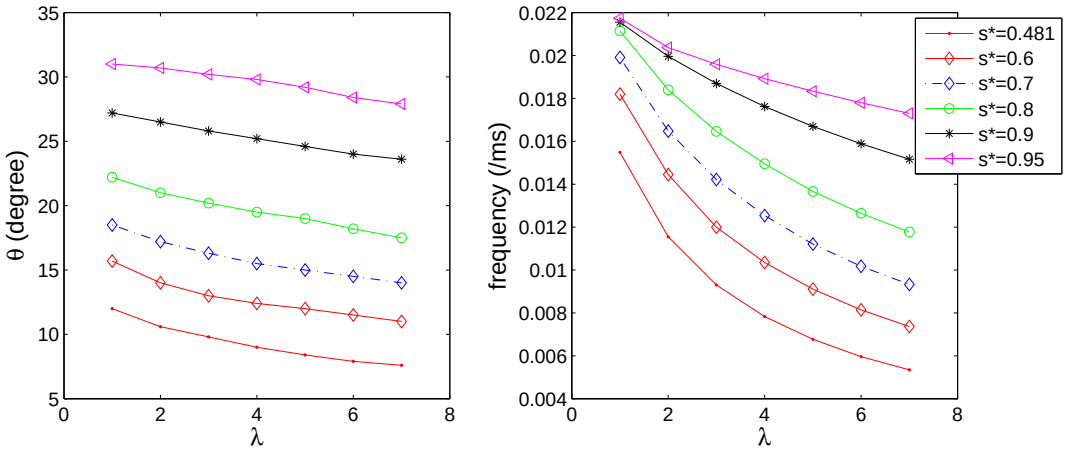

Figure 3.9: Steady inclination angle θ (left) and the associated frequency (right) as a function of λ. $R_0/w = 0.8$.

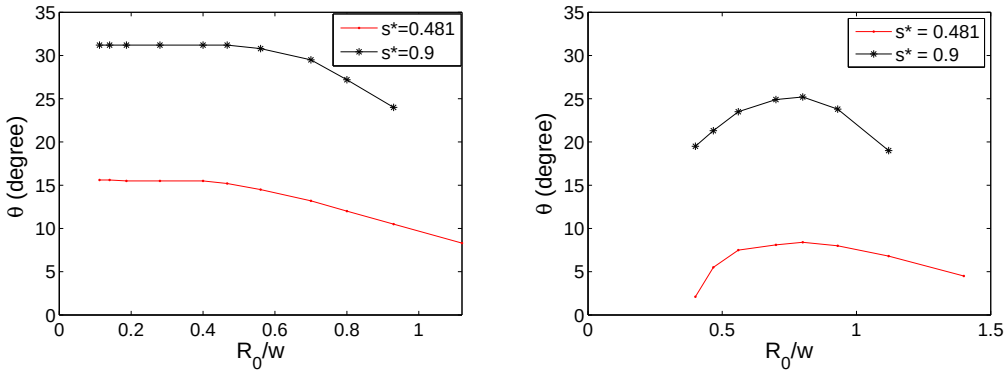

Figure 3.10: Steady inclination angle θ as a function of the degree of confinement R_0/w for $s^* = 0.481$ and 0.9 with $\lambda = 1$ (left) and 5 (right).

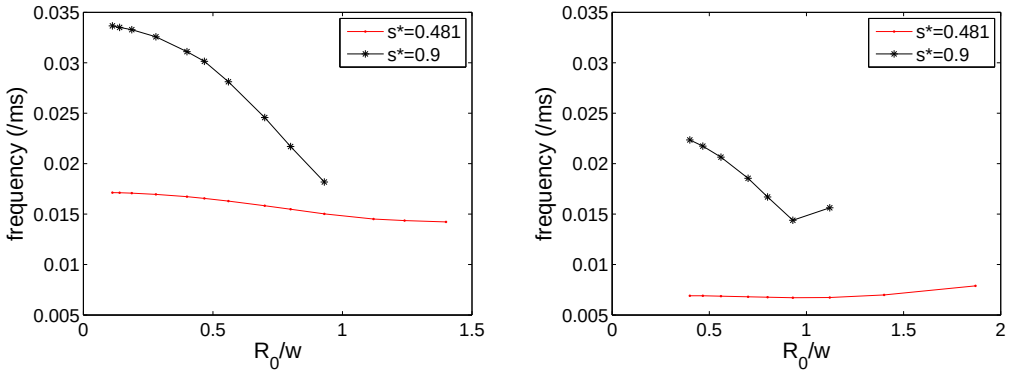

Figure 3.11: Frequency as a function of as a function of the degree of confinement R_0/w for $s^* = 0.481$ and 0.9 with $\lambda = 1$ (left) and 5 (right).

For the case of $\lambda = 5$, we have studied four more degrees of confinement R_0/w = 0.112, 0.14, 0.187, and 0.28. The other parameters are kept same as those at the beginning of Section (3.2). The associated Re and C_a are shown in Table 3.1. For a given swelling ratio s^*, a transition from tank-treading motion to tumbling motion occurs when the degree of confinement R_0/w decreases. The dependence of the cell motion on the degree of confinement for different swelling ratio is shown in Figure 3.12, which indicates that under the condition of the existence of the transition from TT to TB, the smaller s^*, the bigger the critical value of R_0/w. For the tank-treading regime, the steady inclination angle and the associated frequency as a function of s^* for the different degrees of confinement are shown in Figure 3.13. The inclination angle θ is an increasing function of the swelling ratio s^* for the same R_0/w, and it decreases as decreasing R_0/w for the same s^*. The frequency is also an increasing function of the swelling ratio for the same R_0/w. But for a given s^*, the frequencies are almost same since the shear rates of the flow are same.

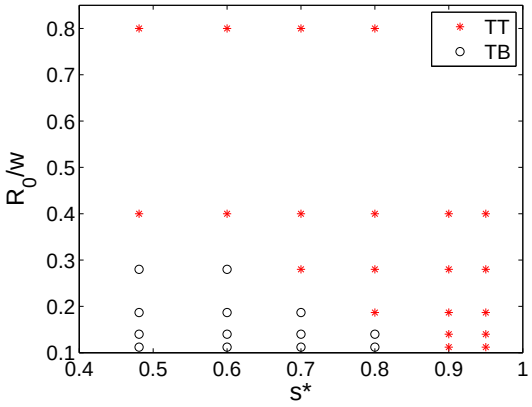

Figure 3.12: Relation between the behavior of cell in shear flow and the degree of confinement R_0/w for different swelling ratios s^* with $\lambda = 5$. TT and TB denote tank-treading motion and tumbling motion, respectively.

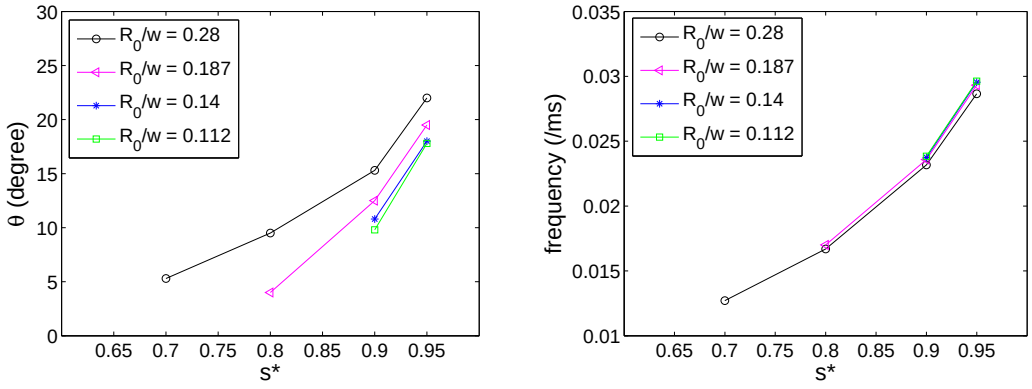

Figure 3.13: Steady inclination angle θ (left) and the associated frequency as a function of s^* (right) for the different degrees of confinement R_0/w . $\lambda = 5$.

As the ending of this section, the effect of the shear rate is examined. A transition from TB to TT occurs as the shear rate $\gamma > 15000$ s^{-1} (the associated Re is about 5) for $\lambda = 5$ and $R_0/w = 0.28$. i.e. A tank-treading motion is a favorable one at a higher Reynolds number in a shear flow. The similar behavior of vesicle was reported in [52].

Chapter 4

RBC in bounded Poiseuille flows

In this chapter, the deformation and lateral migration of a single cell in two-dimensional Poiseuille flows have been investigated. Then the results of simulations involving many RBCs in Poiseuille flows are presented and validated by comparing the size of the cell-free layer next to the walls. Finally, the simulation results of the interaction of two kinds of cells in Poiseuille flow are included.

The values of parameters for modeling cells are the same with [67, 80] as follows: The bending constant is $k_b = 5 \times 10^{-10}$ Nm, the spring constant is $k_l = 5 \times 10^{-8}$ Nm, and the penalty coefficient is $k_s = 10^{-5}$ Nm. The cells are suspended in blood plasma which has a density $\rho = 1.00$ g/cm^3 and a dynamical viscosity $\mu = 0.012$ g/(cms). The viscosity ratio $\lambda = 1$. The computational domain is a two-dimensional horizontal channel. To obtain a Poiseuille flow, a constant pressure gradient is prescribed as a body force. In addition, periodic conditions are imposed at the left and right boundaries of the domain. The Reynolds number is defined by $\mathrm{Re} = \rho U H/\mu$, where

U is the average velocity in the channel. The capillary number is defined by $C_a = \mu \mathrm{G_r} {\mathrm{R_0}}^3/\mathrm{B}$, where μ, $\mathrm{G_r}$, $\mathrm{R_0}$, and B represent the plasma viscosity, the shear rate of fluid flow based on the gradient of the velocity at the wall, the effective radius of the cell, and the bending coefficient, respectively.

4.1 Deformation of a single cell in Poiseuille flows

In this section, the deformation of a single RBC in bounded two-dimensional Poiseuille flows is studied by numerical simulation. Several factors have been found to be important in determining the deformation of a single RBC in Poiseuille flows: the swelling ratio (s^*), the initial angle of the long axis of the cell at the center line (φ), the maximum velocity at the center line of fluid flow ($u_{\max}$), the membrane bending stiffness of a RBC (k_b), and the height of the microchannel (H). Two motions of oscillation and vacillating breathing (also called swing; the long axis undergoes oscillation while the cell shape displays breathing) of the RBC are observed in both narrow and wide channels. The strength of the vacillating-breathing motion depends on the degree of confinement and the value of $u_{\max}$. An RBC exhibits a strong vacillating-breathing motion as the degree of confinement is larger or the value $u_{\max}$ is higher. For the same degree of confinement, the vacillating-breathing motion appears to be relatively weaker but persists longer as the value of $u_{\max}$ is lower. For the different bending constants, the RBC obtains the same equilibrium shape for the same capillary number C_a. The continuation of shape change from the slipper to the parachute shape by varying the value of $u_{\max}$ is obtained for the biconcave shape

cell in a narrower channel. In particular, parachute shape and bullet-like shape, depending on the initial angle φ, coexist for the elliptic shape cell with lower $u_{\max}$ in a narrower channel.

4.1.1 Effect of the swelling ratio

We first present the simulation results of a single RBC in a Poiseuille flow with the fluid domain 100×10 μm^2. The pressure gradient is set to as a constant for this study so that the Reynolds number of the Poiseuille flow without the cell is about 0.4167. The initial velocity is zero everywhere. The grid resolution for the computational domain is 64 grid points per 10 μm. Three different shapes ($s^* =$ 0.481, 0.7, and 0.9) have been studied and the results are shown in Figure 4.1. The initial position of the mass center of the single cell is located at (5,3). The initial angle of the long axis of the cell at the center line is $\varphi = 0$. In Figure 4.1, the cells deform and migrate to the center line of the microchannel and the well-known parachute shape has been observed for the case of $s^* = 0.481$, 0.7 and 0.9. The red asterisk denotes the same point on the cell membrane for the entire simulation. The similar results of capsules in tube flow using the boundary element method have been reported by Pozrikidis in [74].

Given the same initial angle $\varphi = 0$, the effect of different initial positions has been investigated. Migrations of RBCs with $s^* = 0.481$ and 0.9 for three different initial positions (5,3), (5,5), and (5,7.7) are shown in Figure 4.2. The cells with the initial positions (5,3) and (5,7.7) deform and migrate to the center line of the microchannel

where steady axisymmetric states are reached. The cell with the initial position (5,5) parallels to the direction of the flow after it is released, then deforms owing to the hydrodynamic stress imposed symmetrically by the Poiseuille flow, until it reaches a parachute shape as its equilibrium shape. The final position and shape are not related with the initial positions of the RBC.

4.1.2 Effect of the initial angle

The initial angle φ has an important effect on the equilibrium position and shape for the elliptic shape cell with $s^* = 0.9$. Two equilibrium shapes, parachute shape and bullet-like shape, coexist at the center line as equilibrium shapes for $u_{\max} = 1.0$ cm/s with different initial inclination angles φ (see Figure 4.3). When φ is bigger than 37°, a parachute shape is obtained, otherwise a bullet-like shape is obtained. The similar qualitative results of the cell in an unbounded Stokes flow have been reported in [17]. The averaged velocities of the fluid with the cell are 0.653 cm/s for the cell type I (bullet-like shape) and 0.642 cm/s for the cell type II (parachute shape), respectively, and the energy stored in the membrane of the cell type I is lower than that of the cell type II. That is because the resistance force acted on the fluid by the cell type I is less than the force by the cell type II. This resistance force depends on the cell cross section perpendicular to the direction of fluid flow in a narrow channel and the velocity of quadratic flow without cell. Then the inverse force acted on the cell type I by the fluid is less than the inverse force acted on the cell type I by the fluid. This interplay between the fluid and the cell is the main source of the energy stored in the membrane.

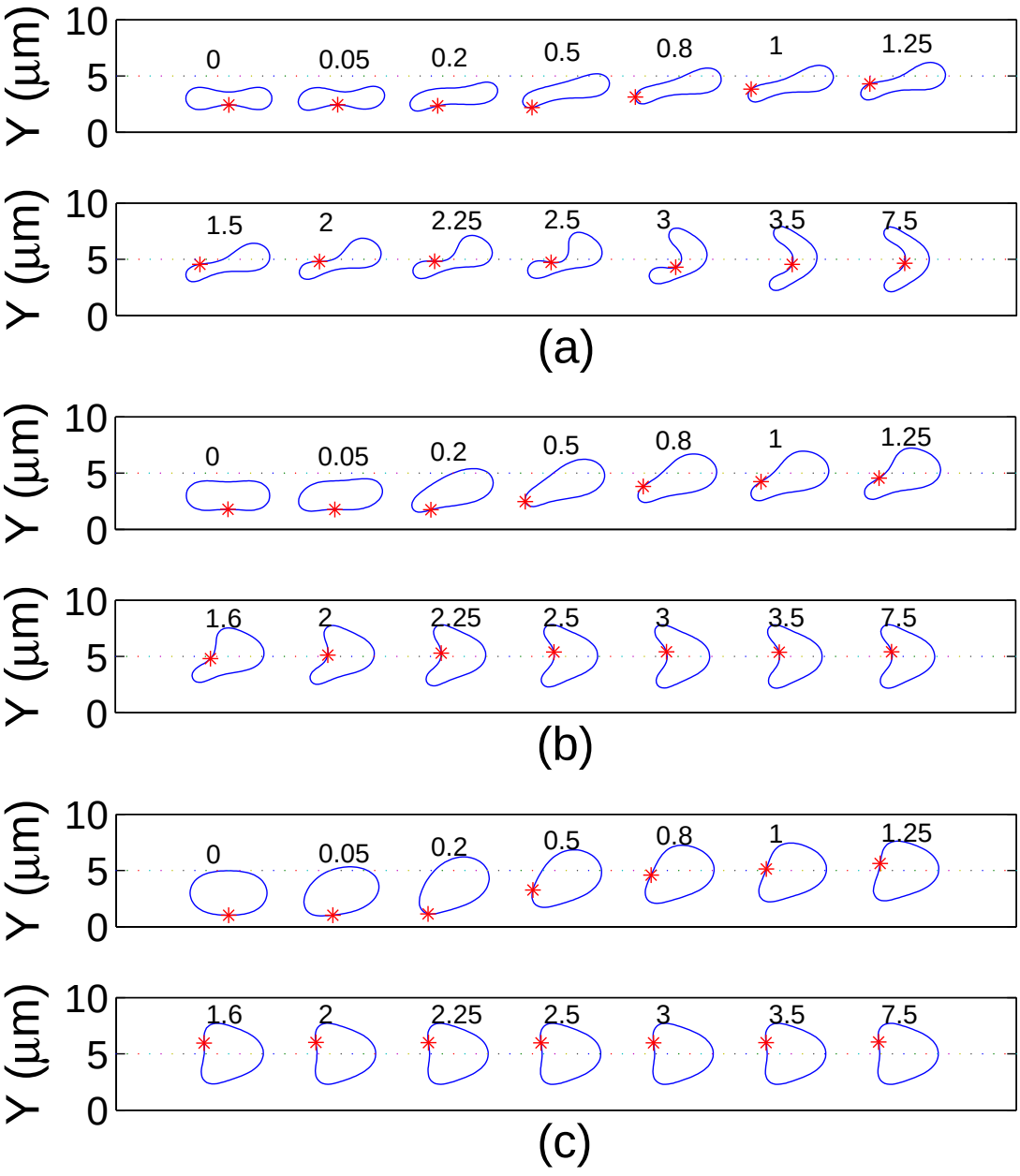

Figure 4.1: The snapshots of the cell migration at different time (ms): (a) $s^* = 0.481$, (b) $s^* = 0.7$, and (c) $s^* = 0.9$. The red asterisk denotes the same node point on the cell membrane.

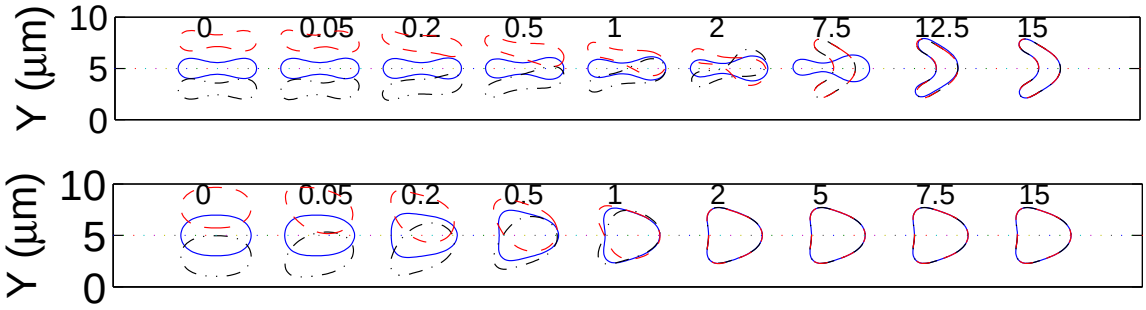

Figure 4.2: The snapshots of the cell migration with $s^* = 0.481$ (top) and 0.9 (bottom) at different time (ms) for three different initial positions.

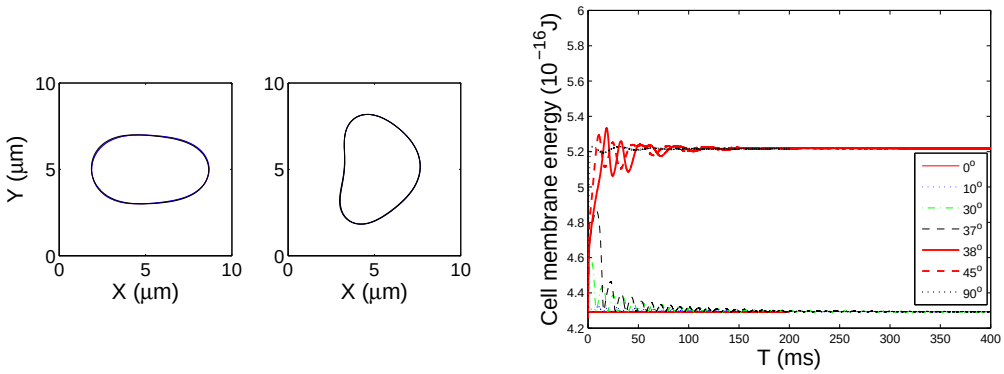

Figure 4.3: Two shapes: bullet-like shape with $u_{\max} = 1$ cm/s and $\varphi = 0°$, 10°, 30°, and 37° (left) and parachute shape with $u_{\max} = 1$ cm/s and $\varphi = 38°$, 45°, and 90° (middle). The histories of cell membrane energy for different initial inclination angles φ (right).

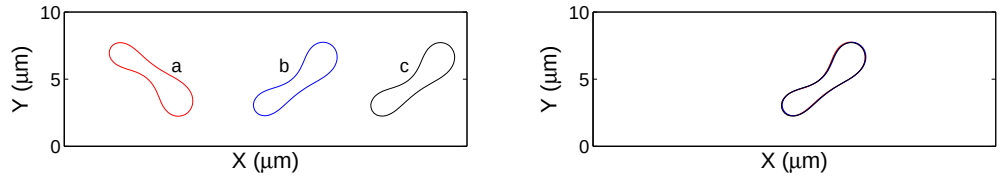

Figure 4.4: The equilibrium shapes for different initial angles:(a) $\varphi = 0$, (b) $\varphi = 45°$, and (c) $\varphi = 90°$ (left). The shapes after shifting and reflecting with respect to the center line of the channel (right). $s^* = 0.481$ and $u_{\max} = 1$ cm/s.

However, for the biconcave shape cell $s^* = 0.481$, only a slipper shape has been obtained at the center line as its equilibrium shape for $u_{\max} = 1.0$ cm/s with the initial inclination angles of $0°, 45°$, and $90°$ as shown in Figure 4.4. It indicates that the slipper shape could be the only equilibrium shape for the low $u_{\max}$.

4.1.3 Effect of the maximum velocity

The effect of $u_{\max}$ on the deformation of a single cell has been investigated. In the simulations, we have kept other parameters the same as in Section 4.1.1. We observed that $u_{\max}$ plays a critical role on the equilibrium shapes of a single RBC migration in a narrow channel. Both slipper shape and parachute shape are obtained by varying the value of $u_{\max}$. The slipper shape is obtained when $u_{\max}$ is lower than a critical value $u_c = 3$ cm/s (resp., 2.8 cm/s) for $s^* = 0.481$ (resp., 0.7), and the parachute shape is obtained when $u_{\max}$ is higher than u_c. The asymmetric shape (slipper

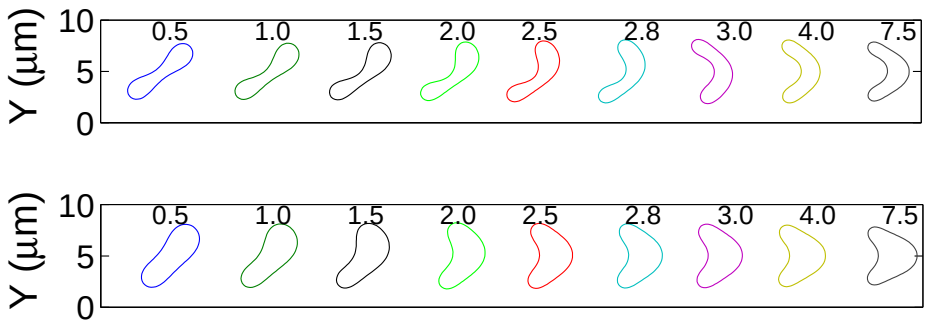

Figure 4.5: The equilibrium shapes of a single cell in a Poiseuille flow for $s^* = 0.481$ (top) and 0.7 (bottom) with $u_{\max}$ from 0.5 to 7.5 cm/s.

shape) of the vesicle in an unbounded Poiseuille flow at zero Reynolds number has been studied by Kaoui *et al.* [40], and the similar results of vesicle also mentioned in [75, 76, 84]. Figure 4.5 shows that the equilibrium shapes for $s^* = 0.481$ and 0.7 with nine different values of $u_{\max} = 0.5$, 1.0, 1.5, 2.0, 2.5, 2.8, 3.0, 4.0, and 7.5 cm/s, and the corresponding Reynolds numbers of the Poiseuille flow without cell are about 0.0278, 0.0556, 0.0833, 0.1111, 0.1389, 0.1556, 0.1667, 0.2222, and 0.4167, respectively. The histories of the cell membrane energy for $s^* = 0.481$ and 0.7 are shown in Figure 4.6. When the cell reaches the equilibrium position and shape, the cell membrane energy of the parachute shape is higher than that of the slipper shape and the flow with higher $u_{\max}$ can provide enough energy to sustain the shape of a parachute. The distance Y_d between the mass center of equilibrium cell and the center line is zero for the parachute shape, but Y_d is nonzero for the slipper shape. These results are reported in Figure 4.7. Our present simulation results are in good agreement with the results in [40].

For the above nine different values of $u_{\max}$, the equilibrium shapes of the elliptic shape cell for $s^* = 0.9$ with two different initial angles $\varphi = \pi/4$ and 0 are shown in Figure 4.8. For $\varphi = 0$, the cell deforms and reaches a bullet-like shape as its equilibrium shape when $u_{\max}$ is lower than $u_c = 3$ cm/s, otherwise it attains a parachute shape. But for $\varphi = \pi/4$, the cell deforms and reaches a bullet-like shape as its equilibrium shape when $u_{\max}$ is between 1.0 cm/s and 3.0 cm/s, otherwise it attains a parachute shape. Both bullet-like and parachute shapes coexist for $u_{\max}$ = 0.5, 1.0, and 3.0 cm/s. These results indicate that when $u_{\max}$ is high enough, the flow can provide enough energy to sustain two different shapes, parachute shape and bullet-like shape, and the final equilibrium shape is determined by other factors such as the initial inclination angle, etc.

We have also applied the method of the numerical continuation to study the change of the equilibrium shape of the cell for $s^* = 0.481$ and 0.7. After obtaining an equilibrium shape for a given value of $u_{\max}$, we have used it as the initial shape in the simulation for the next larger value of $u_{\max}$. The equilibrium shapes for $s^* = 0.481$ and 0.7 are exactly the same as those given in Figure 4.5.

4.1.4 Effect of the membrane bending stiffness of the RBC and the height of the microchannel

To study the effect of the bending constant, we have kept the same values of k_l and k_s and considered three different values of the bending constants, which are $0.1k_b$, $1k_b$, and $10k_b$. $u_{\max} = 1.0$ cm/s and other conditions are the same as in Section

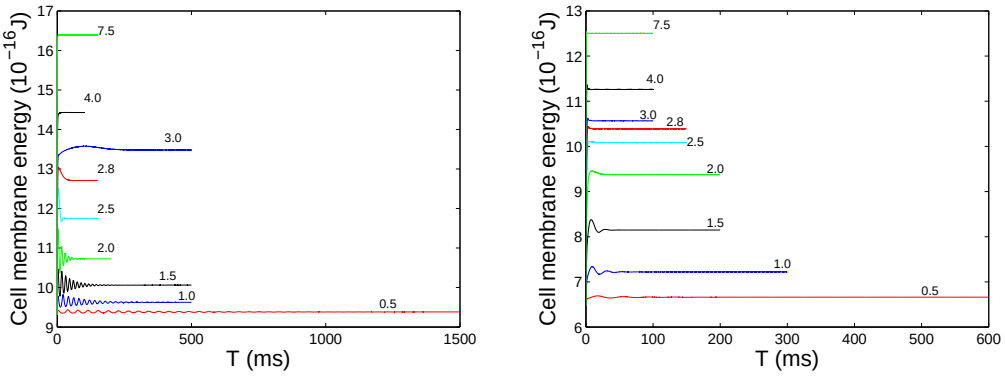

Figure 4.6: The histories of the cell membrane energy in a Poiseuille flow for $s^* = 0.481$ (left) and 0.7 (right) with $u_{\max}$ from 0.5 to 7.5 cm/s.

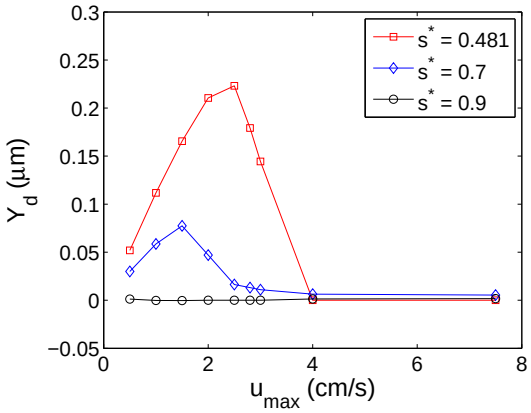

Figure 4.7: The distance Y_d between the mass center of equilibrium cell and the center line as a function of $u_{\max}$ (cm/s).

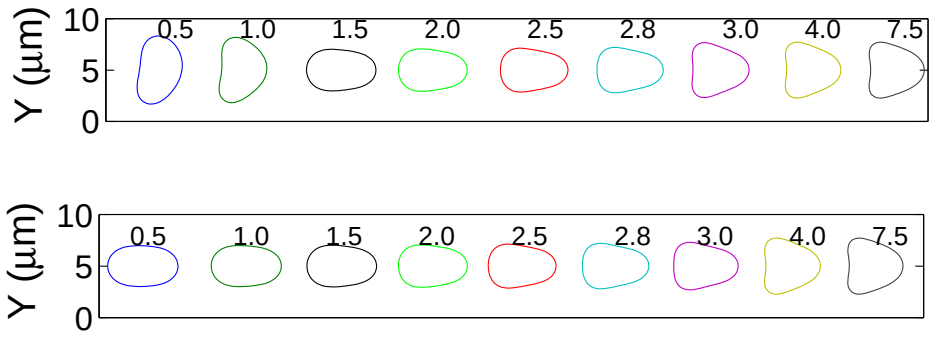

Figure 4.8: The equilibrium shapes of a single cell of $s^* = 0.9$ in a Poiseuille flow with various values of $u_{\max}$ (cm/s) for two initial angles: $\varphi = \pi/4$ (top) and 0 (bottom).

4.1.1. The snapshots of the cell migration in Poiseuille flows for $s^* = 0.481$ and 0.9 with these bending constants are shown in Figure 4.9 and the histories of the cell membrane energy are reported in Figure 4.10. In Figure 4.9, the red asterisk denotes the same point on the cell membrane during the entire simulation. For the lower bending constant $0.1k_b$, a parachute shape is obtained for both the biconcave shape cell $s^* = 0.481$ and the elliptic shape cell $s^* = 0.9$. For the bending constant $1k_b$, both cells exhibit damped vacillating breathing after they are released in the fluid flow as indicated in Figure 4.10. The histories of the cell membrane energy show the vacillating-breathing motion of the elliptic shape cell $s^* = 0.9$ damps out faster than that of the biconcave shape cell of $s^* = 0.481$. The positions and shapes of the vacillating-breathing motion for the biconcave shape cell of $s^* = 0.481$ are shown in Figure 4.11. For the higher bending constant $10k_b$, both cells exhibit damped oscillation until they attain the equilibrium states aligning themselves at an angle with the direction of the flow, and the damping rate of the elliptical shape cell is

bigger than that of the biconcave shape cell. The history of the angle of the long axis of cell at the center line as a function of time is shown in Figure 4.21 (left). The vacillating-breathing motion also takes place for the bending constants $0.1k_b$ with the value of $u_{\max}$ lower than 1.0 cm/s and $10k_b$ with the value of $u_{\max}$ higher than 1.0 cm/s for the biconcave shape cell of $s^* = 0.481$. Figure 4.12 shows the simulation results of the capillary number $C_a = 3.58$ (i.e., $0.1k_b$ with the value of $u_{\max} = 0.1$ cm/s, $1k_b$ with the value of $u_{\max} = 1$ cm/s, and $10k_b$ with the value of $u_{\max} = 10$ cm/s). For the different bending constants, the RBC reaches the same equilibrium shape for the same capillary number in the middle part of Figure 4.12.

The shear rate at the center of the Poiseuille flow is zero, and any deviation of the cell from the center line would be penalized by higher dissipation as a result of the higher shear rate. Thus for a parachute shape cell, no membrane tank treading is present for its symmetric shape and the relative velocity of fluid inside the parachute shape cell also vanishes. However, for a slipper shape cell, its membrane undergoes tank treading and the flow enclosed by the slipper shape cell rotates as shown in Figure 4.13 (a) and 4.13 (c) where the red asterisk denotes the same point on the cell membrane. The similar results of the vesicle and elliptical capsule are also obtained by Kaoui *et al.* [40] and Shin *et al.* [83], respectively.

Finally, the effect of the height of the channel H on the deformation of a single cell is also investigated. We set $u_{\max} = 7.5$ cm/s and vary H. All the other physical and numerical parameters are kept same to those in the Section 4.1.1. Simulations in Figure 4.14 and Figure 4.20 are performed for $H = 10$ and 50 μm, respectively. The corresponding initial positions of the mass center of the single cell are located

at (5,5) and (5,25), respectively. Both of the initial angles are $\varphi = \pi/4$. For the narrower channel with $H = 10$ μm, a parachute shape as its equilibrium shape is obtained for both two bending constants $0.1k_b$ and $1k_b$ (see Figure 4.14 $(a) - (d)$). For the bending constant $10k_b$, the cell of swelling ratio $s^* = 0.481$ exhibits a damped vacillating-breathing motion accompanied by membrane tank-treading until it attains the equilibrium state (a slipper shape as its equilibrium shape) aligning itself at an angle with the direction of the flow as shown in Figures 4.14 (e) and 4.15. But the other one of swelling ratio $s^* = 0.9$ only exhibits oscillation for shorter period of time (see Figure 4.14 (f)) and the cell gradually deforms into a parachute shape. When the bending constant is $100k_b$, both two cells exhibit damped oscillation with the shapes of long body and align themselves with a fixed inclination angle with respect to the flow direction as in Figures 4.14 (g), (h) and 4.15. The damped rate of the elliptic shape cell is also faster than that of the biconcave shape cell. The histories of the height of the cell mass center in Figure 4.16 do show the correlation with the oscillation motion. There is no tank treading for both parachute shape and bullet-like shape since they are symmetric (see Figures 4.13 (b) and (d)).

When placing the initial position of the cell mass center off the center line, we have obtained almost similar behaviors for both two cells in Poiseuille flow as shown in Figures 4.17, 4.18, and 4.19. The vacillating-breathing behavior for the case of the bending constant $10k_b$ and the oscillation for the case of the bending constant $100k_b$ are stronger for the cell of $s^* = 0.481$. But more interesting results are the motions of the cell of $s^* = 0.9$ for the bending constants $10k_b$ and $100k_b$ as shown in Figure 4.17 (f) and (h). A similar motion called snaking motion in Poiseuille flow

has been studied in the Stokes regime in [45]. Actually, the cell of $s^* = 0.9$ exhibits a snaking motion when the equilibrium shape is a bullet-like shape which depends on the initial angle φ (see [81]).

Unlike in a narrower channel, the cell in a wider channel exhibits vacillating-breathing motion after it is released in the fluid flow for the lower bending constant $0.1kb$, and as this motion becomes weak, the cell reaches a slipper shape as its equilibrium state and aligns itself at an angle with the direction of the flow. For the bending constants $1k_b$ and $10k_b$, both two cells exhibit oscillation. The similar simulation results of vesicles by using the boundary integral method are given by Kaoui *et al.* in [45]. The history of the position of the cell mass center, the energy of the cell membrane, and the equilibrium shape are presented in Figure 4.20. The histories of the angle of the long axis of the biconcave cell $s^* = 0.481$ at the center line for the bending constants $1k_b$ and $10k_b$ are shown in Figure 4.21 (right).

The RBC exhibits slipper shape accompanied with (damped) vacillating-breathing motion when the capillary number C_a is less than a critical value such as 10.74 for the biconcave shape cell $s^* = 0.481$ in the narrower channel. For the elliptic shape cell of $s^* = 0.9$, the vacillating-breathing motion damps out quickly. So we focus our attention on investigating the vacillating-breathing motion of the biconcave shape cell for $s^* = 0.481$. Figure 4.22 displays the histories of the energy of the cell membrane of the different values of $u_{\max} = 0.5$, 1.0, 1.5, 2.0, and 2.8 cm/s. The strength of the vacillating-breathing motion depends on the degree of confinement, the maximum velocity at the center line of fluid flow $u_{\max}$ and the capillary number C_a.

The RBC exhibits a stronger vacillating-breathing motion as the degree of confinement is larger or the value $u_{\max}$ is higher. For the same degree of confinement, the vacillating-breathing motion appears to be relatively weaker but persists longer as the value of $u_{\max}$ is lower. For the different bending constants, the RBC obtains the same equilibrium shape for the same capillary number.

4.1.5 Conclusions

The steady shape of the cell under flow depends on the swelling ratio (s^*), the initial angle of the long axis of the cell at the center line (φ), the maximum velocity at the center line of fluid flow ($u_{\max}$), the membrane bending stiffness of the RBC (k_b) and the height of the microchannel (H). Two motions of oscillation and vacillating breathing of the RBC are observed in narrow and wide channels. The strength of the vacillating-breathing motion depends on the degree of confinement and the value of $u_{\max}$. The RBC exhibits a strong vacillating-breathing motion as the degree of confinement is larger or the value of $u_{\max}$ is higher. For the same degree of confinement, the vacillating-breathing motion appears to be relatively weak but persists longer as the value of $u_{\max}$ is lower. For the different bending constants, the RBC obtains the same equilibrium shape for the same capillary number. The continuation of shape change from the slipper to the parachute by varying the value of $u_{\max}$ is obtained for the biconcave shape cell in a narrower channel. In particular, parachute shape and bullet-like shape, depending on the angle φ, coexist for the elliptic shape cell with lower $u_{\max}$ in a narrower channel.

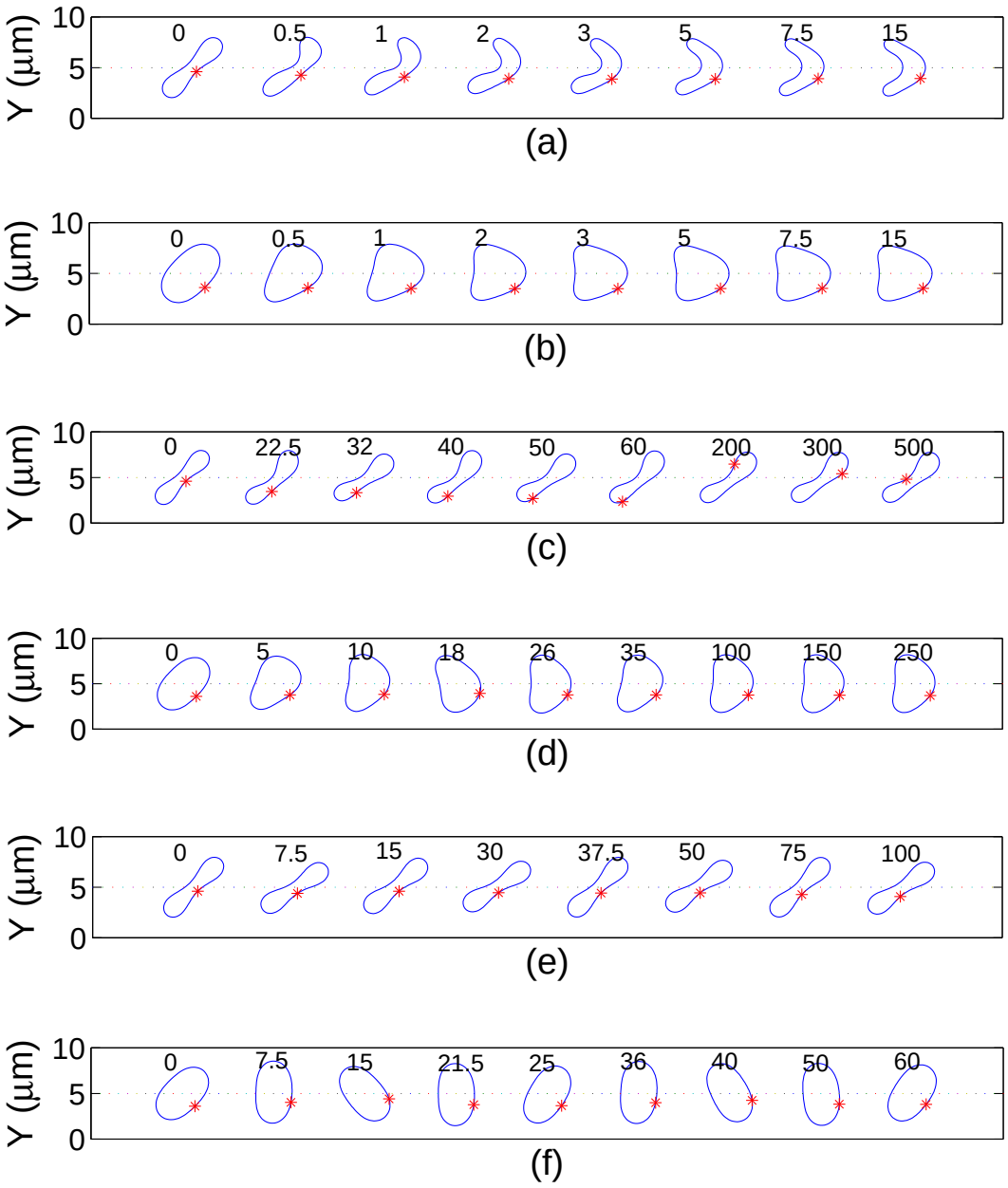

Figure 4.9: The snapshots of the cell migration at different time (ms) for $s^* = 0.481$ and 0.9 with different bending constants: (a) $s^* = 0.481$ and $0.1k_b$, (b) $s^* = 0.9$ and $0.1k_b$, (c) $s^* = 0.481$ and $1k_b$, (d) $s^* = 0.9$ and $1k_b$, (e) $s^* = 0.481$ and $10k_b$, and (f) $s^* = 0.9$ and $10k_b$. The red asterisk denotes the same node point on the cell membrane.

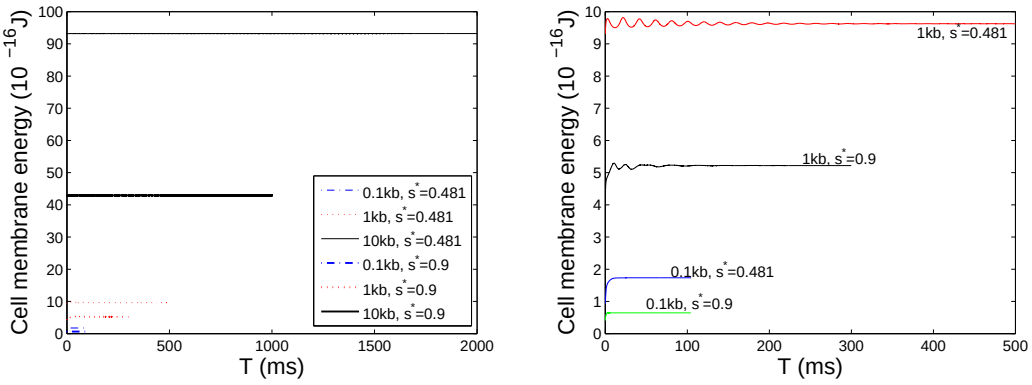

Figure 4.10: The cell membrane energy for $s^* = 0.481$ and 0.9 with different bending constants (left) and the enlarged part (right).

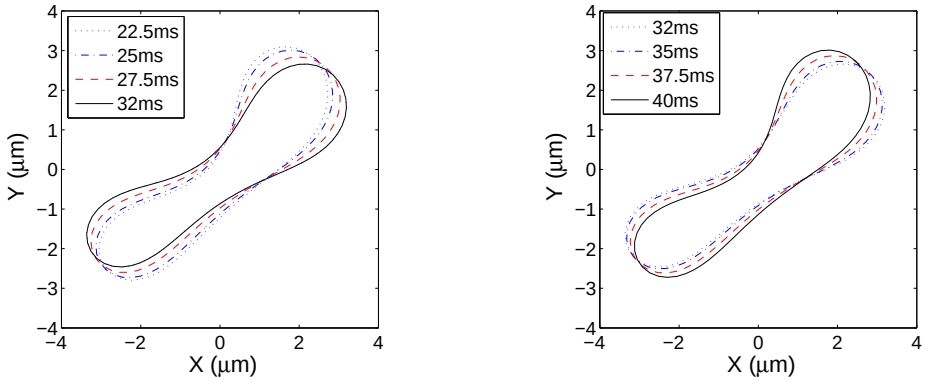

Figure 4.11: The positions and shapes of a single cell for $s^* = 0.481(1k_b)$ at $t = 22.5$, 25, 27.5, and 32 ms (left) and $t = 32$, 35, 37.5, and 40 ms (right).

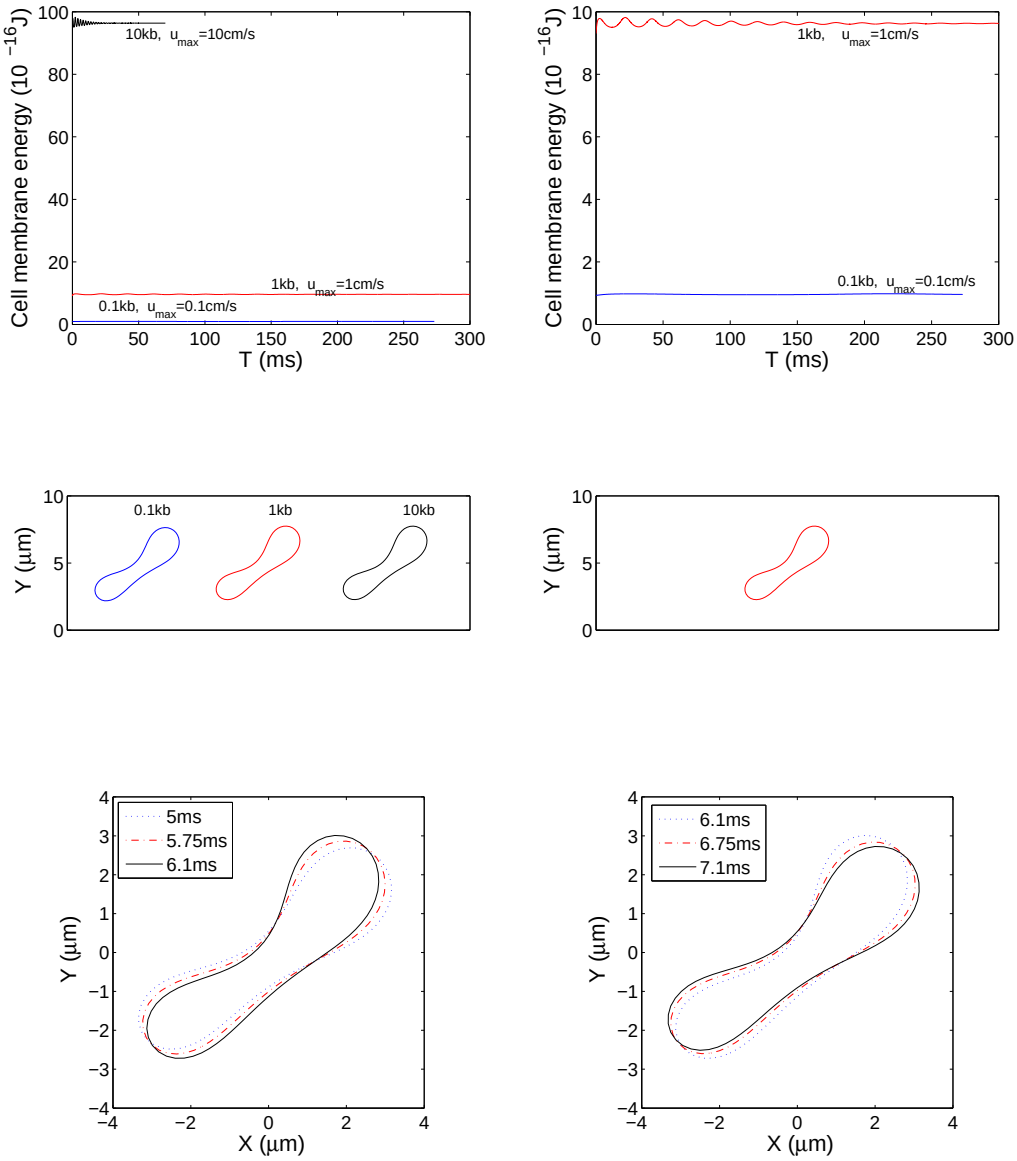

Figure 4.12: The histories of the cell membrane energy for $s^* = 0.481$ with the capillary number $C_a = 3.58$ (top left) and the enlarged part (top right). The equilibrium shapes for different bending constants (middle left) and the shapes after shifting with respect to the center line of the channel (middle right). The positions and shapes of a single cell for $s^* = 0.481$ $(10k_b)$ at $t = 5$, 5.75, and 6.1 ms (bottom left) and $t = 6.1$, 6.75, and 7.1 ms (bottom right).

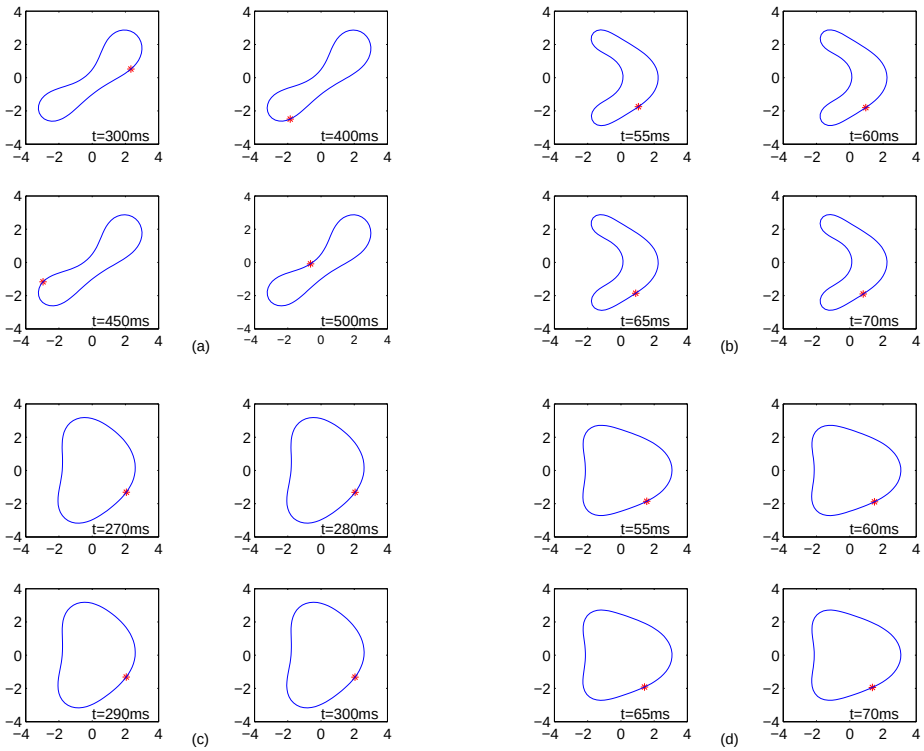

Figure 4.13: Tank treading for a slipper shape cell: (a) $s^* = 0.481$ with $u_{\max} = 1$ cm/s. No tank treading for a parachute shape cell: (b) $s^* = 0.481$ with $u_{\max} = 7.5$ cm/s, (c) $s^* = 0.9$ with $u_{\max} = 1$ cm/s, and (d) $s^* = 0.9$ with $u_{\max} = 7.5$ cm/s. The red asterisk denotes the same node point on the cell membrane. The units for both axes are μm.

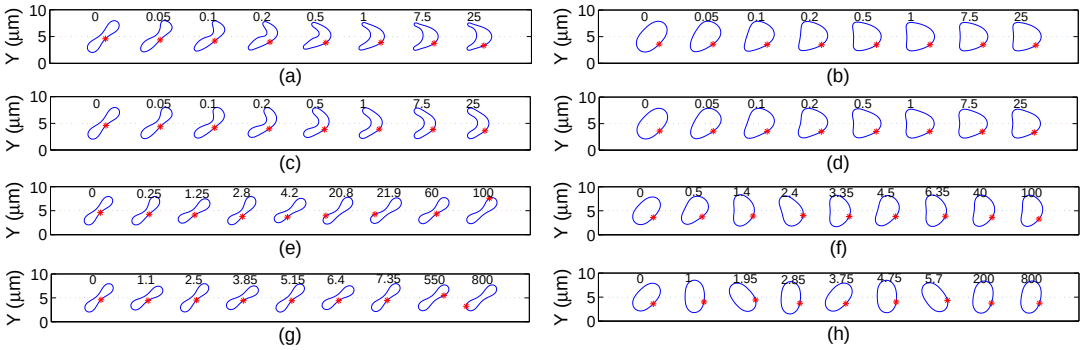

Figure 4.14: The snapshots of the cell motion at different time (ms) for $s^* = 0.481$ and 0.9 with different bending constants: (a) $s^* = 0.481$ and $0.1k_b$, (b) $s^* = 0.9$ and $0.1k_b$, (c) $s^* = 0.481$ and $1k_b$, (d) $s^* = 0.9$ and $1k_b$, (e) $s^* = 0.481$ and $10k_b$, (f) $s^* = 0.9$ and $10k_b$, (g) $s^* = 0.481$ and $100k_b$, and (h) $s^* = 0.9$ and $100k_b$. The red asterisk denotes the same node point on the cell membrane. The initial position is (5,5) and the initial angle is $\pi/4$.

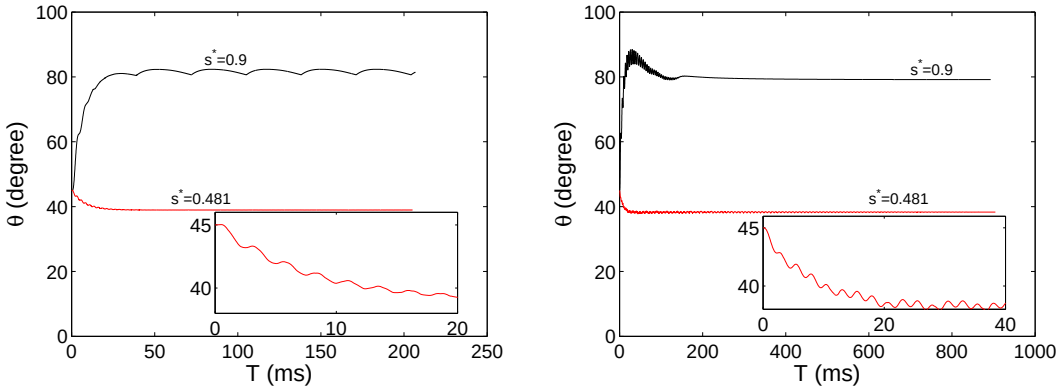

Figure 4.15: The history of the angle between the long axis of cell and the horizontal line for $s^* = 0.481$ and 0.9 with different bending constants: $10k_b$ (left) and $100k_b$ (right). The initial position is (5,5) and the initial angle is $\pi/4$.

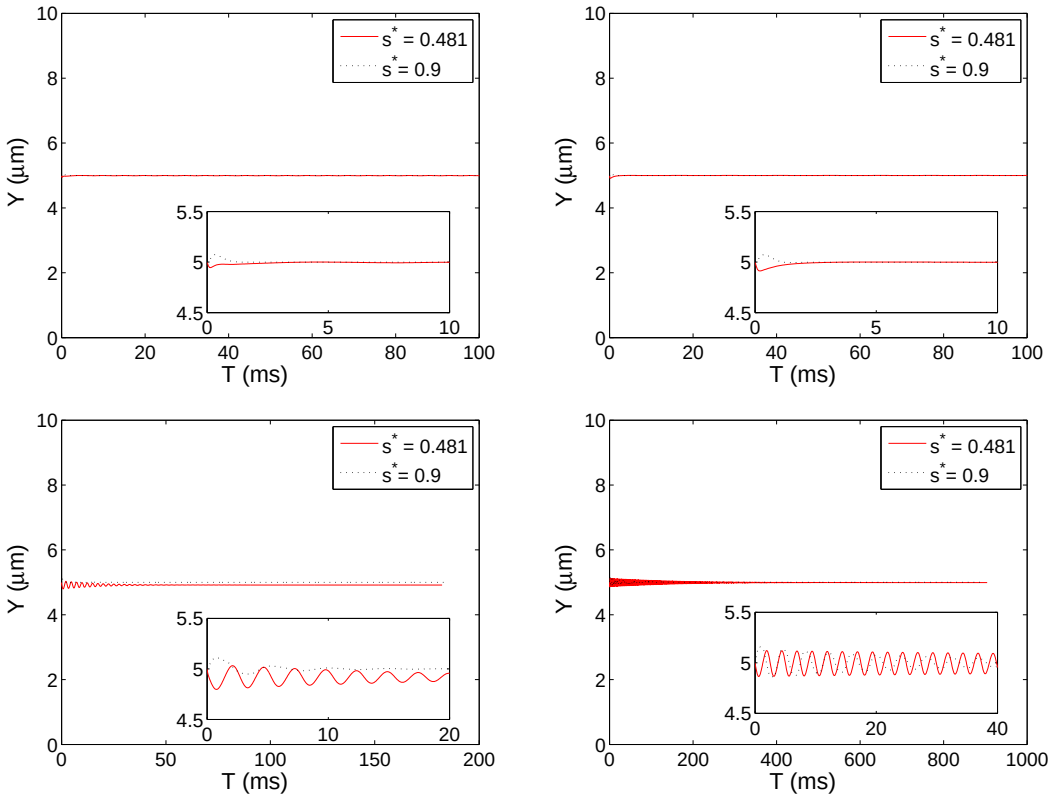

Figure 4.16: The history of the position of the cell mass center for $s^* = 0.481$ and 0.9 with different bending constants: $0.1k_b$ (top left), $1k_b$ (top right), $10k_b$ (bottom left), and $100k_b$ (bottom right). The initial position is (5,5) and the initial angle is $\pi/4$.

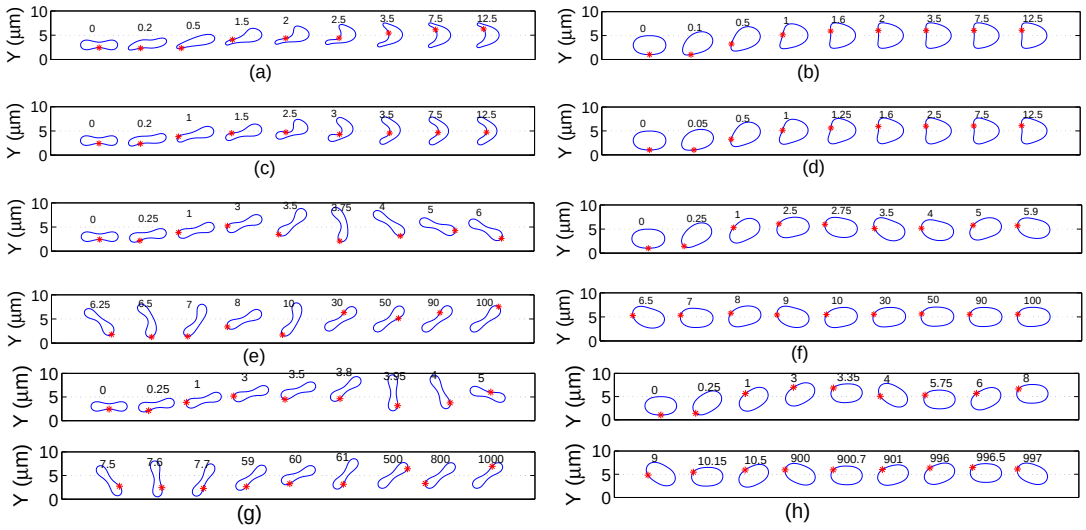

Figure 4.17: The snapshots of the cell motion at different time (ms) for $s^* = 0.481$ and 0.9 with different bending constants: (a) $s^* = 0.481$ and $0.1k_b$, (b) $s^* = 0.9$ and $0.1k_b$, (c) $s^* = 0.481$ and $1k_b$, (d) $s^* = 0.9$ and $1k_b$, (e) $s^* = 0.481$ and $10k_b$, (f) $s^* = 0.9$ and $10k_b$, (g) $s^* = 0.481$ and $100k_b$, and (h) $s^* = 0.9$ and $100k_b$. The red asterisk denotes the same node point on the cell membrane. The initial position is (5,3) and the initial angle is 0.

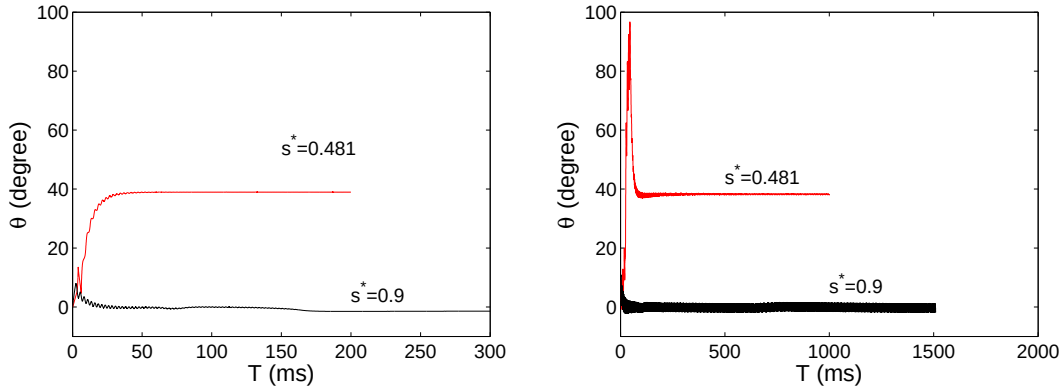

Figure 4.18: The history of the angle between the long axis of cell and the horizontal line for $s^* = 0.481$ and 0.9 with different bending constants: $10k_b$ (left) and $100k_b$ (right). The initial position is (5,3) and the initial angle is 0.

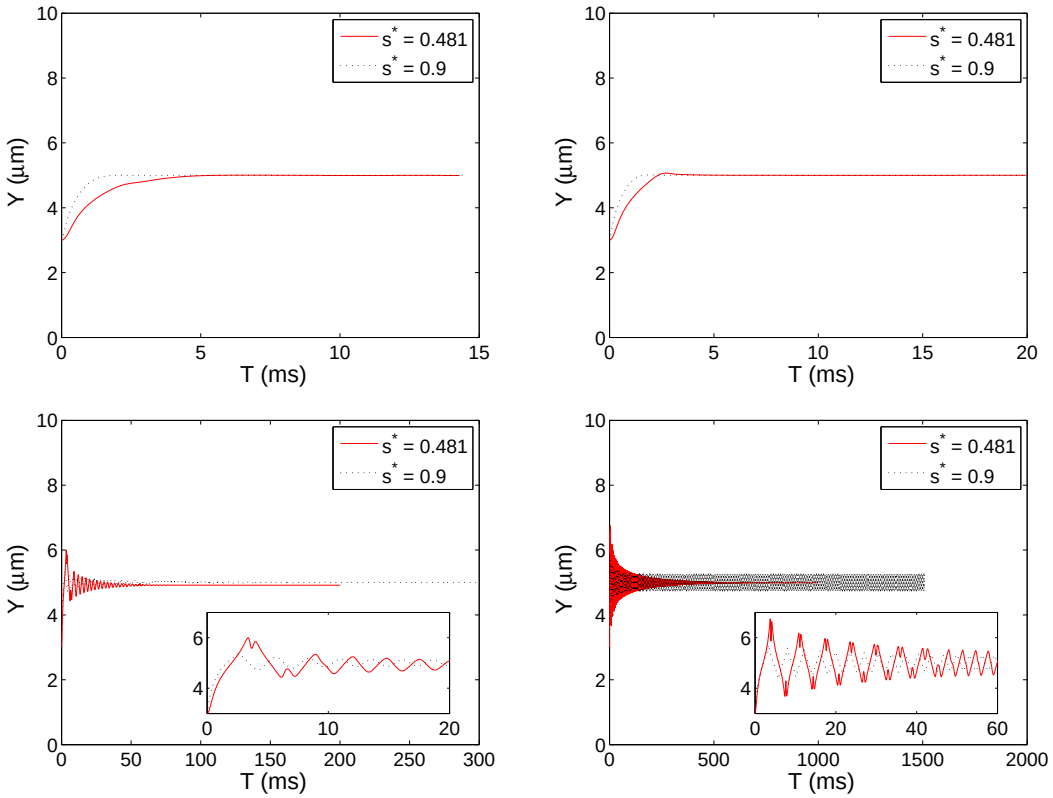

Figure 4.19: The history of the position of the cell mass center for $s^* = 0.481$ and 0.9 with different bending constants: $0.1k_b$ (top left), $1k_b$ (top right), $10k_b$ (bottom left), and $100k_b$ (bottom right). The initial position is (5,3) and the initial angle is 0.

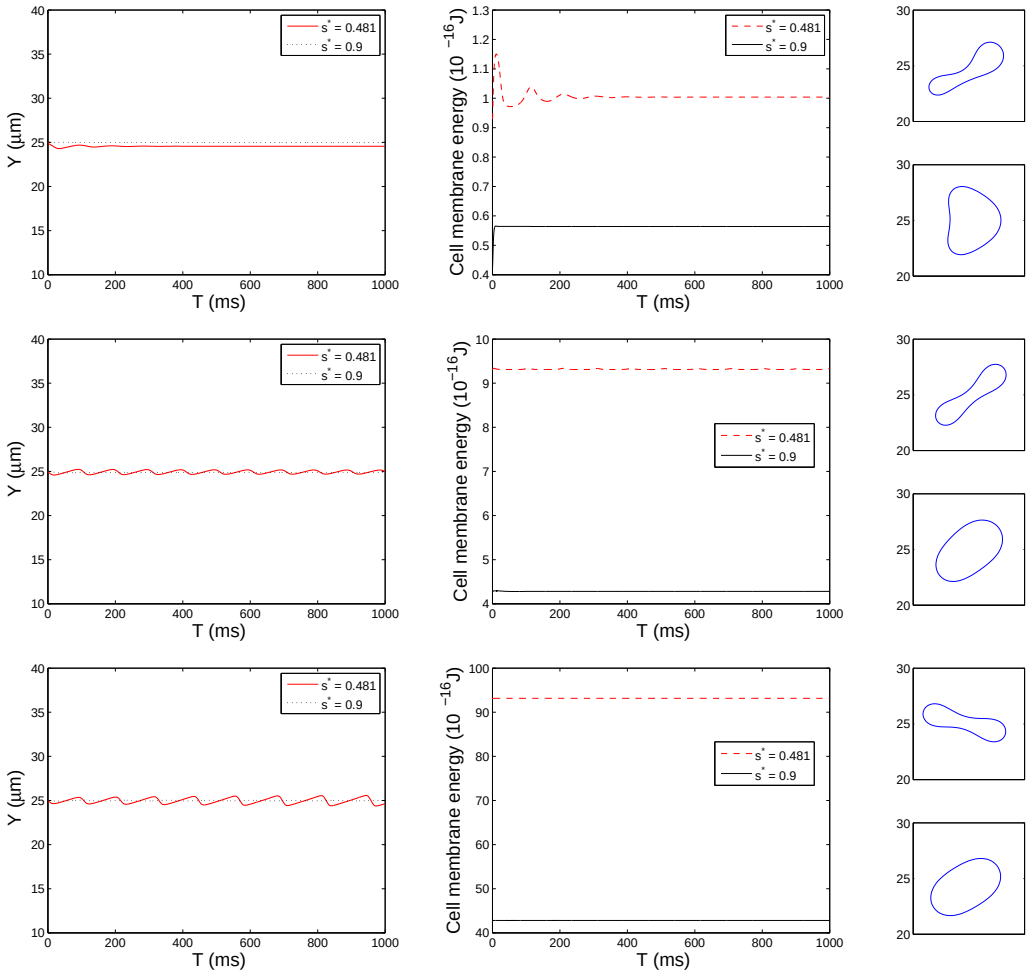

Figure 4.20: The history of the position of the cell mass center (left), the energy of the cell membrane (middle), and the equilibrium shape (right) for various bending constants: $0.1k_b$ (top), $1k_b$ (middle), and $10k_b$ (bottom).

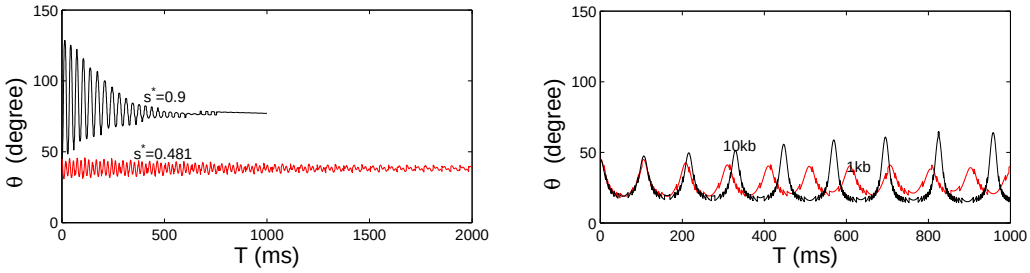

Figure 4.21: The history of the angle of the long axis of cell at the center line as a function of time: narrower channel (left) and wide channel (right).

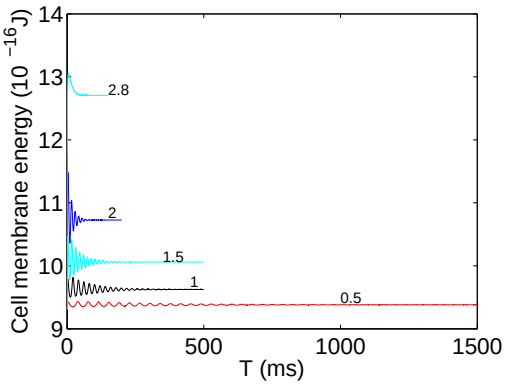

Figure 4.22: The cell membrane energy for $s^* = 0.481$ with different values $u_{\max} =$ 0.5, 1.0, 1.5, 2.0, and 2.8 cm/s.

4.2 Lateral migration and equilibrium shape and position of a single cell in bounded Poiseuille flows

In this section, the lateral migration properties of a single RBC in Poiseuille flows have been investigated by varying the swelling ratio (s^*), the membrane bending constant of RBC (k_b), the maximum velocity of fluid flow ($u_{\max}$), and the degree of confinement R_0/w. Two motions of oscillation and vacillating breathing (swing) of the RBC are observed in both narrow (100×10 μm^2) and wide (100×20 μm^2) channels considered here.

4.2.1 Initial position and angle tests

First, we consider the effect of the initial position and the initial angle φ of the long axis of the cell with respect to the center line on the lateral migration and equilibrium shape and position.

Given the same initial angle φ, the effect of different initial positions has been investigated in a Poiseuille flow with the fluid domain 100×20 μm^2. The pressure gradient is set to as a constant so that Re of the Poiseuille flow without cell is about 0.8333. The initial velocity is zero everywhere. The grid resolution for the computational domain is 64 grid points per 10 μm. Migrations of the RBC with s^* = 0.481, 0.9, and 1.0 for three different initial positions (5,3), (5,10), and (5,17) are shown in Figure 4.23. The cells with the initial positions (5,3) and (5,17) deform

and migrate to the center line of the microchannel where steady states are reached. The cell reaches a slipper shape for $s^* = 0.481$, a parachute shape for $s^* = 0.9$ and a slightly bullet-like shape as its equilibrium shape for the circular case of $s^* = 1.0$, respectively. The deformation of the cells with the initial positions (5,3) and (5,17) is greater than that with the initial position (5, 10) after the cells are placed in the fluid flow. The three cells with different initial positions migrate to the same equilibrium position and attain the same shape. The cell initial position does lead to different initial behavior, but the final position and shape are not related with the initial positions of the RBC.

The effect of the angle is also studied for both biconcave-shape cell with $s^* = 0.481$ and elliptic-shape cell with $s^* = 0.9$, respectively. Figure 4.24 presents the snapshots of the cell migration with the initial angles $\varphi = 0^o$, 45^o, and 90^o. By the combination effects of the wall and the deformability, the cell with $\varphi = 0^o$ deforms and rotates counterclockwise with an angle about 45^o, the cell with $\varphi = 90^o$ deforms and rotates clockwise with an angle about 45^o, and the cell with $\varphi = 45^o$ deforms and almost keeps the same angle. The deformation of the cells with the initial angles $\varphi = 0^o$ and 90^o is greater than that with the initial angle 45^o after the cells are released in the fluid flow. As shown in Figure 4.24, it takes almost the same time (5 ms) for these three cells with different initial angles to reach about the same shape and height in the flow. Then they keep migrating in the flow with no significant difference in shape and height. The initial angle has an influence on the cell initial behavior, but has no significant effect on its motion after its release into the fluid flow for a while.

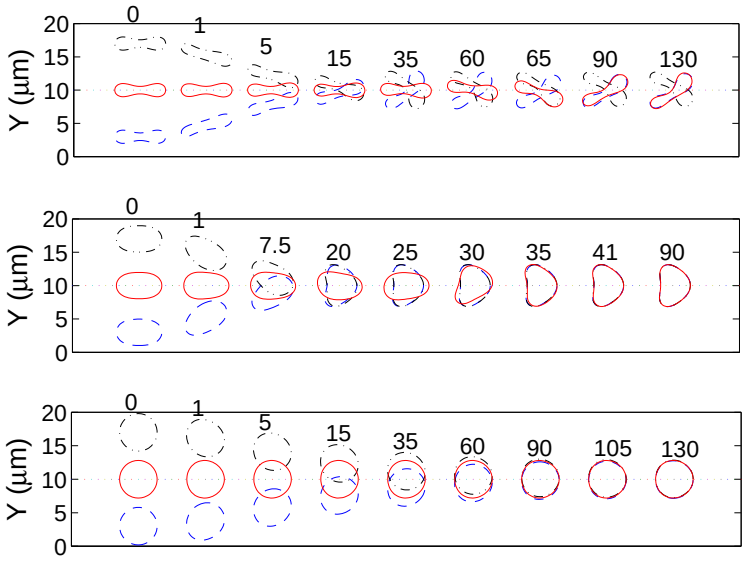

Figure 4.23: The snapshots of the cell migration with three different initial positions of $s^* = 0.481$ (top), 0.9 (middle), and 1.0 (bottom) at different time (ms).

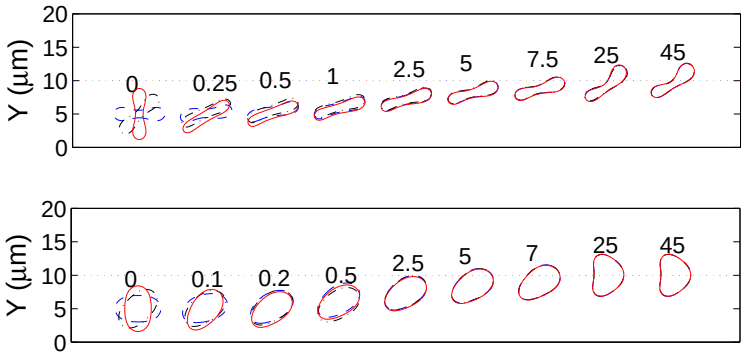

Figure 4.24: The snapshots of the cell migration with three different initial angles φ = 0°, 45°, and 90° of $s^* = 0.481$ (top) and 0.9 (bottom) at different time (ms).

4.2.2 Effect of the swelling ratio

Here we consider the effect of the swelling ratio on the lateral migration and equilibrium shape and position. Seven different shapes of the cells ($s^* = 0.481$, 0.6, 0.7, 0.8, 0.9, 0.95, and 1.0) have been studied and the simulation results are shown in Figure 4.25. The initial position of the mass center of the single cell is located at (5,3) as in Figure 4.24. The initial angle is $\varphi = 0$. The other parameters are kept the same as in Section 4.2.1. The cells deform after they are released close to the bottom wall and migrate toward a higher fluid velocity field, i.e., toward the center line of the channel, and reach their equilibrium shapes and positions, respectively. The average velocities of the fluid flow with the cells are 4.9562, 4.9546, 4.9528, 4.9504, 4.9501, 4.9515, and 4.953 cm/s for $s^* = 0.481$, 0.6, 0.7, 0.8, 0.9, 0.95, and 1.0, respectively. The associated Re are 0.826, 0.8258, 0.8255, 0.8251, 0.825, 0.8253, and 0.8255. While migrating, the biconcave-shape cell with $s^* = 0.481$, 0.6, 0.7, and 0.8 moves to a lateral location characterized by lower shear rates accompanied by damped vacillating-breathing (swing) motion. The damped speed is an inverse proportion function with the swelling ratio s^*. The equilibrium shapes for various swelling ratio are shown in Figure 4.25. The equilibrium positions are at or near the center line, and the distance Y_d is monotonic decreasing to zero with increasing the swelling ratio from 0.481 to 1.0 since the shape is changing from the asymmetric slipper shape to the symmetric shape. The energy stored in the cell membrane of the equilibrium cell is also monotonic decreasing with increasing the swelling ratio from 0.481 to 1.0. The extra energy due to the cell deformation shown in Figure 4.25 also indicates that the cell shape of $s^* = 0.8$ has been changed the most. As shown in

Figure 4.25, for $s^* > 0.8$, the speed of the migration at the beginning decreases with increasing the swelling ratio s^*. This result agrees very well qualitatively with the experimental results reported in [15]. But for $s^* \leq 0.8$, which has not been studied in [15], the speed of the migration at the beginning is an increasing function of the swelling ratio s^*. The critical swelling ratio $s^* = 0.8$ for having a biconcave shape also plays a role here for the migration velocity at the beginning. For $s^* > 0.8$, the deformability is weaker for a higher value of s^* due to the lack of the excess circumference. But for $s^* \leq 0.8$, the excess circumference is more than enough for the cell to deform, and the cell of larger s^* can interact more with the faster flow region due to the larger cell area and then migrates faster.

4.2.3 Effect of the membrane bending stiffness of RBC

To study the effect of the bending constant, we have kept the same values of k_l and k_s and considered four different values of the bending constants, $0.1k_b$, $1k_b$, $10k_b$, and $100k_b$, and other parameters are the same as in Section 4.2.2. The capillary numbers C_a are 135.337, 13.533, 1.353, and 0.135 corresponding to the bending constants $0.1k_b$, $1k_b$, $10k_b$, and $100k_b$, respectively. The snapshots of the cell migration in Poiseuille flows for $s^* = 0.481$, 0.9, and 1.0 with these bending constants are shown in Figure 4.26. The red asterisk denotes the same point on the cell membrane during the entire simulation. The histories of the position of the cell mass centers are displayed in Figure 4.27. For the above four bending constants, the cells migrate toward the equilibrium height close to the center line of the channel. Different deformability led by the different bending constants presents different dynamical

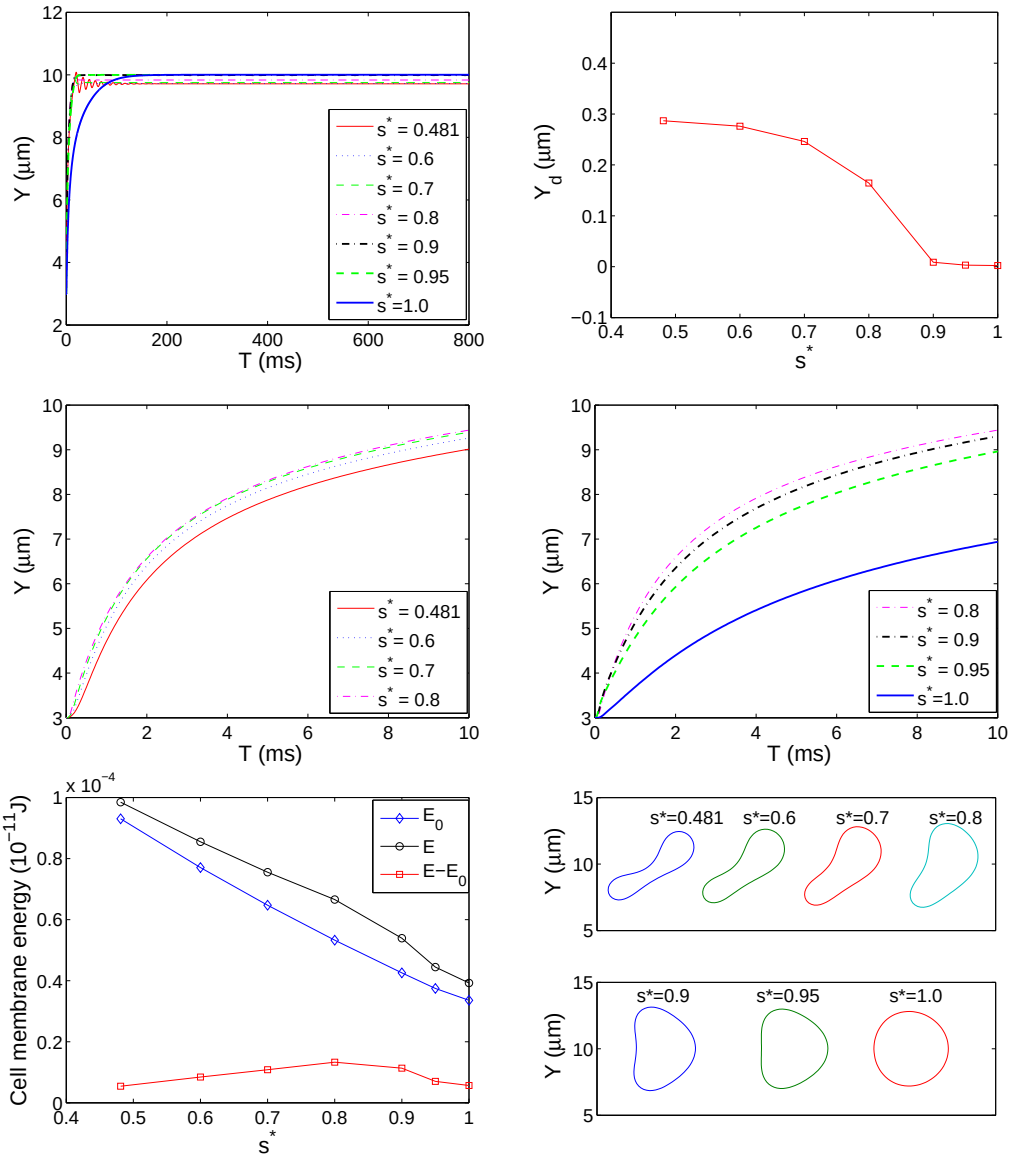

Figure 4.25: The history of the position of the cell mass center (top left) and the distance Y_d as a function of the swelling ratio s^* for the degree of confinement R_0/w = 0.28 (top right). The history of the position of the cell mass center at the beginning 10 ms of s^* = 0.481, 0.6, 0.7, and 0.8 (middle left) and s^* = 0.8, 0.9, 0.95, and 1.0 (middle right). The initial cell membrane energy E_0, the cell membrane energy of the equilibrium state E, and the energy difference $E - E_0$ (bottom left) and the equilibrium shapes for various swelling ratios s^* = 0.481, 0.6, 0.7, 0.8, 0.9, 0.95, and 1.0 (bottom right).

properties during the cell migration. For the lower bending constant $0.1k_b$, the cell with $s^* = 0.9$ migrates to the equilibrium height faster than the other two as shown in Figure 4.28. A parachute shape is obtained for both the biconcave-shape cell and the elliptic-shape cell, and a slightly bullet-like shape is observed for the circular-shape cell. For the bending constant $1k_b$, the cell with $s^* = 0.9$ also migrates faster to the equilibrium height. But both the biconcave-shape cell and the elliptic-shape cell exhibit damped vacillating breathing after they reach the center line of the channel as indicated in Figure 4.27. The equilibrium location of the biconcave-shape cell is about 0.2863 μm away from the center line due to its asymmetric equilibrium shape (slipper shape). For the bending constant $10k_b$, both the biconcave-shape cell and the elliptic-shape cell exhibit damped oscillation until they attain the equilibrium states, aligning themselves at an angle with the direction of the flow as shown in Figure 4.26 (g) and (h). The damping rate of the elliptic-shape cell is again bigger than that of the biconcave-shape cell as shown by the history of the angle θ in Figure 4.28 (left). For the bending constant $100k_b$, both two cells display damped oscillation with the shapes of long body as shown in Figures 4.26 (i) and (j) and 4.28 (right). The histories of the height of the cell mass center in Figure 4.27 do show the correlation with the oscillation motion.

Concerning the vacillating-breathing behavior in a Poiseuille flow, it was first observed without considering the lateral migration in [82]. To obtain this kind of behavior, the bending constant needs to be large enough with respect to the velocity $u_{\max}$ so that the cell can not be deformed into either a symmetric parachute or a bullet-like shape at the center line. In other words, the cell shape has to be a long

body shape in the central region of the channel as shown in Figure 4.26 $(d), (g)$, (h), (i), and (j) so that when the mass center of the cell moves up and down, its inclination angle oscillates since the portion of the membrane closer to the wall moves slower than that in the central region does. When the mass center finally settles to a steady height, the oscillation disappears.

And we also report the results of the distance Y_d as a function of Reynolds number (Re > 10) for various bending constants $1k_b$, $10k_b$, and $100k_b$ in Figure 4.29. The equilibrium position of the cell settles in the center line of the channel or between the center line and the wall. For the biconcave shape cell, the distance Y_d deceases as the bending constant increases. But Y_d increases as increasing the bending constant for both the elliptic cell and the circular cell. There is no distinguishing difference as it changes from $1k_b$ to $10k_b$ for the cell of $s^* = 0.481$ and 1.0. For both the elliptic shape cell and the circle cell, the distance Y_d increases with increasing Re, i.e., the equilibrium position shifts to the bottom wall, reaches a peak at about Re $= 40$ and decreases as Re increases (i.e. the equilibrium position shifts toward the center line). The similar results of the elliptical capsule are also obtained by Shin *et al.* in [83]. These simulation results may serve a useful application in separating cells that have same size but different bending constants via the bifurcation law, e.g. the Zweifach-Fung effect [31].

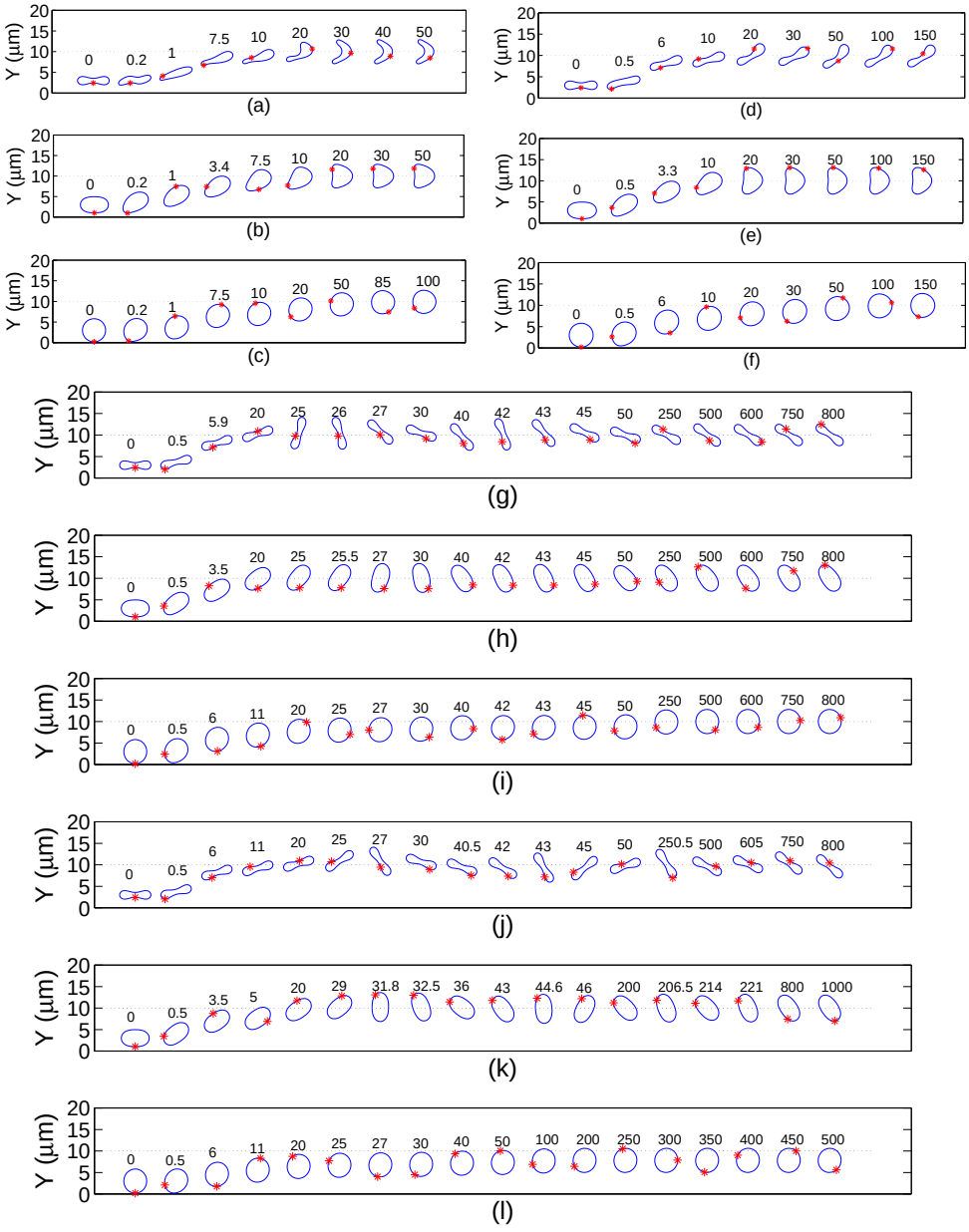

Figure 4.26: The snapshots of the cell migration in Poiseuille flows for $s^* = 0.481$, 0.9, and 1.0 with different bending constants at different time (ms): (a) $s^* = 0.481$ and $0.1k_b$, (b) $s^* = 0.9$ and $0.1k_b$, (c) $s^* = 1.0$ and $0.1k_b$, (d) $s^* = 0.481$ and $1k_b$, (e) $s^* = 0.9$ and $1k_b$, (f) $s^* = 1.0$ and $1k_b$, (g) $s^* = 0.481$ and $10k_b$, (h) $s^* = 0.9$ and $10k_b$, (i) $s^* = 1.0$ and $10k_b$, (j) $s^* = 0.481$ and $100k_b$, (k) $s^* = 0.9$ and $100k_b$, and (l) $s^* = 1.0$ and $100k_b$. The red asterisk denotes the same node point on the cell membrane.

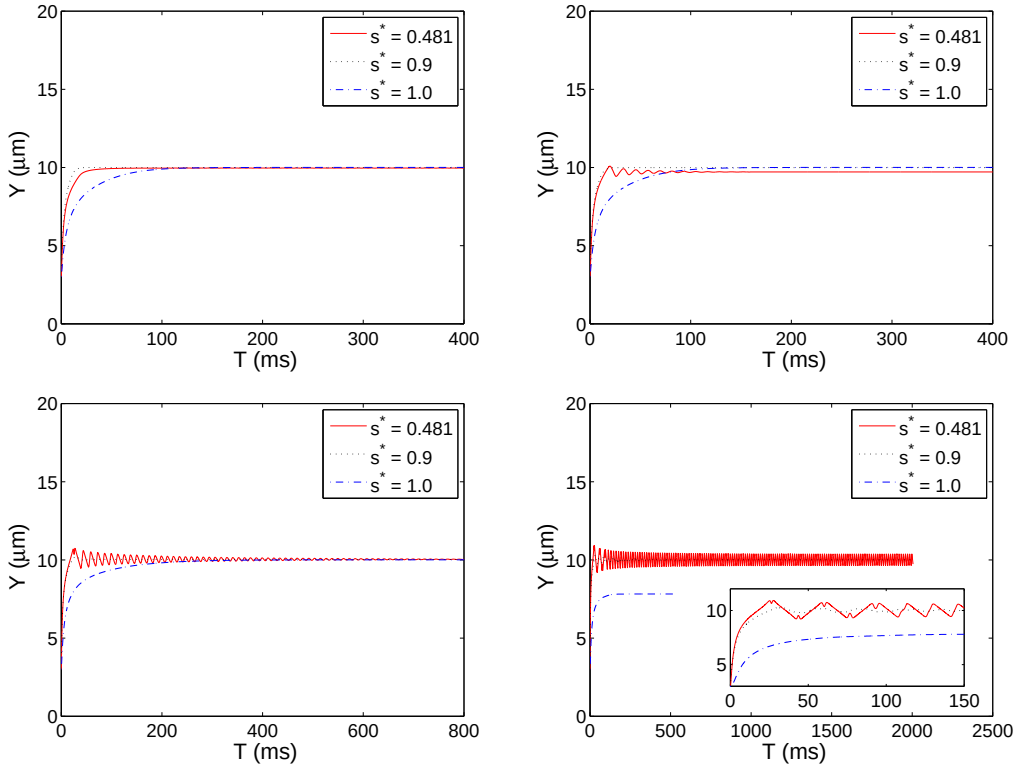

Figure 4.27: The history of the position of the cell mass center for various bending constants $0.1k_b$ (top left), $1k_b$ (top right), $10k_b$, and $100k_b$ (bottom right).

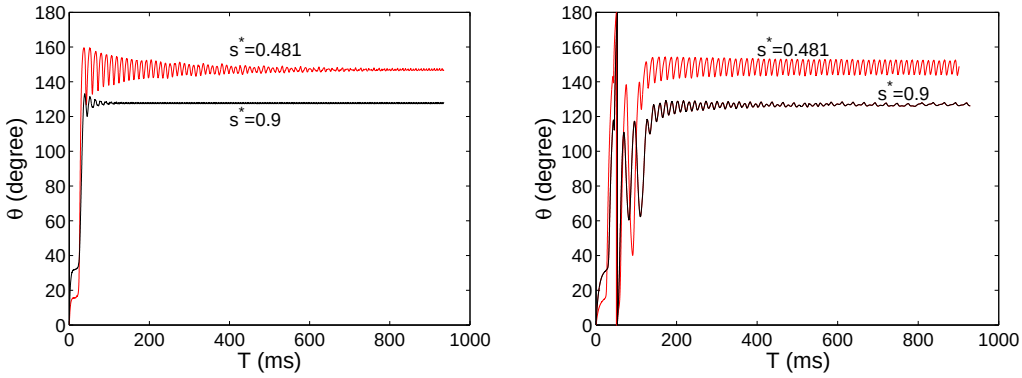

Figure 4.28: The history of the angle between the long axis of cell and the horizontal line for the bending constant $10k_b$ (left) and $100k_b$ (right).

4.2.4 Effect of the maximum velocity

The effect of $u_{\max}$ on the lateral migration and equilibrium shape and position of a single cell in Poiseuille flows has been investigated. In the simulations, we have kept other parameters the same as in Section 4.2.2. We observed that $u_{\max}$ plays a critical role on the migration, the deformation, the equilibrium position, and the shape of the cell. The higher the $u_{\max}$, the faster the cell deforms. So when the velocity of the cell migration is higher, it reaches the equilibrium shape and position more quickly. During the migration, both the biconcave-shape cell and the elliptic-shape cell exhibit a damped vacillating-breathing motion after the cell reached the center line of the channel for lower $u_{\max}$, and the vacillating-breathing motion damps out quickly for the elliptic-shape cell. When the equilibrium shape is symmetric with respect to the center line of the channel such as an ellipse, parachute shape, and bullet-like shape, the mass center lies in the center line of the channel; Otherwise,

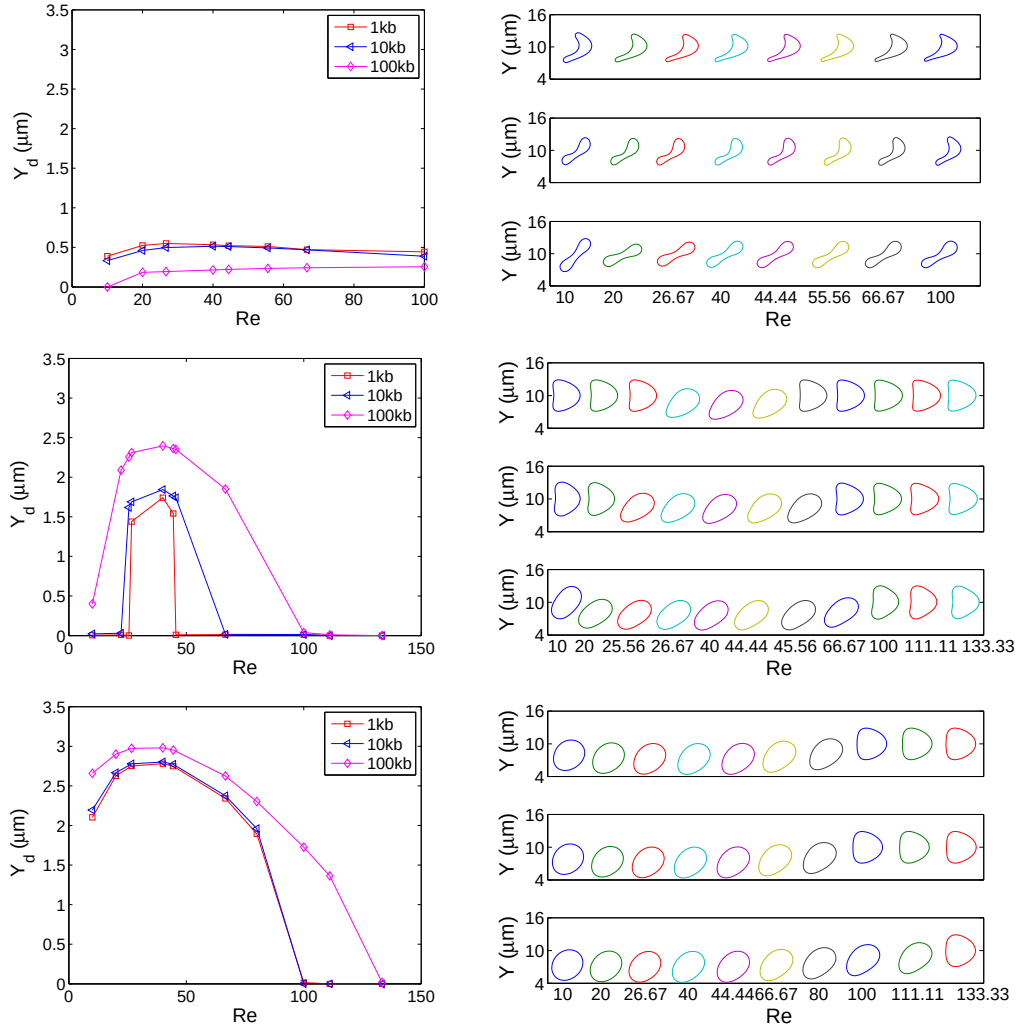

Figure 4.29: The distance Y_d between the cell mass center of the equilibrium position and the center line of the channel as a function of the Reynolds number Re for various bending constants $1k_b$, $10k_b$, and $100k_b$ of $s^* = 0.481$, 0.9, and 1.0 (from top to bottom, left). The equilibrium shapes of $s^* = 0.481$, 0.9, and 1.0 (from top to bottom, right) for different Re with the bending constants $1k_b$ (top one in each group), $10k_b$ (middle one in each group), and $100k_b$ (bottom one in each group).

when the equilibrium shape is asymmetric such as a slipper shape, the mass center settles between the center line and the wall. The histories of the cell mass centers are shown in Figure 4.30. The distance Y_d as a function of Re and the corresponding equilibrium shapes for three different swelling ratio $s^* = 0.481$, 0.9, and 1.0 are displayed in Figures 4.31 and 4.32, respectively.

For the biconcave-shape cell with $s^* = 0.481$, a slipper shape as its equilibrium shape is obtained for various $u_{\max}$. For the elliptic-shape cell with $s^* = 0.9$, a slipper shape as its equilibrium shape is observed for $u_{\max} < 7.5$ cm/s (Re < 0.83), a parachute shape as its equilibrium shape is observed for 7.5 cm/s $\leq u_{\max} \leq 230$ cm/s ($0.83 \leq$ Re ≤ 25.56) and $u_{\max} \geq 410$ cm/s (Re ≥ 45.56), and an asymmetric shape as its equilibrium shape is observed for 230 cm/s $< u_{\max} < 410$ cm/s ($25.56 <$ Re < 45.56). For the circular-shape cell with $s^* = 1.0$, a (slightly) bullet-like shape as its equilibrium shape is obtained for $u_{\max} < 60$ cm/s (Re < 6.67) and $u_{\max} \geq 900$ cm/s (Re ≥ 100), and an asymmetric shape as its equilibrium shape is observed for 60 cm/s $\leq u_{\max} < 900$ cm/s ($6.67 \leq$ Re < 100).

The asymmetric shape (slipper shape) of a vesicle in an unbounded Poiseuille flow at zero Re has been studied by Kaoui *et al.* [40], and similar results for a vesicle are mentioned in [75, 76, 84]. But the difference is that our simulation results show the cell of $s^* = 0.9$ and 1.0 can stay away from the center line with an asymmetric equilibrium shape with increasing value of $u_{\max}$ and then shift back to the center line with a symmetric parachute and bullet-like shape with enough higher $u_{\max}$ as shown in Figures 4.30 and 4.32. The above migration of the cell of $s^* = 0.9$ and 1.0 depends mainly on two lift forces in the narrow channel considered here: One is a positive

force toward the channel center generated by the inertial effect of the wall, and the other is a negative force toward the wall generated by the shear gradient of the Poiseuille flow. The cell migrates toward the channel center when $u_{\max}$ is very slow since, besides the cell deformability, the effect of the wall is stronger than that of the shear gradient of the flow, and then the positive lift force from the wall is larger than the negative lift force when the cell is closer to the wall. As $u_{\max}$ is larger, the effect of wall becomes weaker when comparing the effect of velocity profile of the fluid flow, the composite force becomes negative, and then the equilibrium position shifts away from the center line. When $u_{\max}$ increases further, the curvature of velocity profile of the fluid flow becomes very small, and the negative lift force generated by the shear gradient of the Poiseuille flow decreases. So the cell migrates to the center line of the channel for much higher $u_{\max}$ in a narrower channel considered here. The similar tendency for the capsule was reported in [83]. For a neutrally buoyant particle of an elliptic shape moving in a bounded Poiseuille flow, the mass center also moves to the center line when $u_{\max}$ is sufficiently higher in [13] for the same reason.

4.2.5 The effect of the degree of confinement

Finally, we compare the equilibrium position and shape of the RBC in Poiseuille flows by varying the degree of confinement. In this section, we consider two different degrees of confinement, $R_0/w = 0.56$ (100×10 μm^2) and 0.28 (100×20 μm^2), and six swelling ratios, $s^* = 0.481$, 0.6, 0.7 , 0.8, 0.9, and 1.0. Simulation results are reported in Figures 4.33 and 4.34 for these two degrees of confinement, respectively. In Figure 4.33, Re is between 0 and 0.5 for the degree of confinement $R_0/w = 0.56$.

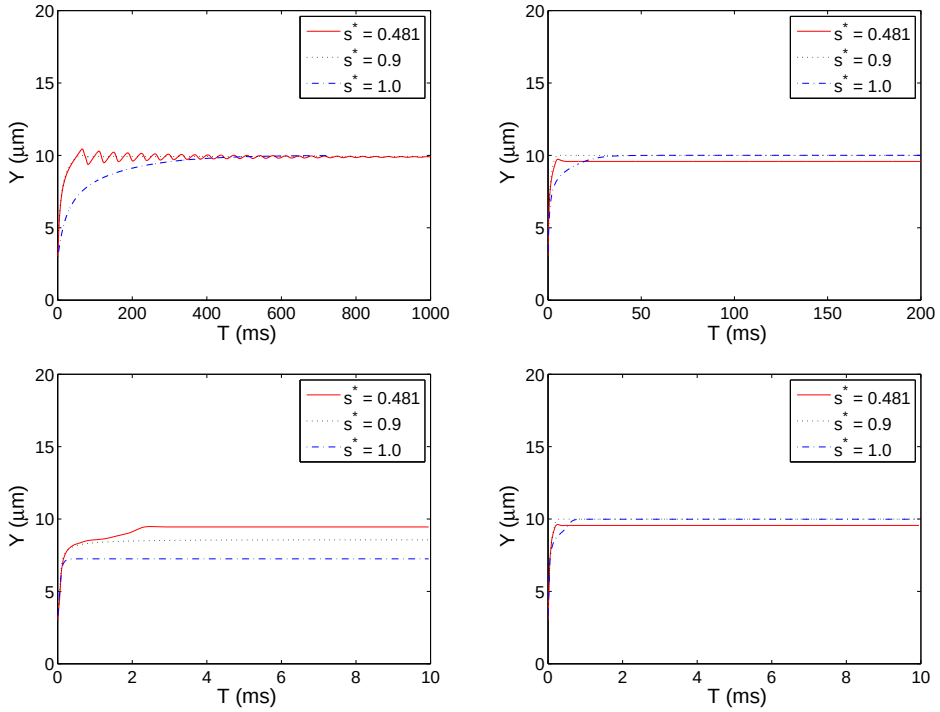

Figure 4.30: The history of the position of the cell mass center for various $u_{\max}$ = 2.5 (top left), 30 (top right), 240 (bottom left), and 900 cm/s (bottom right). The associated Re are 0.278, 3.33, 26.67, and 100.

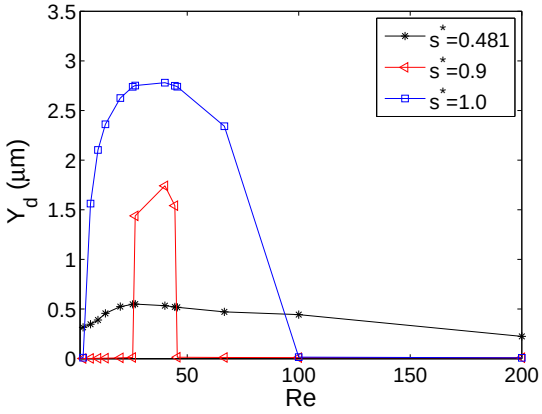

Figure 4.31: The distance Y_d between the cell mass center of the equilibrium position and the center line of the channel as a function of Re.

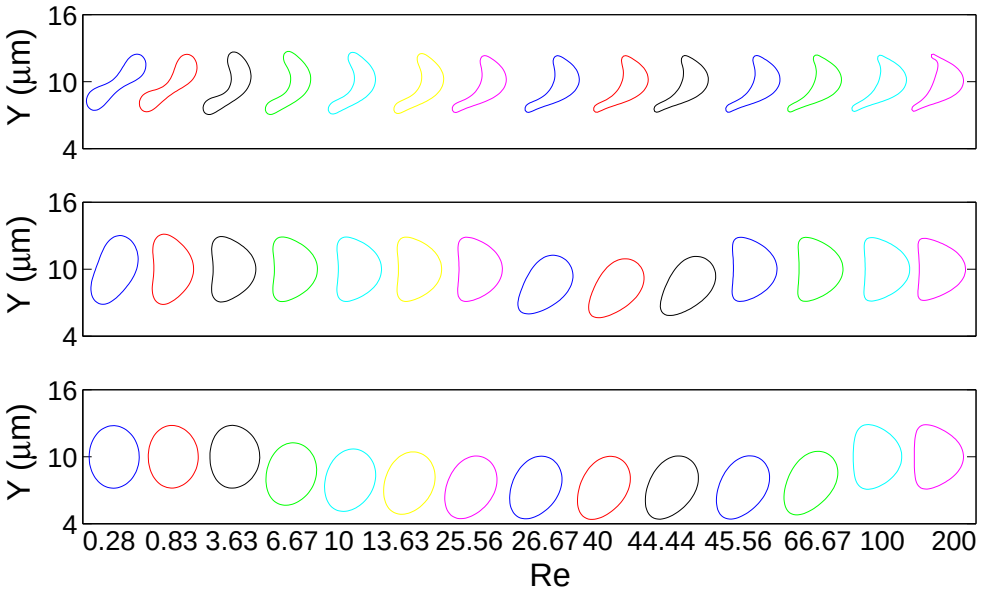

Figure 4.32: The equilibrium position and shape of $s^* = 0.481$, 0.9, and 1.0 (from top to bottom) with the $u_{\max} = 2.5$, 7.5, 30, 60, 90, 120, 230, 240, 360, 400, 410, 600, 900, and 1800 cm/s (from left to right) and associated Re are 0.28, 0.83, 3.33, 6.67, 10, 13.33, 20, 26.67, 40, 44.44, 45.56, 66.67, 100, and 200.

The distance Y_d increases with increasing Re and reaches a peak, then decreases with increasing Re for $s^* = 0.481$, 0.6, 0.7, and 0.8. The peak of Re (0.1389, 0.1111, 0.0833, and 0.0694) is a decreasing function of the swelling ratio s^* (0.481, 0.6, 0.7, and 0.8). After the distance Y_d reaches its peak, the cell equilibrium position shifts back to the center line of the channel and the equilibrium shape becomes a parachute shape for $s^* \leq 0.9$ and a bullet-like shape for $s^* = 1.0$. The diagram of the equilibrium shape in Figure 4.33 is similar to the simulation results in [40]. In Figure 4.34, Re is between 0 and 5 for a smaller degree of confinement $R_0/w = 0.28$. The distance Y_d increases with increasing Re and reaches a peak, then decreases with increasing Re for $s^* = 0.481$, 0.6, 0.7 , and 0.8. The peak of Re (2.222, 1.333, 0.833, 0.667, and 0.444) is a decreasing function of the swelling ratio s^* (0.481, 0.6, 0.7, 0.8, and 0.9). The distance Y_d is almost zero for the swelling ratio $s^* = 1.0$ due to its symmetric shape. For the wider channel, it needs higher $u_{\max}$ to obtain a symmetric shape for the cell of smaller values of the swelling ratio s^*, especially for the one of $s^* = 0.481$. It indicates that the degree of confinement is also important for the equilibrium shape in a bounded Poiseuille flow. In general, for the bigger degree of confinement, the distance Y_d is highly related to the equilibrium shape: Y_d is zero for the symmetric equilibrium shape such as a parachute shape and a bullet-like shape, but Y_d is nonzero for the asymmetric equilibrium shape such as a slipper shape.

Given a swelling ratio s^*, the cell membrane energy of the equilibrium position is an increasing function as Re increases. The slipper-shape cell is more stable than the parachute-shape one in the sense that the energy stored in the former is lower than that in the latter. The fluid flow with higher $u_{\max}$ can provide enough energy

to sustain a parachute chape. This is another way to explain why the slipper shape is a favorable shaoe in a narrow Poiseuille flow with low flow velocity besides the explanation based on reducing the lag by assuming a slipper shape discussed in [40]. For a given Re, the bigger the swelling ratio ($s^* < 1.0$), the lower the cell membrane energy. The membrane energy of the cell of $s^* = 1.0$ behaves differently from the others for the both degrees of confinement considered here. The corresponding equilibrium shapes of the various swelling ratios $s^* = 0.481$, 0.6, 0.7 ,0.8, 0.9, and 1.0 are shown in Figure 4.33 (bottom).

4.2.6 Conclusions

In this section, inertial migration and equilibrium position and shape of a cell with different initial shape (convex and biconcave) in bounded two-dimensional Poiseuille flows have been studied by numerical simulation. Several important factors have been examined for the inertial migration of a single RBC in Poiseuille flows: the swelling ratio (s^*), the membrane bending stiffness of RBCs (k_b), the maximum velocity of fluid flow ($u_{\max}$), and the degree of confinement (the ratio of the cell's effective radius R_0 to the channel half height w). The combined effect of the deformability, the degree of confinement, and the shear gradient of the Poiseuille flow make the RBC migrate toward a certain cross-sectional equilibrium position, which lies either on the center line of the channel or off center line. For $s^* > 0.8$, the speed of the migration at the beginning decreases with increasing the swelling ratio s^*. But for $s^* < 0.8$, the speed of the migration at the beginning is an increasing function of the swelling ratio s^*. Two motions of oscillation and vacillating breathing (swing) of RBC are observed.

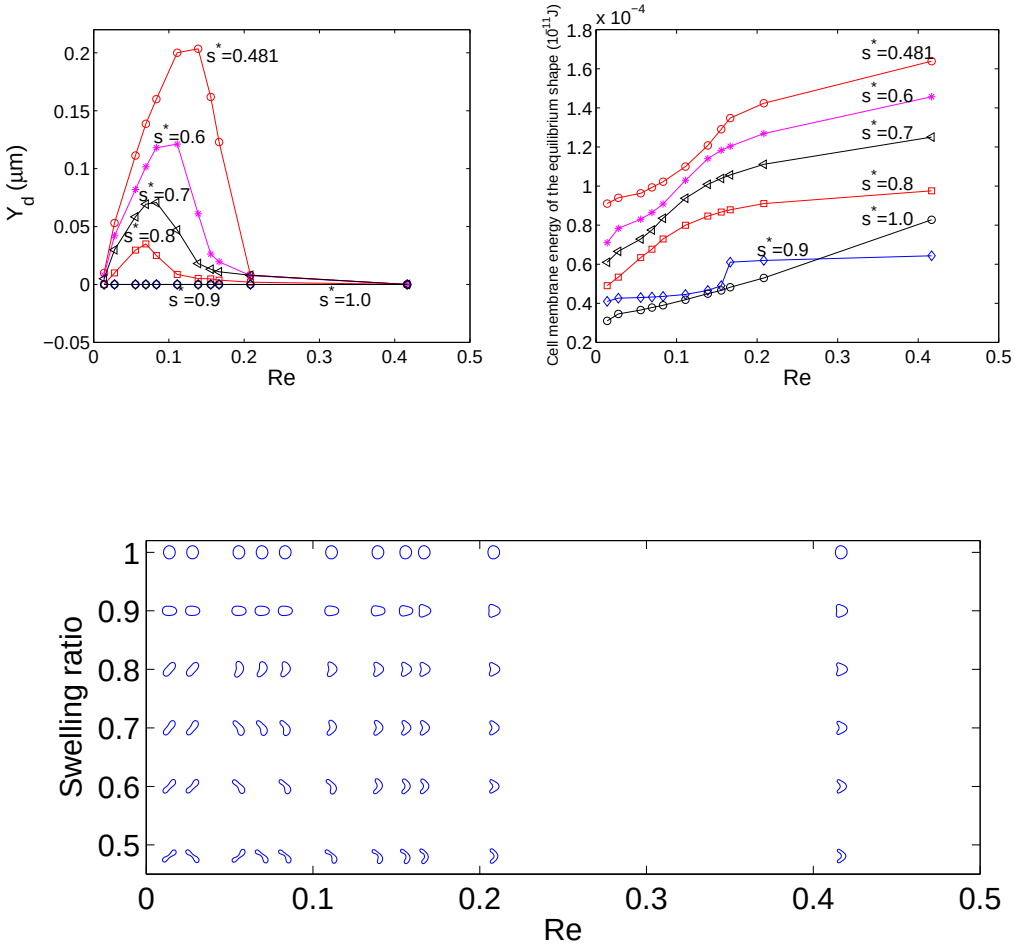

Figure 4.33: The distance Y_d between the cell mass center of the equilibrium position and the center line of the channel as a function of Re (top left), the cell membrane energy of the equilibrium position as a function of Re (top right), and the corresponding equilibrium shapes of the various swelling ratios $s^* = 0.481$, 0.6, 0.7 ,0.8, 0.9, and 1.0 (bottom). $R_0/w = 0.56$.

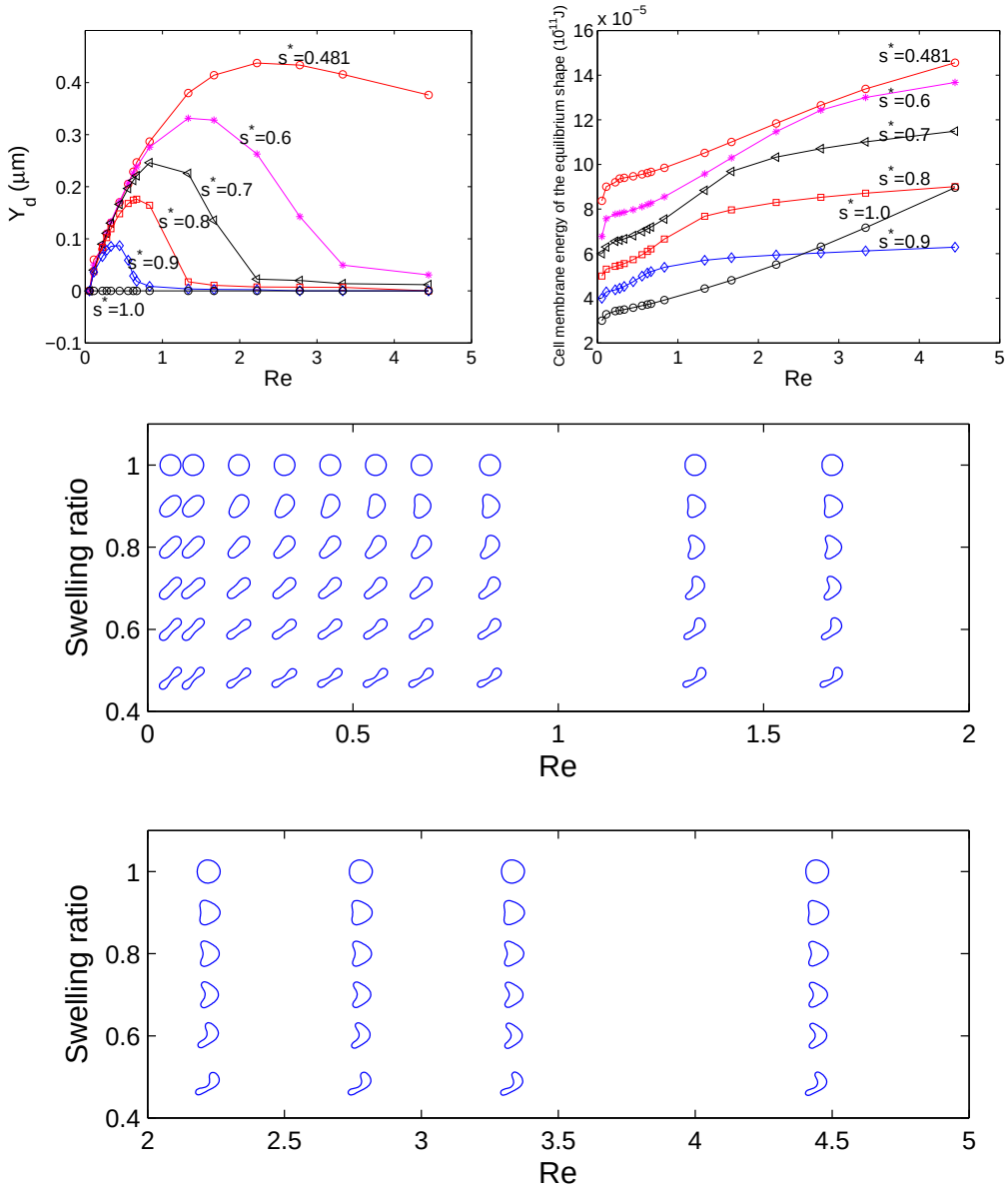

Figure 4.34: The distance Y_d between the cell mass center of the equilibrium position and the center line of the channel as a function of Re (top left), the cell membrane energy of the equilibrium position as a function of Re (top right), and the corresponding equilibrium shapes of the various swelling ratios $s^* = 0.481$, 0.6, 0.7 ,0.8, 0.9, and 1.0 (bottom). $R_0/w = 0.28$.

The distance Y_d between the cell mass center of the equilibrium position and the center line of the channel increases with increasing Re and reaches a peak, then decreases with increasing Re. The peak of Re is a decreasing function of the swelling ratios ($s^* < 1.0$). The distance Y_d is almost zero for s^*=1.0. Given a swelling ratio s^*, the cell membrane energy of the equilibrium position is an increasing function as Re increases. The slipper-shape cell is more stable than the parachute-shape one since the energy stored in the former is lower than that in the latter. For a given Re, the bigger the swelling ratio ($s^* < 1.0$), the lower the cell membrane energy. The deformability of cell is harder for the bigger swelling ratio because the excess perimeter is less.

4.3 Four cell migration in Poiseuille flows

To study the effect of the deformability on the migration of the cell, we have considered the case of four cells with $s^* = 1$ (i.e. the radius is 2.8 μm) in a Poiseuille flow so that we can compare their motions with the computational results of four neutrally buoyant disks of the same area obtained by the DLM/FD method described in [64]. Then we have compared the results with those of $s^* = 0.7$ to study the effect of the swelling ratio on the lateral migration.

In the simulations, we have kept the same values for k_l and k_s as in Section 4.2.2 and considered five different values of the bending constant, namely $0.1k_b$, $1k_b$, $10k_b$, $100k_b$, and $1000k_b$. The fluid domain is a 100×50 μm^2 rectangle. The pressure drop is set as a constant for this study so that the Reynolds number of the Poiseuille flow without cells is 2.778. The initial velocity is zero everywhere. The initial shapes of the cells we consider are circle with the swelling ratio $s^* = 1$. The initial position of the mass centers of the four cells are at (25,10), (25,40), (65,10), and (65,40). The histories of the height of the mass centers of the cells in the channel with different values of bending constants k_b are shown in Figure 4.35. The Reynolds numbers based on the averaged velocity of the flow with five cells are 2.7109, 2.7103, 2.7057, 2.6852, and 2.6746 for the bending constants $0.1k_b$, $1k_b$, $10k_b$, $100k_b$, and $1000k_b$, respectively.

The cells with $s^* = 1$ move slowly toward the central region of the bigger channel at the beginning 100 ms, and then set their equilibrium positions between the wall and the center line of the channel. In Figure 4.35, the averaged distances of the mass

centers of the five cells to the central line of the channel for the finally relative steady states are 9.06, 9.18, 9.58, 11.20, and 12.05 μm for the bending constants $0.1k_b$, $1k_b$, $10k_b$, $100k_b$, and $1000k_b$, respectively. Thus the migration of four cells with $s^* = 1$ in a Poiseuille flow depends on the strength of the bending property of the cells. The shapes and the positions of the four cells at $t = 500$ ms are also shown in Figure 4.35. For the case of the bending constants $0.1k_b$, $1k_b$, $10k_b$, and $100k_b$, the equilibrium shapes of the four cells are not circular at $t = 500$ ms. When the bending constant is $1000k_b$, the four almost circular cells behave like four neutrally buoyant disks of radius 2.8 μm moving in a Poiseuille flow. Via the DLM/FD method described in [64], the averaged distance of the mass centers of the four neutrally buoyant disks to the central line is 12.73 μm, which is in good agreement with the distance for the case of $1000k_b$. The results of the four neutrally buoyant disks obtained by the DLM/FD method can be found in Figure 7 in [80]. For the case of the four cells with $s^* = 0.7$ shown in Figure 4.36, the combined effect of the deformability, the degree of confinement, and the shear gradient of the Poiseuille flow make the cells migrate toward the center line of the channel. The Reynolds number based on the averaged velocity and the channel height is Re = 2.76. There is a big difference between the results of $s^* = 1$ and those of $s^* = 0.7$, the cells with $s^* = 1$ lack of the deformability so that they can not migrate to the center line of the channel, and the distance between the cell mass center of the center line of the channel depends on the bending constant of the cell membrane. But for the cells with $s^* = 0.7$, due to their deformability and that the effect of the flow inertia is weaker, they easily move to the central region of the channel. Hence, the interplay between the wall effect,

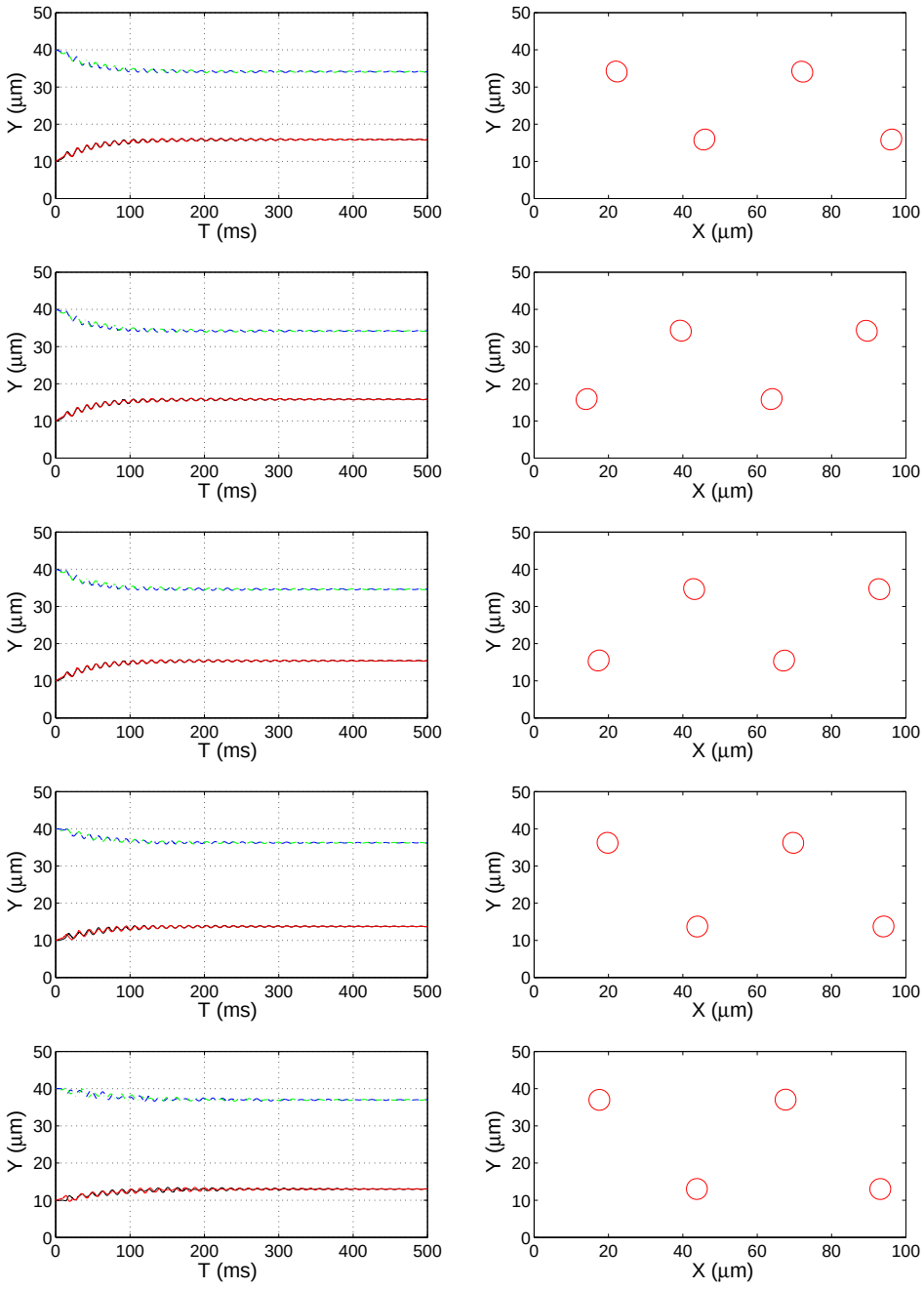

Figure 4.35: Histories of the height of the mass centers (left) and shapes and positions of four cells (right) at $t = 500$ ms with different bending constants $0.1k_b$, $1k_b$, $10k_b$, $100k_b$, and $1000k_b$ (from top to bottom) .

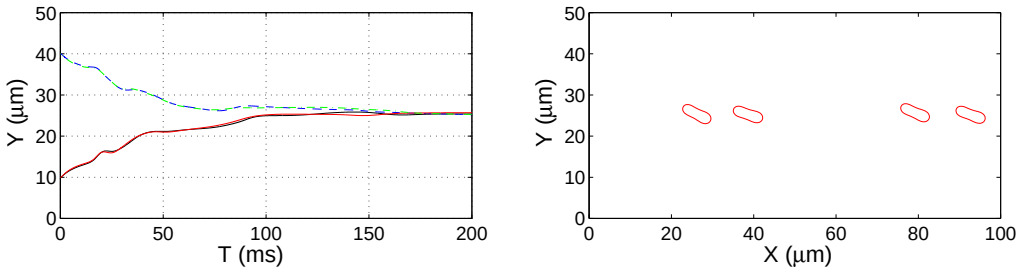

Figure 4.36: Histories of the height of the mass centers (left) and shape and position of four cells (right) at $t = 200$ ms in a Poiseuille flow with $s^* = 0.7$.

deformation, and inertia forces has strong influence on the cell lateral migration rate.

We have noticed that the four cells become staggered as shown in Figure 4.35. One reason for having this kind of patterns is that the initial positions of the four cells are not stable since particles do not move side by side in Newtonian fluids, the force on each particle makes them move away from each other (see, e.g. [2]).

4.4 Migration of many cells in Poiseuille flows

4.4.1 Migration of many cells in a wide channel

To apply the methodology to many-cell cases, we have considered the cases of 50 and 100 RBCs with $s^* = 0.7$ in a Poiseuille flow. We have used the same values for k_b, k_l, and k_s as in Section 4.2.2. The fluid domain is a 100×50 μm^2 rectangle. Hence the hematocrit (Hct) of the 50 cell case (resp., 10 cell case) is 17.24% (resp., 34.48%). The pressure gradient is set as a constant for this study so that the Reynolds number

of the Poiseuille flow without cells is 2.778. The initial velocity is zero everywhere. The time step is 10^{-5} ms. The positions and shapes of cells at different times are shown in Figures 4.37 and 4.39. We have observed that the cells move toward the center of the channel, an effect attributed to their deformability. Similar two-dimensional results have been observed numerically in [5, 16]. There are cell-free layers next to the walls as shown in Figures 4.37 and 4.39. The associated velocity fields and shapes and positions of the finally relative steady states are displayed in Figures 4.38 and 4.40, respectively. The averaged velocity profiles of the fluid flow with cells as shown in Figure 4.43 (left) have blunt shapes due to the aggregation of the cells in the central region. In [10], the cell-free layer has been estimated to be roughly 100/Hct in cylindrical tubes with diameters between 40 and 83 μm. In [16], the numerical results of the size of the cell-free layer in two-dimensional Poiseuille flows are in good agreement with the above estimation reported in [10]. Thus for Hct = 17.24 %, the estimation of the cell-free layer is about 5.8 μm (2.9 μm for the Hct = 34.48 % case). We have computed the size of the cell-free layer by averaging the gap size between the wall and the closest cell to the wall for the last millisecond of the simulation. Our results show the sizes of the cell-free layer are about 6.24 and 2.94 μm for the Hct = 17.24 % and Hct = 34.48 %, respectively, which are in good agreement with the estimation in [10]. The Reynolds numbers Re and the capillary numbers C_a for the 50 cell case and 100 cell case are displayed in Table 4.1.

Then we have considered the cases where the averaged velocity is reduced to $U =$ 3.333 cm/s and all other parameters are kept the same as the beginning of this section. The positions and shapes of cells are shown in Figure 4.41. The associated velocity

Hct	Re	C_a
17.24 %	2.34	7.23
34.48 %	1.59	7.24

Table 4.1: The Reynolds numbers Re and the capillary numbers C_a for the 50 cell case and 100 cell case, respectively. $U = 6.67$ cm/s.

Hct	Re	C_a
17.24 %	1.17	3.61
34.48 %	0.82	3.62

Table 4.2: The Reynolds numbers Re and the capillary numbers C_a for the 50 cell case and 100 cell case, respectively. $U = 3.33$ cm/s.

fields and shapes and positions of the finally relative steady states are displayed in Figures 4.41 and 4.42, respectively. The averaged velocity profiles of the fluid flow with cells as shown in Figure 4.43 (right) have blunt shapes due to the aggregation of the cells in the central region. The computational results show the averaged size of cell-free layer is about 5.92 μm (resp., 2.97 μm) for the Hct = 17.24% case (resp., the Hct = 34.48% case), which are in agreement with the estimation in [10]. The Reynolds numbers Re and the capillary numbers C_a for the 50 cell case and 100 cell case are displayed in Table 4.2.

In Figures 4.37, 4.39, and 4.41, the orientation of cells has shown some symmetry with respect to the center line of the channel. Since the two channel walls are at rest, the cell located between the center line and a wall is in a kind of "nonlinear shear" flow. Hence the motion and inclination angles of those cells are similar to the behavior of cell migrating in a "linear shear" flow between two parallel plates, which is that the cell migrates to the center line with an inclination angle related to the swelling ratio of the cell.

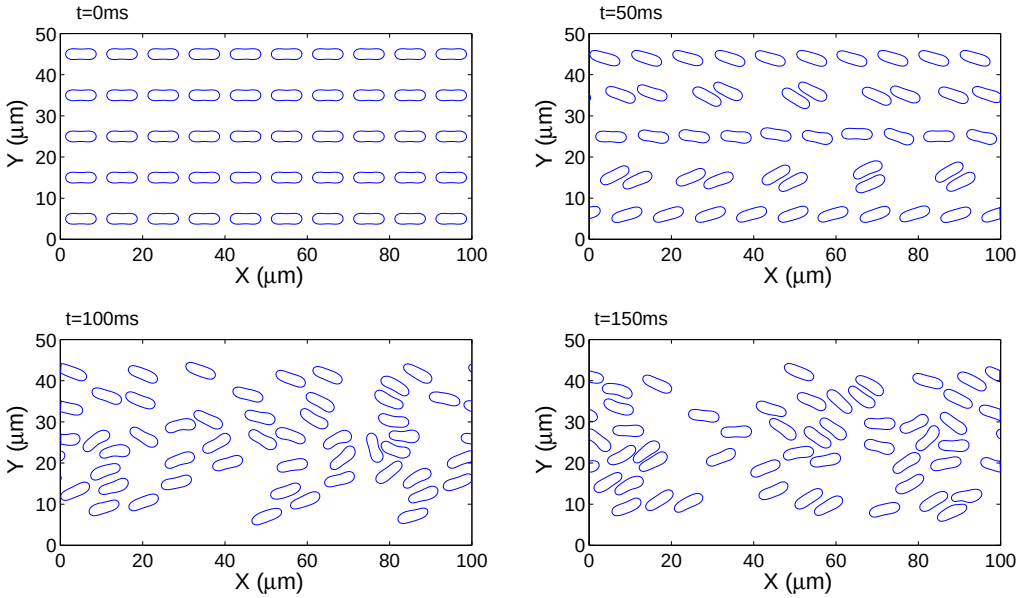

Figure 4.37: Shapes and positions of 50 cells at $t = 0$, 50, 100, and 150 ms for $U = 6.67$ cm/s.

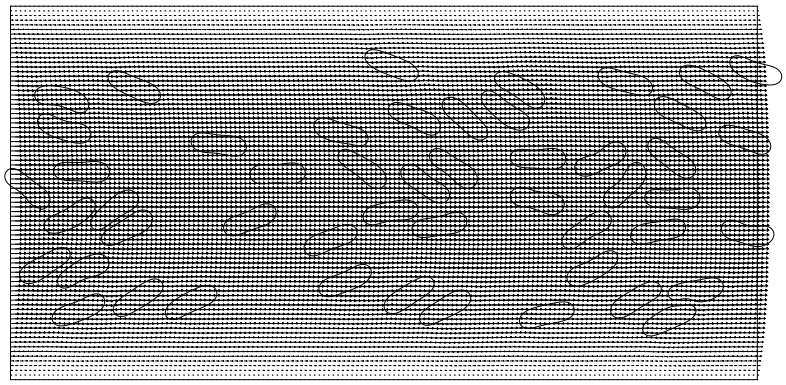

Figure 4.38: Velocity field and shapes and positions of 50 cells at $t = 150$ ms for $U = 6.67$ cm/s.

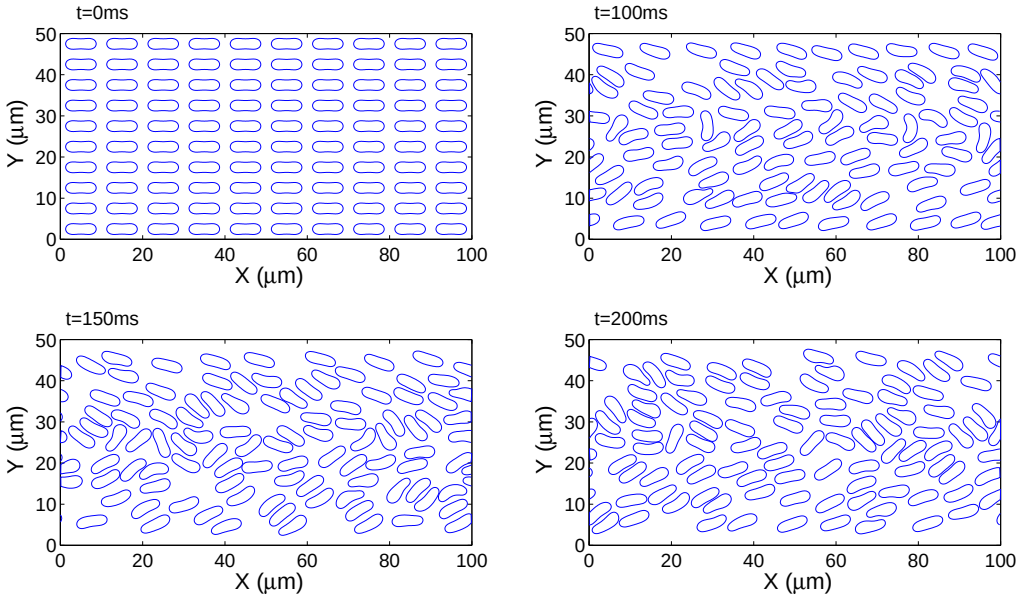

Figure 4.39: Shapes and positions of 100 cells at $t = 0$, 100, 150, and 200 ms for $U = 6.67$ cm/s.

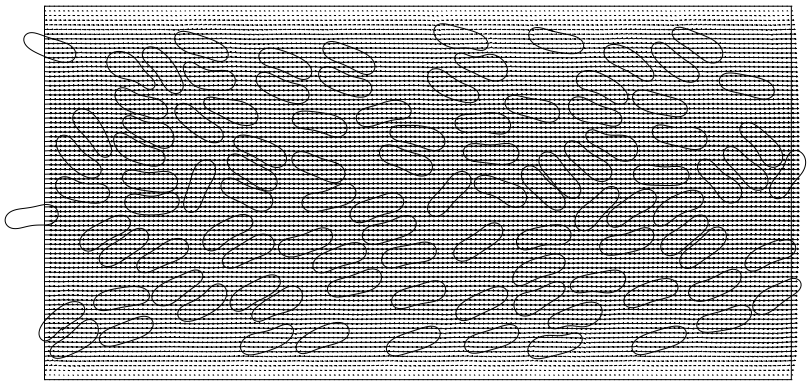

Figure 4.40: Velocity field and shapes and positions of 100 cells at $t = 200$ ms for $U = 6.67$ cm/s.

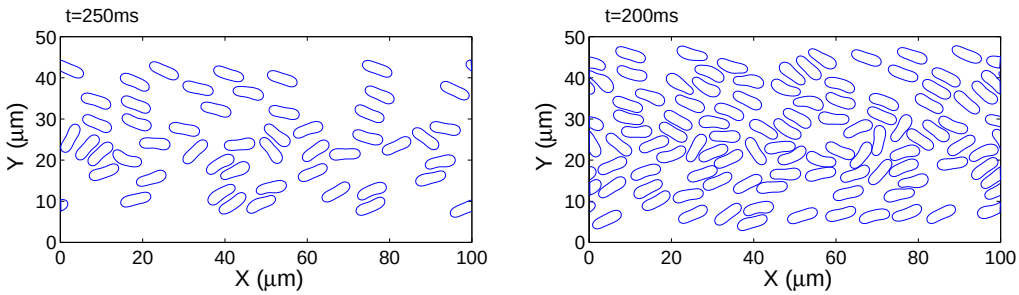

Figure 4.41: Shapes and positions of 50 cells at $t = 250$ms (left) and those of 100 cells at $t = 200$ms (right) for $U = 3.33$ cm/s.

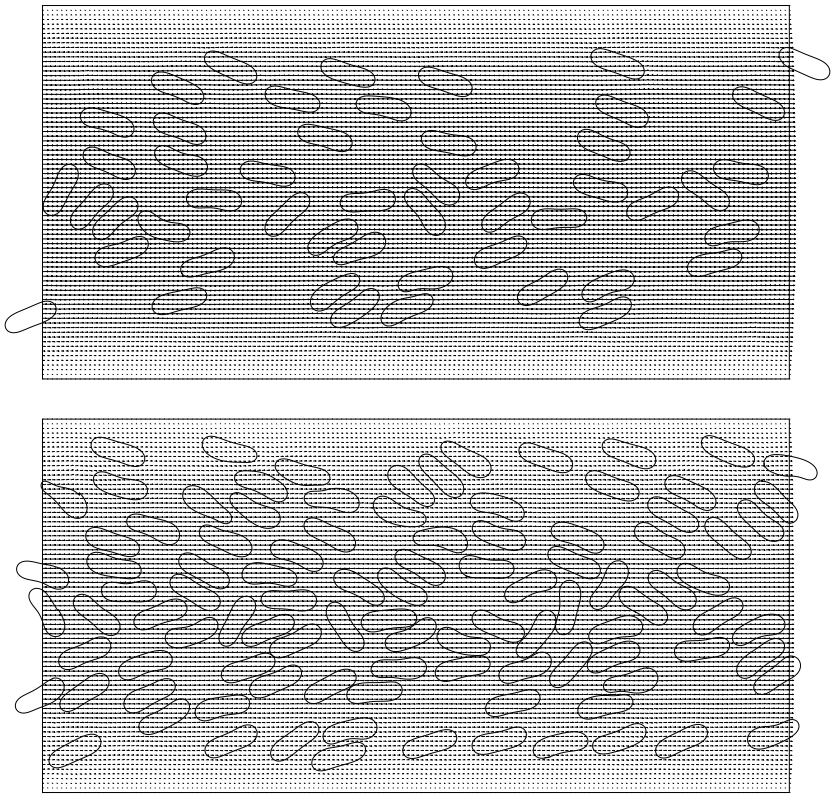

Figure 4.42: Velocity field and shapes and positions of 50 cells at $t = 250$ ms (top) and 100 cells at $t = 200$ ms (bottom) for $U = 3.33$ cm/s.

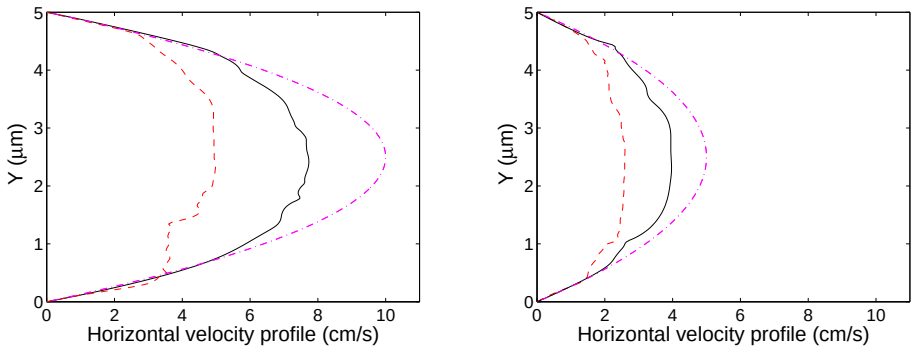

Figure 4.43: Distribution of the horizontal velocity of the fluid flow with cells at the relative stable states for 50 cells (black solid line) and 100 cells (red dashed line) for $U = 6.67$ cm/s (left) and $U = 3.33$ cm/s (right). The magenta dashdot line denotes the associated velocity distribution of the steady state fluid flow without cells.

4.4.2 Migration of many cells in a curved boundary channel

We also study the migration of many cells in curve boundary channel and the effect of the curve boundary on the size of the cell-free layer. In this section, the computational domain is a 100×60 μm^2 rectangle. The regions of the constriction shown in Figures 4.44 and 4.46 are given by the functions f_{t} and f_{b} for the top curve boundary and the bottom curve boundary, respectively (see Table 4.3). So Hct = 17.24% for both two cases. The initial velocity is zero everywhere. The time step is 10^{-5} ms. The positions and shapes of cells at different times are shown in Figures 4.44 and 4.46. We have observed that the cells move toward the center of the channel, an effect attributed to their deformability. There are cell-free layers next to the walls as shown in Figures 4.44 and 4.46. We have computed the size of the cell-free layer by averaging the gap size between the wall and the closest cell to the wall for the last millisecond of the simulation. Our results show the sizes of the cell-free layer are

Case	f_{t}	f_{b}
I	$2.5\cos(2x\pi/5)+55$	$2.5\sin(2x\pi/5)+5$
II	$2.5\cos(x\pi/5)+55$	$2.5\sin(x\pi/5)+5$

Table 4.3: The functions f_{t} and f_{b} for the top and bottom curve boundary, respectively.

Case	U_{avg}(cm/s)	$H_{\mathrm{avg}}(\mu\mathrm{m})$	$\mathrm{Re}=\rho U_{\mathrm{avg}}H_{\mathrm{avg}}/\mu$
I	1.53	50	0.638
II	1.634	50	0.681

Table 4.4: The averaged velocity of the fluid flow with cells U_{avg} , the averaged width of the channel H_{avg}, and the Reynolds number Re for Case I and Case II .

about 6.01 and 6.43 μm for the Figures 4.44 and 4.46, respectively. The Reynolds numbers based on the averaged velocity of the fluid flow with cells and the averaged width of the channel are displayed in Table 4.4. The averaged width of the channel for both two case are same, the Reynolds number of the case II is bigger than that of the case I since the averaged velocity of the fluid flow with cells of the case II is higher than that of the case I. The computational results show that the channel boundary (straight or curve) has no effect on the size of the free-cell layer.

4.4.3 Migration of many cells in a narrow channel

In this section, we have investigated the migration of many cells in a narrow channel and consider the effect of the bending constant of the cell membrane k_b on the size of the cell-free layer. The computational domain is a 100×25 $\mu\mathrm{m}^2$ rectangle. Hence the Hct = 23.69% (resp., 34.48%) for the value of $s^* = 0.481$ (resp., $s^* = 0.7$). The pressure gradient is set as a constant for this study so that the

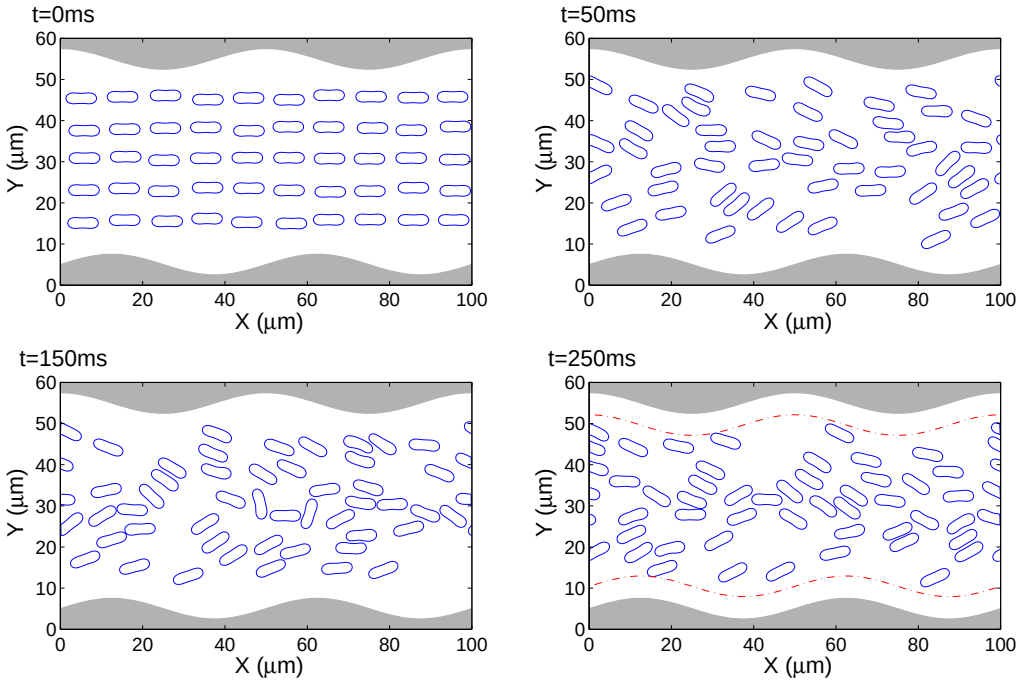

Figure 4.44: Shapes and positions of 50 cells at $t = 0$, 50, 150, and 250ms. The dash red line denotes the shift of the curve boundary function tangential to the closed cell to the wall.

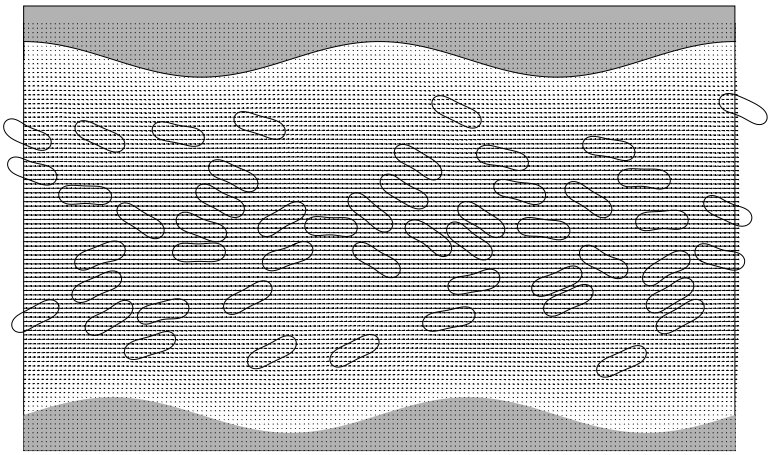

Figure 4.45: Velocity field and shapes and positions of 50 cells at $t = 250$ ms.

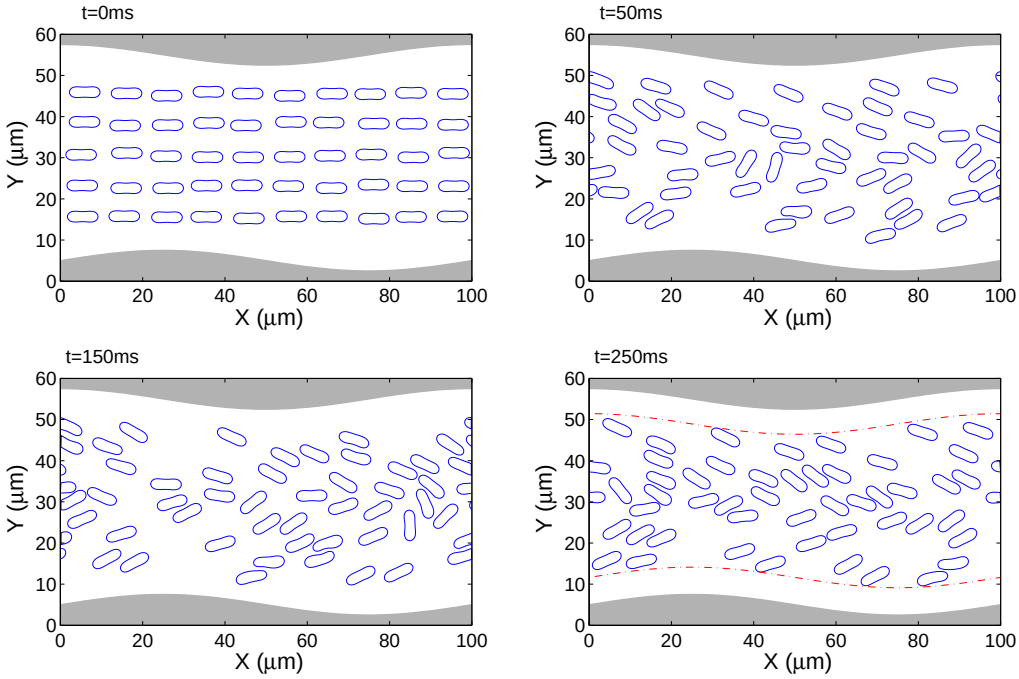

Figure 4.46: Shapes and positions of 50 cells at $t = 0$, 50, 150, and 250ms. The dash red line denotes the shift of the curve boundary function tangential to the closed cell to the wall.

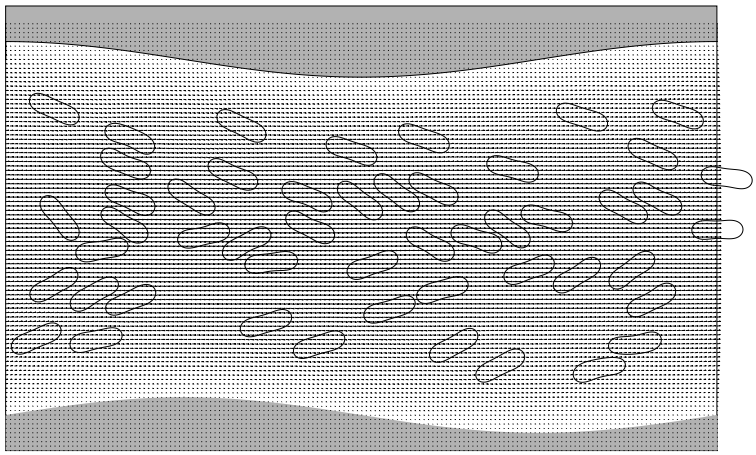

Figure 4.47: Velocity field and shapes and positions of 50 cells at $t = 250$ ms.

Reynolds number of the Poiseuille flow without cells is 0.139. The initial velocity is zero everywhere. The time step is 10^{-5} ms. Here we considered three different bending constants, which are $0.01k_b$, $0.1k_b$, and $1k_b$. The positions and shapes of cells at relative stable states are shown in Figure 4.49 and the associated average velocity profiles are exhibited in Figure 4.50. Aggregation of cells and cell-free layers next to the walls are observed in Figure 4.49. The smaller the bending constant, the less the size of the cell-free layer. As observed in *vivo* and *vitro* experiments [73], the average velocity profiles of the fluid flow with cells as shown in Figure 4.50 have blunt shapes due to the aggregation of the cells in the central region. Comparing with a fluid without cells under the same pressure gradient, the flow rate with cells Q is smaller. Hence the apparent viscosity $\eta = \mu Q_0/Q$, where Q_0 is the flow rate without cells, is larger than 1.2, implying the flow resistance increases due to the existence of the cells. From Figure 4.50, we know that the apparent viscosity η is an increasing function as the bending constant k_b. A similar tendency was reported in [96].

4.4.4 RBC rouleaux in a very narrow channel

As shear stress is reduced, RBCs can aggregate and tend to obstruct the capillary entrance. With weak aggregation, RBCs form rouleaux, which look like stacks of coins. As the end of this section, we have studied the rouleaux formation of many cells in a very narrow channel with weak aggregation. To implement this purpose, a Morse potential (2.15) is adopted to model the intercellular interaction energy. The reference distance r_0 is chosen to be 0.5 μm (the value of this parameter can be

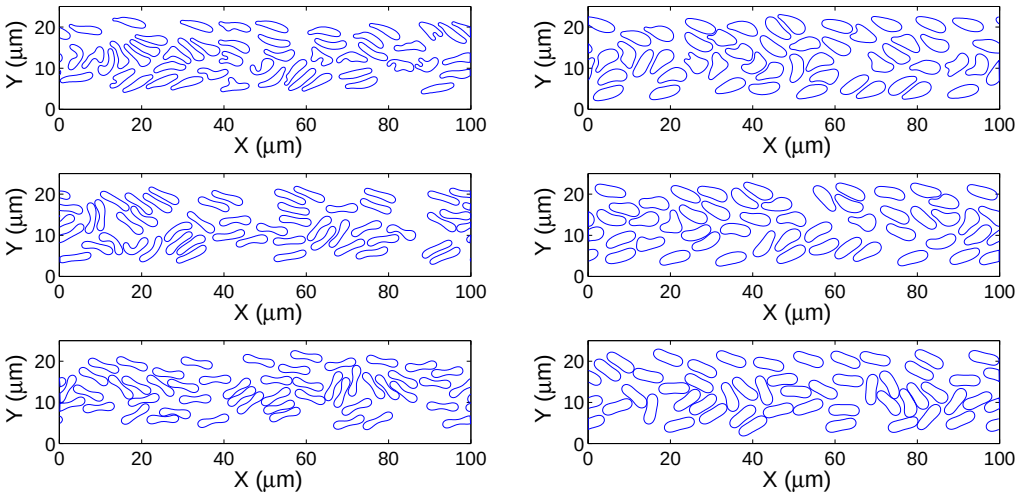

Figure 4.48: The relative stable states of the fluid flow with cells with different bending constants $0.01k_b$ (top), $0.1k_b$ (middle), and $1k_b$ (bottom) for $s^* = 0.481$ (left) and 0.7 (right).

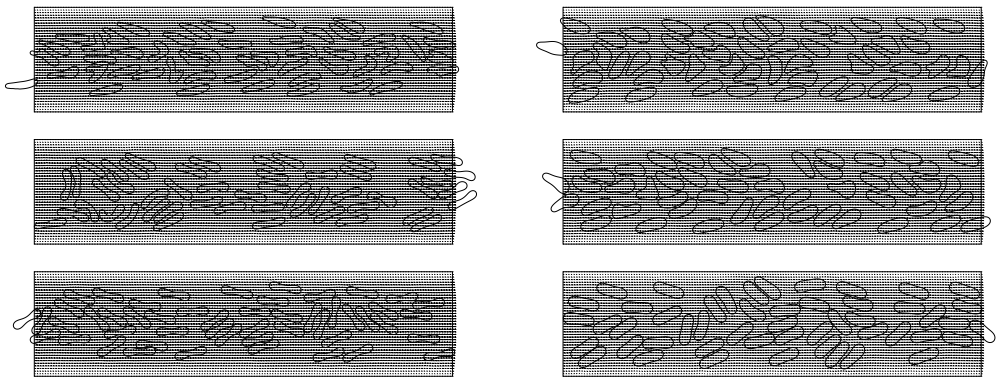

Figure 4.49: Velocity field and shapes and positions of cells with different bending constants $0.01k_b$ (top), $0.1k_b$ (middle), and $1k_b$ (bottom) for $s^* = 0.481$ (left) and 0.7 (right).

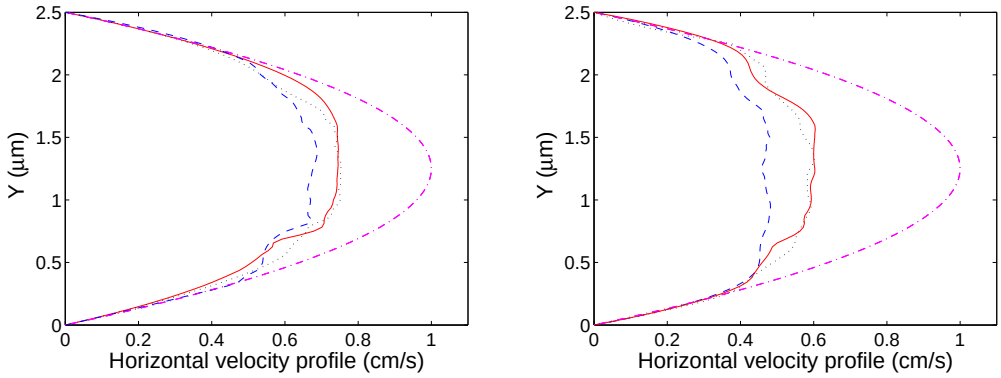

Figure 4.50: Distribution of the horizontal velocity of the fluid flow with cells at the relative stable states for different bending constants $0.01k_b$ (black dotted line), $0.1k_b$ (red solid line), and $1k_b$ (blue dashed line) for $s^* = 0.481$ (left) and 0.7 (right). The magenta dashdot line denotes the associated velocity distribution of the steady state fluid flow without cells.

reduced when a finer mesh grid is used). The value of the scaling factor is $\beta = 58.2$ μm^{-1}. The surface energy D_e can be picked to adjust a weak or strong intercellular interaction.

The computational domain is a 100×10 μm^2 rectangle. Hence the Hct = 11.85% (resp., 17.24%) for the value of $s^* = 0.481$ (resp., $s^* = 0.7$). The pressure gradient is set as a constant for this study so that the Reynolds number of the Poiseuille flow without cells is 0.083. The initial velocity is zero everywhere. The time step is 10^{-5} ms. The shapes and the position of 10 cells at relative stable status of $s^* = 0.481$ and 0.7 are shown in Figure 4.52. RBCs aggregate by attaching each other side by side (resembling stack of coins) forming rouleaux for both $s^* = 0.481$ and 0.7, which are similar to the experimental observation (see Figure 4.51). The averaged velocity and the associated Re are shown in Table 4.5.

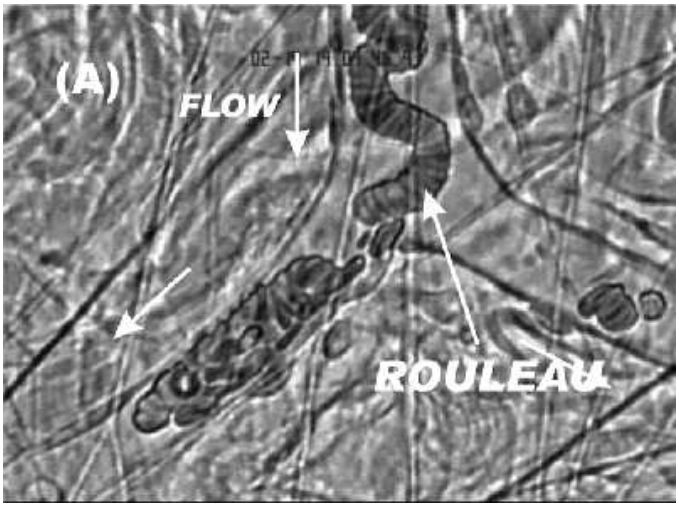

Figure 4.51: Image of RBC rouleaux formation in capillaries from [54].

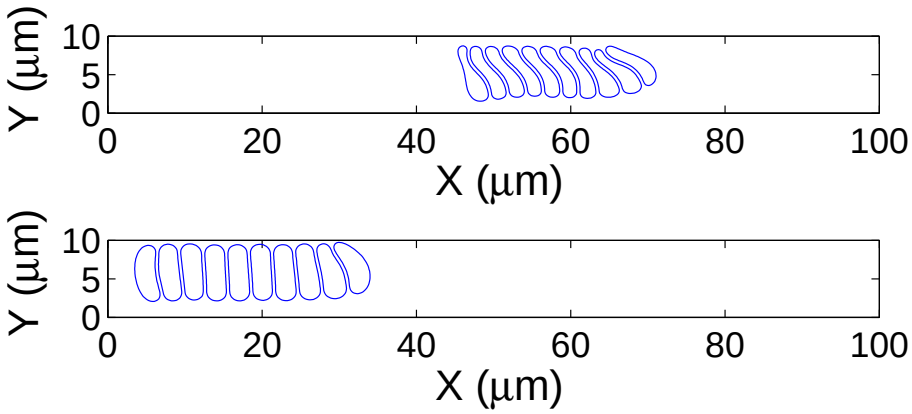

Figure 4.52: Shapes and positions of 10 cells at relative stable states of $s^* = 0.481$ (top) and 0.7 (bottom).

Hct (%)	U^*(cm/s)	U^{**}(cm/s)	Re
11.85	0.1	0.056	0.0047
17.24	0.1	0.048	0.004

Table 4.5: The hematocrit (Hct), the averaged velocity of the steady state fluid flow without cells U^*, the averaged velocity of the relative steady state fluid flow with cells U^{**}, and the Reynolds number Re based on U^{**} .

4.5 Interaction of two kinds of cells in Poiseuille flows

4.5.1 Interaction of two kinds of cells in a wide channel

In this section, we have simulated the interaction of cells of two swelling ratios, $s^* = 0.7$ and 1, in Poiseuille flow and studied the size of the cell-free layer and the Fahraeus-Lindqvist effect. The cells of $s^* = 1$ are treated as solid particles in the simulation by adjusting its bending parameter to 1000 times of the k_b given at the beginning of this Chapter. We have considered the cases of forty eight cells of $s^* = 0.7$ and two cells of $s^* = 1$ with the averaged velocity $U = 3.333$ cm/s. All other parameters are kept the same as in Section 4.1.1. The hematocrit of fifty cells is Hct = 17.536%, so the estimation of the cell-free layer is about 5.7 μm [10]. We have considered two cases which have different initial position of the circular cells. The positions and shapes of cells at different times are shown in Figures 4.53 and 4.55. The associated velocity fields and shapes and positions of the finally relative steady state are displayed in Figures 4.54 and 4.56, respectively. The averaged velocity profiles of the fluid flow with cells as shown in Figure 4.57 have blunt shapes due to the aggregation of the cells in the central region. The histories of the height of two cells of $s^* = 1$ are shown in Figure 4.58. Two cells of $s^* = 1$, which have almost circular shape, move to the region next to the walls and stay there, which is what we expect for such type of cells since the cell of $s^* = 1$ has less deformability and the lowest rate of migration toward the center line of the channel. Once they are in

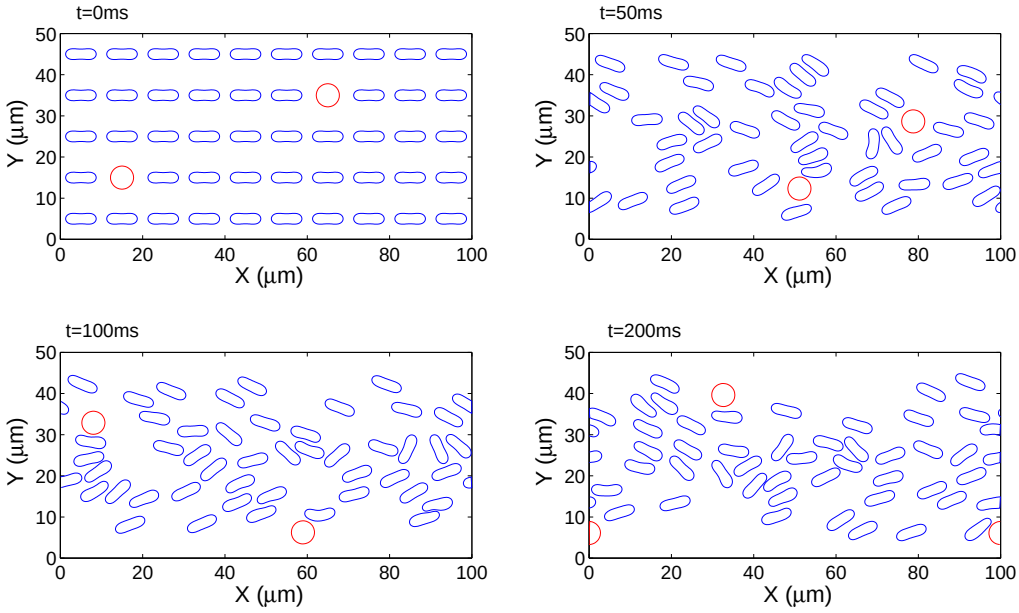

Figure 4.53: Shapes and positions of cells for the case I at $t = 0$, 50, 100, and 200 ms (from left to right and from top to bottom).

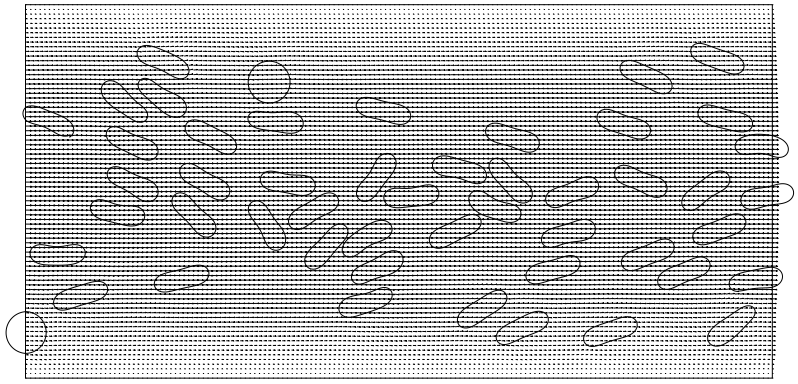

Figure 4.54: Velocity field and shapes and positions of cells for the case I at $t = 200$ ms.

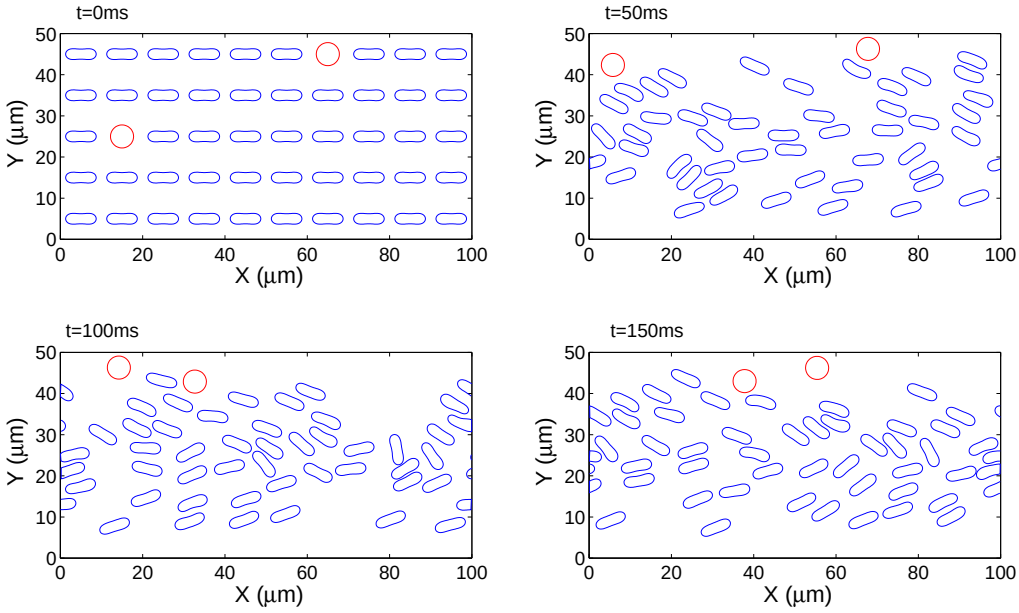

Figure 4.55: Shapes and positions of cells for the case II at $t = 0$, 50, 100, and 150 ms (from left to right and from top to bottom).

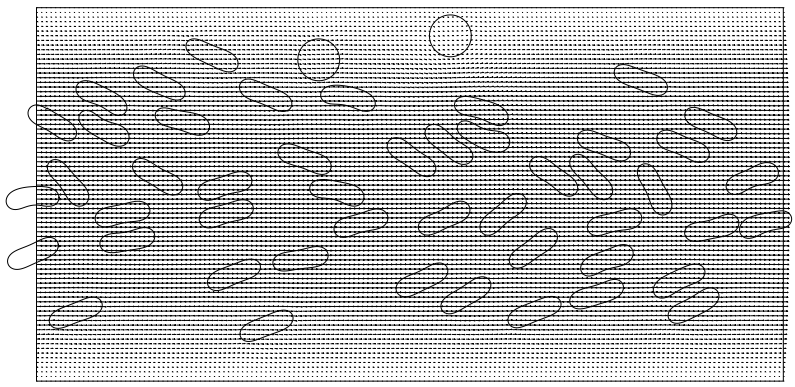

Figure 4.56: Velocity field and shapes and positions of cells for the case I at $t = 150$ ms.

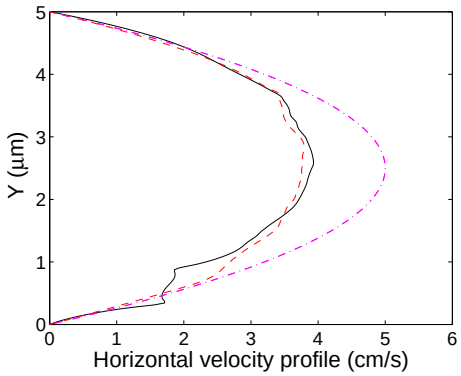

Figure 4.57: Distribution of the horizontal velocity of the fluid flow with cells at the relative stable state: case I (black solid line) and case II (red dashed line). The magenta dashdot line denotes the associated velocity distribution of the steady state fluid flow without cells.

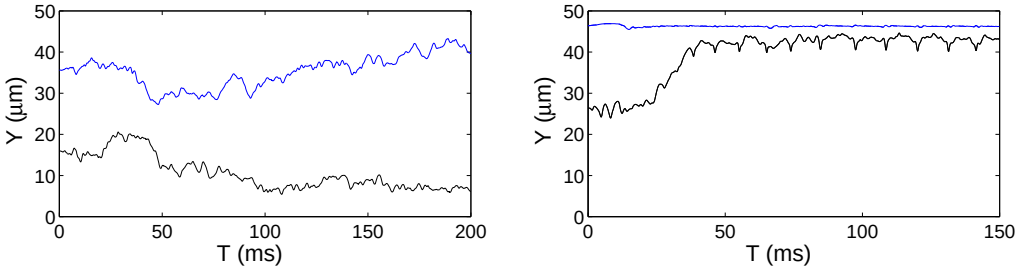

Figure 4.58: The histories of the height of two cells of $s^* = 1$: case I (left) and case II (right).

the region next to the walls, the other kind of cells keep them in the same region due to Fahraeus-Lindquis effect. Our results show the averaged sizes of cell-free layer associated to the cells of $s^* = 0.7$ are about 5.92 μm and 5.81 μm, respectively, which are in agreement with the estimation in [10]. The Reynolds numbers based the averaged velocity and the channel height are about Re = 1.11 and 1.08, respectively. For the interaction of cells of two different swelling ratios, the computational results show that the almost circular cells behave similar to the neutrally buoyant disks when interacting with other cells (see [67]).

4.5.2 Interaction of two kinds of cells in a narrow channel

In this section, we have simulated the interaction of forty five cells of swelling ratio $s^* = 0.481$ and five circular cells of radius 1.4 μm in Poiseuille flows. The computational domain is a 100×25 μm^2 rectangle. The circle cells are treated as solid particles in the simulation by adjusting its bending parameter to 1000 times of the k_b given at the beginning of this chapter. The averaged velocity of the fluid flow without the cells is 3.33 cm/s. We keep all other parameters the same as those in Section 4.1.1. The hematocrit of 50 cells is Hct = 22.56 %. The positions and shapes of cells at different times are shown in Figure 4.59. The velocity field and positions and shapes at the last moment is shown in Figure 4.60. The averaged size of cell-free layer is about 3.03 μm. Five circular cells, which have almost circular shape, move to the region next to the walls and stay there, which is what we expect for such type of cells since the cell of $s^* = 1$ has less deformability and the lowest rate of migration toward the center line of the channel. Once they are in the region next to the walls, the other cells keep them in the same region. The histories of the height of five cells of $s^* = 1$ are shown in Figure 4.64. Such simulation results imply that the small solid particle in blood flow will accumulate in the cell-free layer regions, as has been observed in experiments with platelets in [1].

When we reduced the bending constant of the five circular cells of radius 1.4 μm back to $1k_b$ and keep all other parameters the same as those above. The circular cells also move to the region close to the wall and stay there. But it takes much time to reach the relative steady state (see Figure 4.64). The positions and shapes of cells at different times are shown in Figure 4.61. The velocity field and positions and shapes

at the last moment is shown in Figure 4.62. The averaged size of cell-free layer is about 3.03 μm. The histories of the height of two cells of $s^* = 1$ are shown in Figure 4.64. The distribution of the horizontal velocity of the fluid flow with cells at the relative stable states for both $1000k_b$ and $1k_b$ as shown in Figure 4.63. The averaged velocities of the relative steady state fluid flow with the cells are about 2.45 cm/s for $1000k_b$ and 2.38 cm/s for $1k_b$, respectively.

For this narrow channel, we also have studied the relation between the size of the cell-free layer and Hct (see Figure 4.65), and found that the averaged size of the cell-free layer ε is satisfactory:

$$\varepsilon \approx \frac{200}{3\mathrm{Hct}}. \tag{4.1}$$

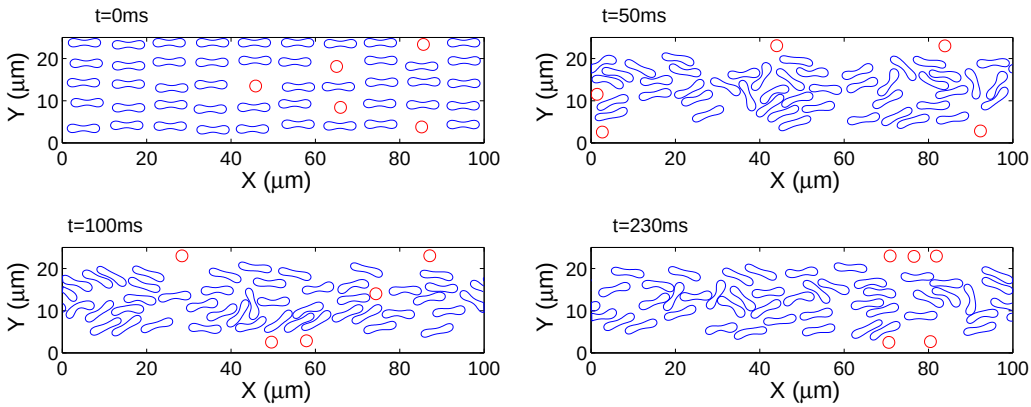

Figure 4.59: Shapes and positions of cells at $t = 0$, 50, 100, and 230 ms (from left to right and from top to bottom).

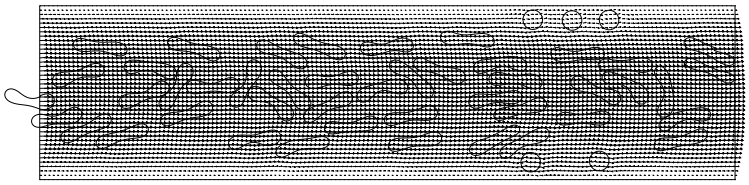

Figure 4.60: The velocity field and shapes and positions of cells at $t = 230$ ms.

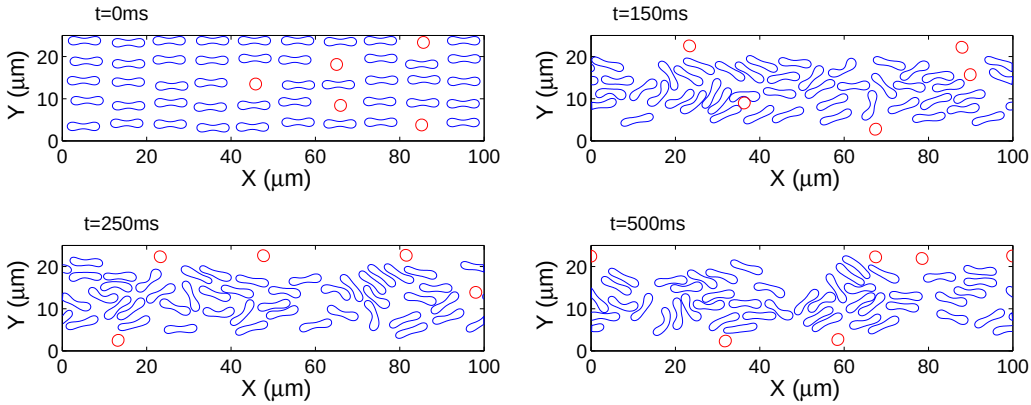

Figure 4.61: Shapes and positions of cells at $t = 0$, 150, 250, and 500 ms (from left to right and from top to bottom).

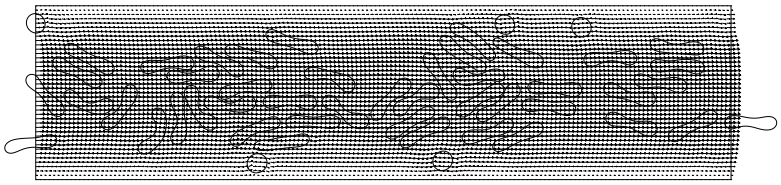

Figure 4.62: The velocity field and shapes and positions of cells at $t = 500$ ms.

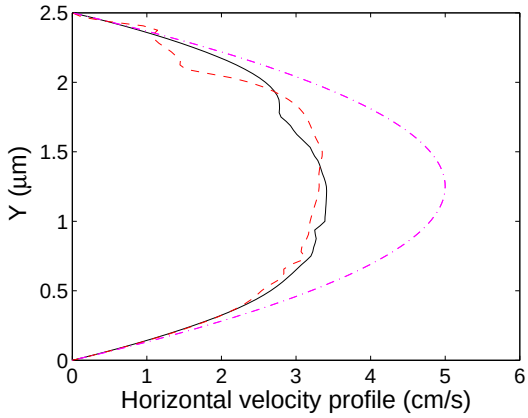

Figure 4.63: Distribution of the horizontal velocity of the fluid flow with cells at the relative stable state for $1000k_b$ (black solid line) and $1k_b$ (red dashed line). The magenta dashdot line denotes the associated velocity distribution of the steady state fluid flow without cells.

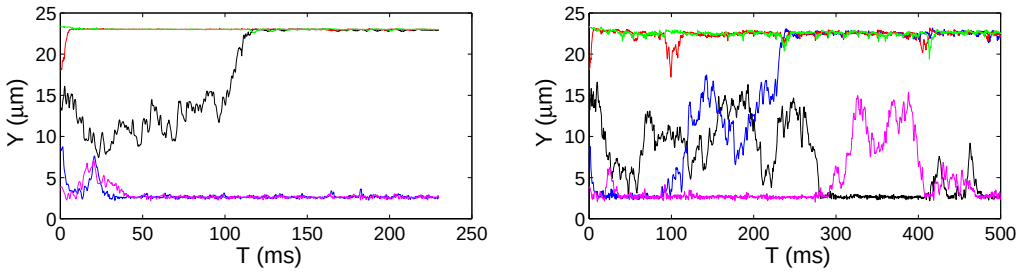

Figure 4.64: The histories of the height of five cells of radius 1.4 μm for $1000k_b$ (left) and $1k_b$ (right).

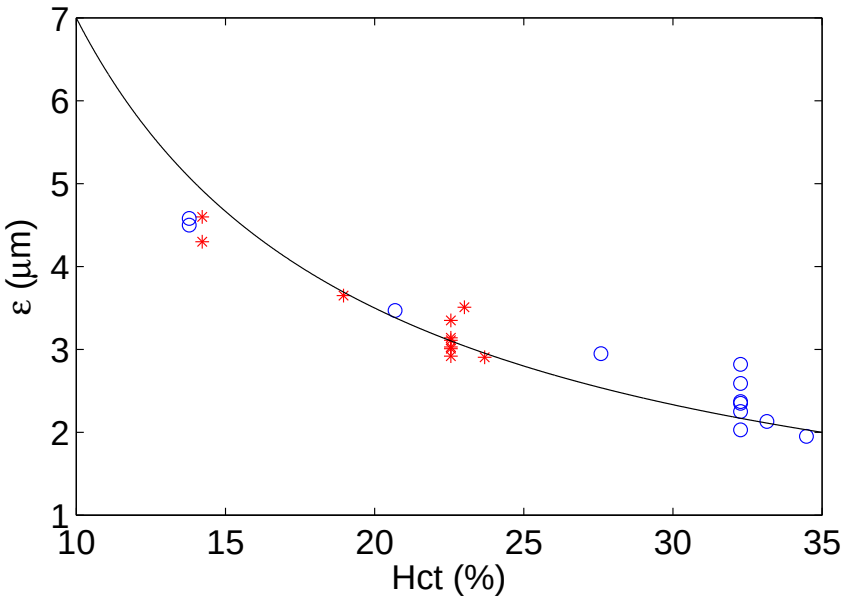

Figure 4.65: The size of cell-free layer as a function of Hct.

Chapter 5

RBC in three dimensional flows

Like in the two-dimensional case, an elastic spring network model is chosen to model the skeleton structure of RBC membrane. Such model combined with an immersed boundary method and finite element method is applied to simulate the RBC rheology in three-dimensional microchannels.

5.1 Model and method

The governing equations for the fluid-cell system are the Navier-Stokes equations

$$\rho\left(\frac{\partial \mathbf{u}}{\partial t} + \mathbf{u}\cdot\nabla\mathbf{u}\right) = -\nabla p + \mu\Delta\mathbf{u} + \mathbf{f} \text{ in } \Omega\times(0,T), \tag{5.1}$$

$$\nabla\cdot\mathbf{u} = 0 \text{ in } \Omega\times(0,T). \tag{5.2}$$

Here the domain Ω is a bounded region filled with blood plasma which is incompressible, Newtonian, and contains RBC(s) (see Figure 5.1).

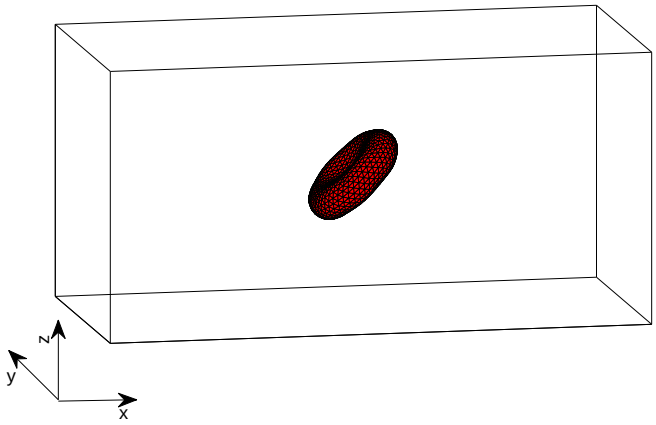

Figure 5.1: An example of computational domain with one RBC.

Equations (5.1) and (5.2) are completed by the following boundary and initial conditions:

$$\mathbf{u} = \mathbf{g} \text{ on the top and bottom of } \Omega \text{ and}$$

$$\mathbf{u} \text{ is periodic in } x \text{ direction,} \tag{5.3}$$

$$\mathbf{u}(\mathbf{x}, 0) = \mathbf{u}_0(\mathbf{x}) \text{ in } \Omega. \tag{5.4}$$

where $\mathbf{u}$ and p are the fluid velocity and pressure, respectively, anywhere in the flow, ρ is the fluid density, and μ is the fluid viscosity. $\mathbf{f}$ is a body force which is the sum of $\mathbf{f}_p$ and $\mathbf{f}_B$, where $\mathbf{f}_p$ is the pressure gradient pointing in the horizontal direction and $\mathbf{f}_B$ accounts for the force acting on the fluid-cell interface. In equation (5.4), $\mathbf{u}_0(\mathbf{x})$ is the initial fluid velocity. For the cases of shear flow, $\mathbf{f}_p$ is set to be zero. When considering the slit Poiseuille flow, we set $\mathbf{g} = \mathbf{0}$. For both shear flow and slit

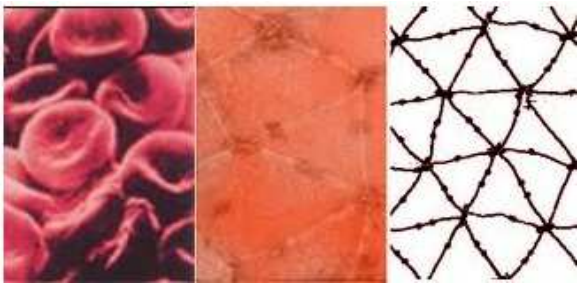

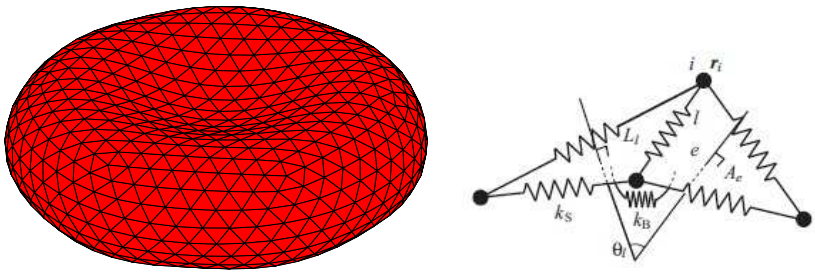

Figure 5.2: Image of RBCs and the spectrin cytoskeleton from [87] (top). The elastic spring model of the three-dimensional RBC membrane: The membrane is divided into small triangular elements (bottom left) and the associated spring parameters between two neighboring triangular elements (bottom right).

Poiseuille flow, $\mathbf{u}$ is periodic in both x and y directions.

5.1.1 Elastic spring model for the RBC membrane

The deformability and the elasticity of the RBC are due to the skeleton architecture of the membrane. A three-dimensional elastic spring network developed in [91] is chosen here to model the deformable behavior of the RBCs. Based on this model, the RBC membrane can be viewed as small triangular elements and the neighboring vertices of these elements are connected by springs, as shown in Figure 5.2. Energy

stores in the spring due to the change of the length L_l of the spring with respect to its reference length L_{l0} , the change in angle θ between two neighboring springs, the local areal conversation , and the global areal conversation with respect to its reference area A_0. The total energy of the RBC membrane, $E = E_s + E_b + E_a + E_A$, is the sum of the total energy for stretch and compression, the total energy for the bending, the total local areal conversation, and the total global areal conversation which, in particular, are

$$E_s = \frac{k_s}{2} \sum_{l=1}^{N_l} (L_l - L_{l0})^2, \tag{5.5}$$

$$E_b = \frac{k_b}{2} \sum_{l=1}^{N_l} L_l \tan^2(\frac{\theta_l}{2}), \tag{5.6}$$

$$E_a = \frac{k_a}{2} \sum_{e=1}^{N_e} (\frac{A_e - A_{e0}}{A_{e0}})^2 A_{e0}, \tag{5.7}$$

and

$$E_A = \frac{k_A}{2} (\frac{A - A_0}{A_0})^2 A_0. \tag{5.8}$$

In equations (5.5)−(5.8), N_l is the total number of the springs, k_s and k_b are spring constants for changes in length and bending angle, respectively, θ_l is the angle between the normal outer vectors of the two neighboring triangular elements which have the side l as their boundary, A_e is the area of triangular element e, A_{e0} is the reference area of e, N_e is the total number of the triangular elements, k_a is the the area expansion modulus for the local triangular element, A is the area of the entire membrane, A_0 is the reference global area and k_A is the global area expansion modulus.

In the process of creating the initial biconcave shape of RBCs described in [91], the RBC is assumed to be a sphere of radius $R_0 = (\frac{S}{4\pi})^2$ (here $S = 135\ \mu\text{m}^2$) initially. The sphere is discretized into N_e triangular elements with N nodes so that N_l springs are formed by connecting the neighboring vertices of these elements. The shape change is stimulated by reducing the total volume of the sphere through a penalty function

$$\Gamma_V = \frac{k_V}{2}(\frac{V - V_e}{V_e})^2 V_e, \tag{5.9}$$

where V and V_e are the time dependent volume of the RBC and the equilibrium volume of the RBC, respectively, and k_V is the penalty coefficient. Thus the total energy is modified as $E + \Gamma_V$. Based on the principle of virtual work the force acting on the ith membrane node now is

$$\mathbf{F}_i = -\frac{\partial(E + \Gamma_V)}{\partial \mathbf{r}_i}, \tag{5.10}$$

where $\mathbf{r}_i$ is the position of the ith membrane node. When the volume is reduced, each RBC membrane node moves on the basis of the following equation of motion:

$$m\ddot{\mathbf{r}}_i + \gamma\dot{\mathbf{r}}_i = \mathbf{F}_i. \tag{5.11}$$

Here, $\dot{(\ )}$ denotes the time derivative, and m and γ represent the membrane node mass and the membrane viscosity of the RBC. The position $\mathbf{r}_i$ of the ith membrane node is solved by discretizing equation (5.11) via a second order finite difference method. Figure 5.3 shows an example of a sequence of the shapes when reducing the volume of a sphere with surface area $S = 135\ \mu\text{m}^2$ to 63.7% (i.e. $V = 94\ \mu\text{m}^3$) of its initial volume to form the biconcave RBC shape with $N = 770, N_e = 1536$, and

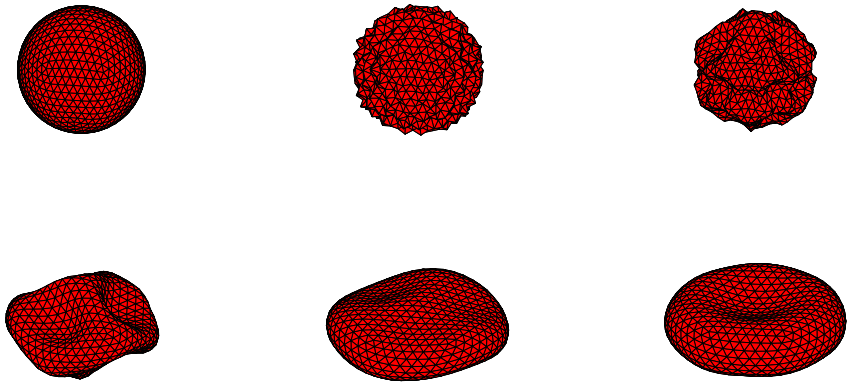

Figure 5.3: Snapshots of changing a sphere with surface area $S = 135\ \mu\text{m}^2$ to 63.7% (i.e. $V = 94\ \mu\text{m}^3$) of its initial volume to form the biconcave RBC shape (N = 770) at different time: 0, 1, 12, 200, 835, and 15000 ms (from left to right and from top to bottom).

$N_l = 2304$. The total energy stored in the membrane decreases as the time elapses as shown in Figure 5.4. The final shape of the RBC is obtained as the total energy is minimized. The volume of the final shape has less than 0.001% difference from the given equilibrium area V_e and the global area of the final shape has less than 0.002% difference from the reference area A_0 of the initial sphere. The value of the swelling ratio of a RBC in this work is defined by $V^* = \frac{3V}{4\pi R_0^3}$.

5.1.2 Immersed boundary method

The immersed boundary method developed by Peskin, e.g., [69, 70, 71], is employed in our study because of its distinguishing features in dealing with the problem

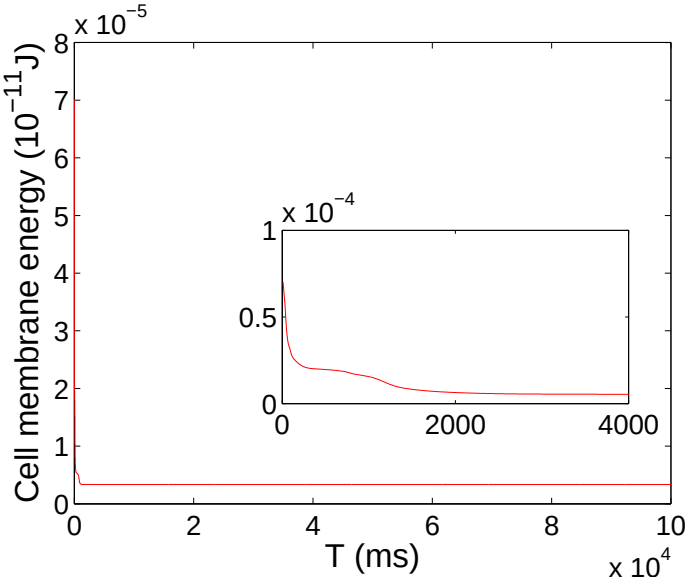

Figure 5.4: The history of the total energy of RBC membrane.

of fluid flow interacting with a flexible fluid-structure interface. Based on the method, the boundary of the deformable structure is discretized spatially into a set of boundary nodes. The force located at the immersed boundary node $\mathbf{X} = (X_1, X_2, X_3)$ affects the nearby fluid mesh nodes $\mathbf{x} = (x_1, x_2, x_3)$ through a three-dimensional discrete δ function $D_h(\mathbf{X} - \mathbf{x})$:

$$\mathbf{f}_B(\mathbf{x}) = \sum \mathbf{F}_i D_h(\mathbf{X}_i - \mathbf{x}) \quad \text{for } |\mathbf{X_i} - \mathbf{x}| \leq 2h, \tag{5.12}$$

where h is the uniform finite element mesh size and

$$D_h(\mathbf{X} - \mathbf{x}) = \delta_h(X_1 - x_1)\delta_h(X_2 - x_2)\delta_h(X_3 - x_3) \tag{5.13}$$

with the one-dimensional discrete δ functions being

$$\delta_h(z) = \begin{cases} \frac{1}{8h}\left[3 - 2|z|/h + \sqrt{1 + 4|z|/h - 4(|z|/h)^2}\right], & |z| \le h, \\ \frac{1}{8h}\left[5 - 2|z|/h - \sqrt{-7 + 12|z|/h - 4(|z|/h)^2}\right], & h \le |z| \le 2h, \\ 0, & \text{otherwise.} \end{cases} \tag{5.14}$$

The movement of the immersed boundary node $\mathbf{X}$ is also affected by the surrounding fluid and therefore is enforced by summing the velocities at the nearby fluid mesh nodes $\mathbf{x}$ weighted by the same discrete δ function:

$$\mathbf{U}(\mathbf{X}) = \sum h^3 \mathbf{u}(\mathbf{x_j}) D_h(\mathbf{X} - \mathbf{x_j}) \quad \text{for } |\mathbf{X} - \mathbf{x_j}| \le 2h. \tag{5.15}$$

After each time step, the position of the immersed boundary node is updated by

$$\mathbf{X}_{t+\Delta t} = \mathbf{X}_t + \Delta t \mathbf{U}(\mathbf{X}_t). \tag{5.16}$$

Remark 5.1. Similar to the two-dimensional cases, at each time step, via operator splitting technique, we solve a sequence of subproblems, namely, a degenerated quasi-Stokes problem, the membrane motion, the advection problem, and the diffusion problem as in [81, 82]. We keep the conversation of volume given in equation (5.9) when computing membrane force in equation (5.10) since the divergence-free condition is enforced in a weak sense through the finite element method used in the computations.

5.2 Simulation results and discussions

5.2.1 Stretching force test

A very important advantage of the coarse-grained model discussed in [72] is that it allows us to use a smaller number of nodes to represent the RBC membrane and then speed up the computations, especially for the cases of the flow with thousands of deformable RBCs. But the average equilibrium length of the springs depending on the number of nodes will be larger than the observed data in experiment. Thus it is necessary to do stretching force test on RBC membrane to tune the elastic parameters such that the spring network model with less nodes can still be used to simulate the RBC membrane as well as possible.

When performing the cell stretching force test, RBC ($N = 194$) is suspended in the fluid flow with computational domain $2H \times H \times 2H$ μm^3 (here $H = 5R_0$) as shown in Figure 5.5. The initial position of RBC is located in the center of the domain with its large diameters placed in the xy-plane. We choose 5% of vertices that have the largest x coordinates. In our present simulations, we apply the time-dependent force $\mathbf{f}_n^{\text{ext}} = \mathbf{f}^{\text{ext}}/(0.05N)$ to each of these points. Correspondingly, a force $\mathbf{f}_n^{\text{ext}} = -\mathbf{f}^{\text{ext}}/(0.05N)$ is applied to each of those vertices with the smallest x coordinates at the beginning of the simulation. The transverse and axial diameters are computed as $2 \times \max_{n=1,2,\cdots,N} \sqrt{{y_n}^2 + {z_n}^2}$ and $|\max_{n=1,2,\cdots,N} x_n - \min_{n=1,2,\cdots,N} x_n|$, respectively. Figure 5.6 shows our simulation results are in good agreement with experimental data in [57]. In Figure 5.6, the simulations are carried out with two groups of parameters as shown in Table 5.1. The RBC shapes with parameters (II) at different stretching forces are

Parameter	Group I	Group II
k_s (N/m)	5.5×10^{-6}	7.5×10^{-6}
k_b (N)	5.0×10^{-12}	7.0×10^{-12}
k_A (N/m)	5.0×10^{-3}	5.0×10^{-3}
k_a (N/m)	0.01	0.01
k_V (N/m^2)	50	50

Table 5.1: Two groups of the cell membrane parameters.

shown in Figure 5.7.

5.2.2 A single RBC in a narrow tube

First, we apply the coarse-grained model ($N = 194$) to simulate deformation and motion of a single RBC in a horizontal tube with 10 μm in diameter and 50 μm in length. The periodic condition is imposed in the horizontal x direction. The velocity of the fluid flow is zero everywhere initially. Then we apply a body force to drive the tube flow such that the maximun velocity of the fluid flow is 0.5 cm/s. The RBC deforms and a typical parachute shape is obtained, which is commonly observed in experiments [88]. The RBC can restore to the biconcave resting disk after the removal of the force as in [29, 72]. The snapshots at different time and the associated history of the energy stored in the RBC membrane are shown in Figures 5.8 and 5.9, respectively. The total cell membrane energy increases when the cell shape changes from a biconcave shape to a parachute shape under the flow and the total energy reaches a plateau when a parachute shape as its equilibrium shape is obtained, and the total energy decreases back to the minimum as the cell quickly returns back to its initial biconcave shape after cessation of the flow at $t = 732$ ms..

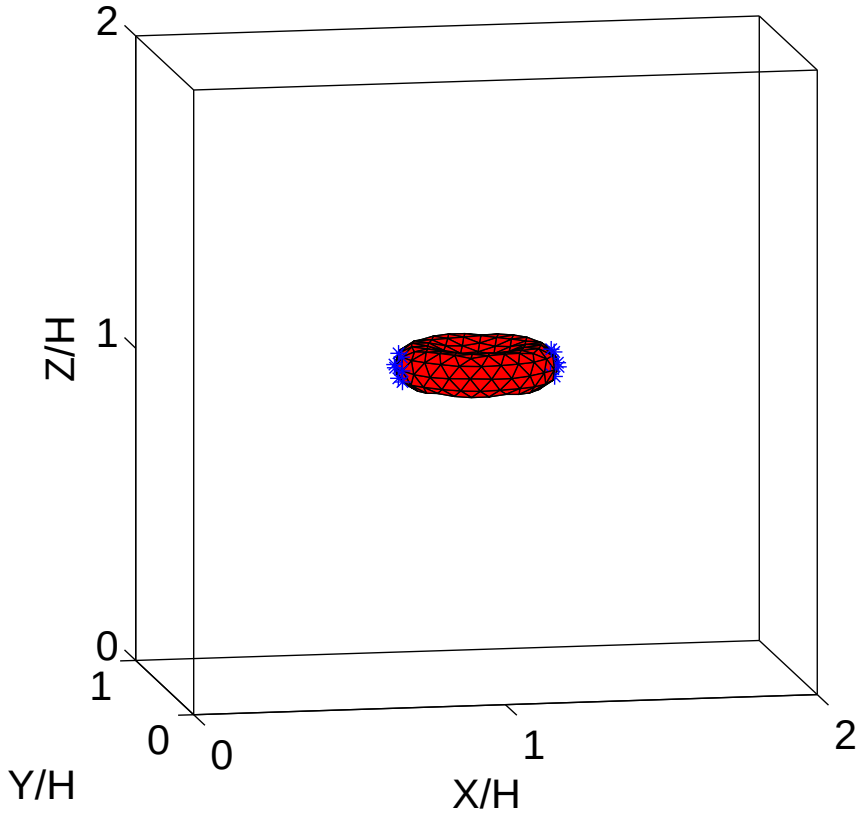

Figure 5.5: The initial state of RBC (N = 194) at the beginning of the stretching force test. The blue asterisks denote the vertices the stretching force applied.

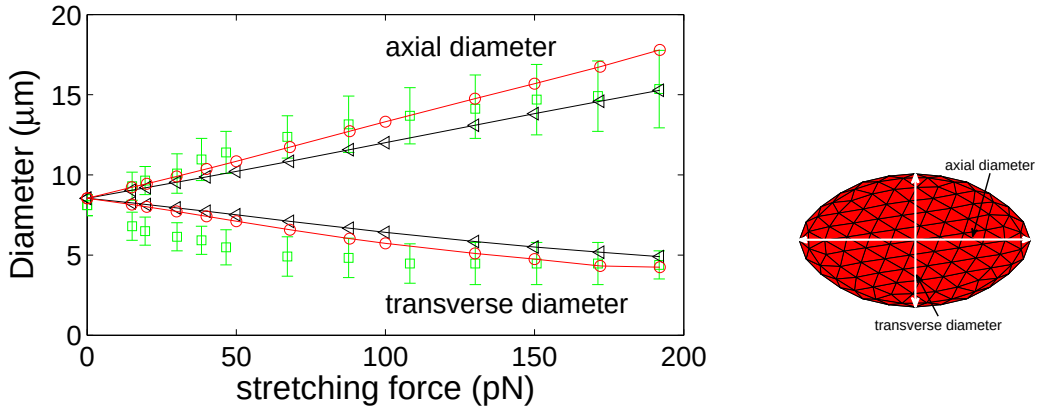

Figure 5.6: Axis and transverse diameters of the RBC versus stretching force. The symbols represent the optical tweezers experimental data from [57]. Red line with circle and black line with triangular denote the parameters (I) and (II), respectively.

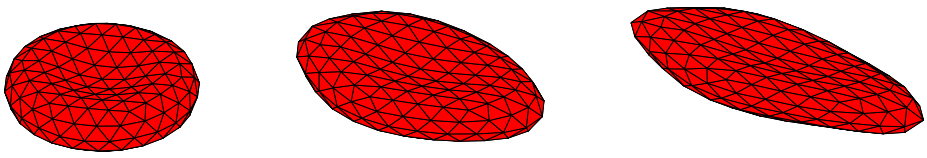

Figure 5.7: RBC shapes with parameter (II) at different forces 0, 88, and 172 pN (from left to right).

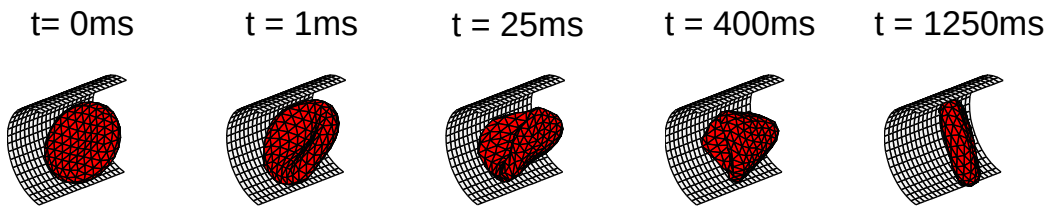

Figure 5.8: The snapshots of the cell deformation at different time. From left to right: (a) The biconcave disk RBC is placed in the narrow tube with the fluid at rest. (b) and (c) The deformation of RBC after the body force driving the fluid is applied 1 and 5 ms, respectively. (d) The parachute shape of RBC at steady flow. (e) The RBC returns to its equilibrium biconcave shape after the removal of the body force driving the fluid flow.

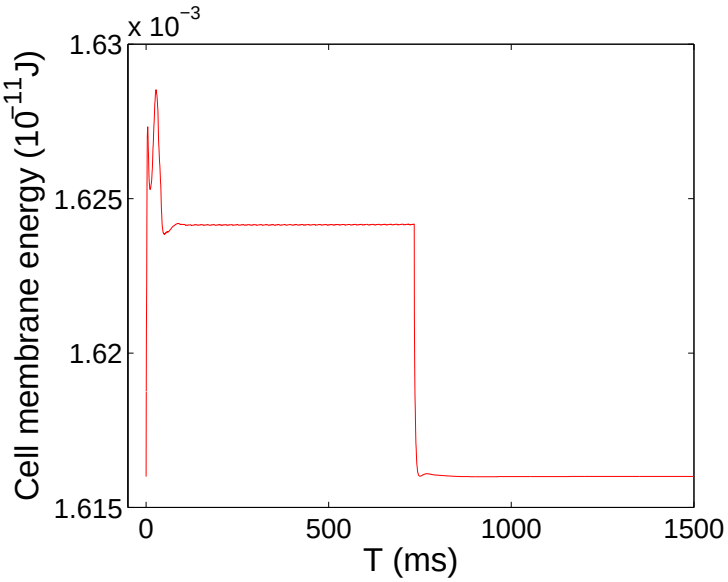

Figure 5.9: The history of the energy stored in the RBC membrane. The body force is removed at $t = 732$ ms.

5.2.3 Lateral migration of a single RBC in a slit Poiseuille flow

In this section, we have investigated the lateral migration and shape and position of a single RBC in a slit Poiseuille flow. The computational domain is $2H \times 2H \times H$ μm^3 (here $H = 5R_0$). Here, x is the direction of the flow, z is the direction of velocity gradient, and y is the direction of vorticity of the undisturbed flow. The periodic conditions are imposed in the x direction and y direction. The initial velocity of the flow is zero everywhere. The initial position of RBC is $(H, H, 0.825H)$ with the initial angle $\varphi = 0$. Six different constants for pressure gradient are set for this study so that the Reynolds numbers of the Poiseuille flow without the cell are about 0.0137, 0.03, 0.06, 0.12, 0.164, and 0.205. The Reynolds number is defined by Re $= \rho H U_{\max}/\mu$. The combined effect of the deformability, the degree of confinement, and the shear gradient of the Poiseuille flow make the RBC migrate toward a certain cross-sectional equilibrium position, which lies close to the center line (here it settles between $0.5H$ and $0.6H$). The beginning velocity of the migration toward the center line of the channel is an increasing function of Re. The histories of the cell mass center at different Re are shown in Figure 5.10 and the corresponding equilibrium shapes and the associated left side view, front view, and the top view for Re = 0.12 are displayed in Figures 5.11 and 5.12, respectively. From Figures 5.10 and 5.11, we know that the equilibrium position and shape depends on the Reynolds number Re for the same group of cell parameters. The cell rotates accompanied with less deformability for the lowest Re = 0.0137. For Re = 0.03, 0.06, 0.12, 0.164, and 0.205, a slipper shape is obtained for both two groups of cell parameters. The change in

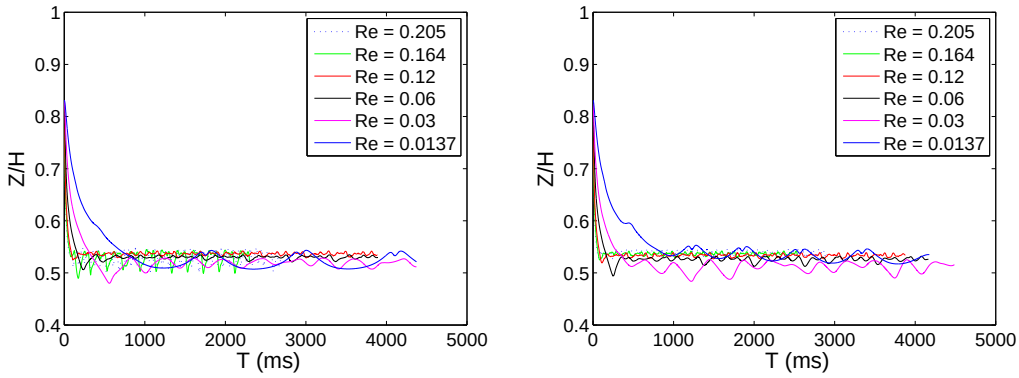

Figure 5.10: The histories of the cell mass center at different Re: parameter (I) (left) and parameter (II) (right).

the morphology is directly proportional to Re for the same group of cell parameters. For the same Re, the change in the morphology of parameter I is bigger than that of parameter II. The mass center of the equilibrium shape cell deviates away from the center line of the channel due to its asymmetric slipper shape.

5.3 Conclusions

In this chapter, an elastic spring network model combined with an immersed boundary method and finite element is used to study the RBC rheology in three-dimensional microchannels. A stretching force test has been performed to tune the RBC membrane parameters by comparing our simulation results with the optical tweezers experimental data from [57]. A coarse-grained model is adopted to investigate the motion of a single RBC in a narrow tube Poiseuille flow. In a narrow tube Poiseuille flow, a typical parachute shape is obtained as its equilibrium shape when

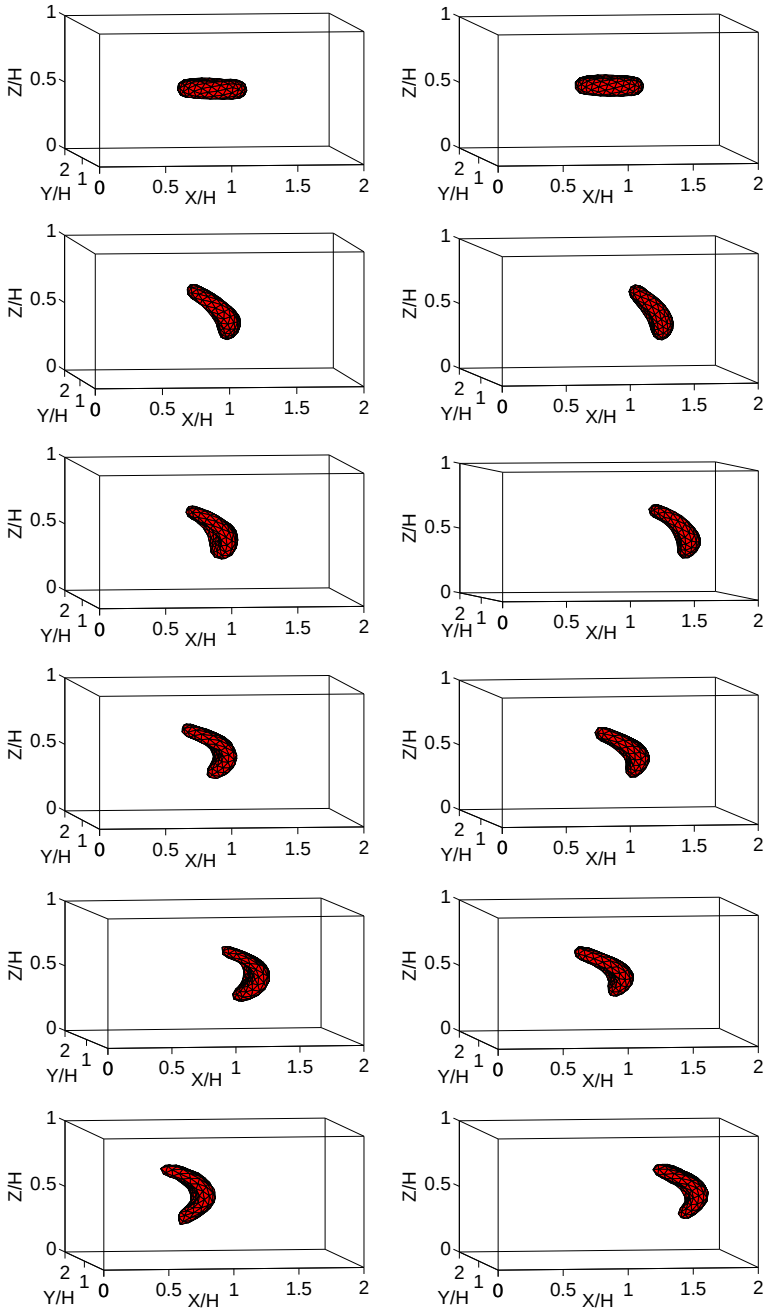

Figure 5.11: The equilibrium shapes of the cell at different Re: 0.0137, 0.03, 0.06, 0.12, 0.164, and 0.205 (from top to bottom). Parameter (I) (left) and parameter (II) (right), respectively.

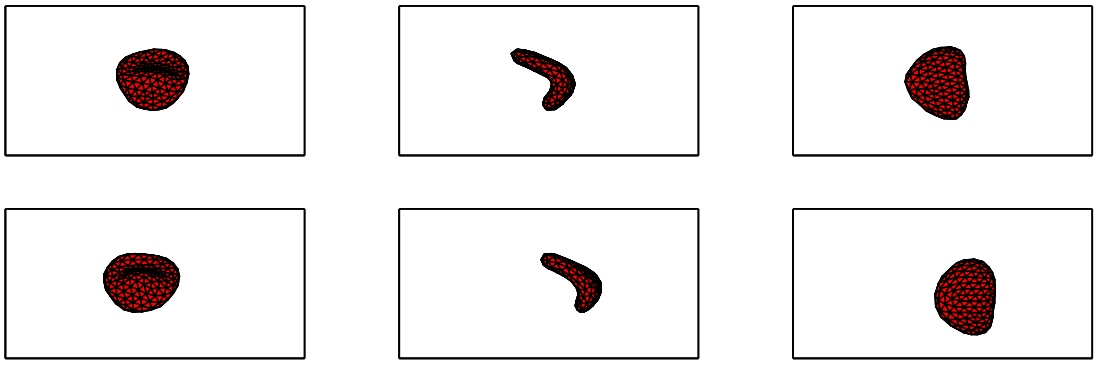

Figure 5.12: The left view (left two), the front view (middle two), and the top view (right two) with Re = 0.12 for parameter (I) (top) and parameter (II) (bottom), respectively.

the fluid is driven by a body force, and it can return to the biconcave resting disk after the removal of the force. Also the lateral migration and shape and position of a single RBC in slit Poiseuille flow has been studied. The cell rotates accompanied with less deformability for the lowest Re = 0.0137. For Re = 0.03, 0.06, 0.12, 0.164, and 0.205, a slipper shape is obtained for both two groups of cell parameters. The change in the morphology is directly proportional to Re for the same group of cell parameters. For the same Re, the change in the morphology of parameter I is bigger than that of parameter II. The mass center of the equilibrium shape cell deviates away from the center line of the channel due to its asymmetric slipper shape.

Chapter 6

Summary

6.1 Conclusions

An elastic spring model combined with an immersed boundary method and finite element method is validated in this dissertation by the comparison of the steady inclination angles of the tank treading of a single RBC in a shear flow. The effect of the viscosity ratio λ and the degree of confinement R_0/w on the dynamical behavior of RBC in shear flow are also studied. In the tank-treading regime, the inclination angle θ is a decreasing function of the viscosity ratio λ for the same swelling ratio s^* , but for the same λ, θ increases as s^* increases. A transition from tank-treading motion to tumbling motion happens as λ reaches a critical value λ_c for a given s^* and λ_c increases as s^* increases. For $\lambda = 1$, the inclination angle θ is a decreasing function of R_0/w, but for $\lambda = 5$, θ increases as the increasing value of R_0/w and reaches a peak, then decreases as R_0/w increases.

Lateral migration and equilibrium shape and position of a single RBC in two dimensional bounded Poiseuille flows are investigated by varying the initial position, the initial angle of the long axis of the cell at the center line, the swelling ratio, the membrane bending stiffness of the RBC, the maximum velocity of the flow, and the degree of confinement. The combined effects of the deformability, the degree of confinement and the shear gradient of the Poiseuille flow make the RBC migrate toward a certain cross-sectional equilibrium position, which lies either on the center line of the channel or off the center line. For $s^* > 0.8$, the speed of the migration at the beginning decreases with increasing s^*. But for $s^* < 0.8$, the speed of the migration at the beginning is an increasing function of s^*. The distance Y_d between the cell mass center of the equilibrium position and the center line of the channel increases with increasing Re and reaches a peak, then decreases with increasing Re. The peak of Re is a decreasing function of the swelling ratio ($s^* < 1.0$). The distance Y_d is almost zero for $s^* = 1.0$. Given a swelling ratio s^*, the cell membrane energy of the equilibrium position is an increasing function as Re increases. The slipper-shape cell is more stable than the parachute-shape one since the energy stored in the former is lower than that in the latter. For a given Re, the bigger the swelling ratio ($s^* < 1.0$), the lower the cell membrane energy. The deformability of cell is harder for the bigger swelling ratio because the excess perimeter is less. Two motions of oscillation and vacillating breathing of the RBC are observed in narrow and wide channels. The strength of the vacillating-breathing motion depends on the degree of confinement and the value of $u_{\max}$. The RBC exhibits a strong vacillating-breathing motion as the degree of confinement is larger or the value of $u_{\max}$ is higher. For the same degree

of confinement, the vacillating-breathing motion appears to be relatively weak but persists longer as the value of $u_{\max}$ is lower. For the different bending constants, the RBC obtains the same equilibrium shape for the same capillary number. The continuation of shape change from the slipper to the parachute by varying the value of $u_{\max}$ is obtained for the biconcave shape cell in a narrower channel. In particular, parachute shape and bullet-like shape, depending on the initial angle φ, coexist for the elliptic shape cell with lower $u_{\max}$ in a narrower channel.

Interactions of many cells in Poiseuille flows are examed for studying the size of the cell-free layer and the Fahraeus-Lindqvist effect. For the cases of many cells in a wider channel, our results show that the channel boundary (straight or curve) has no effect on the size of the cell-free layer, which is in good agreement with the estimation based on the experimental results in [10] for the different values of Hct and the averaged velocity. Also the circular cells with radius 2.8 μm like to move the region next to the wall which is similar to the behavior of white blood cells in microvessels. For the interaction of cells of two different swelling ratios, the computational results show that the almost circular cells behave similar to the neutrally buoyant disks when interacting with other cells (see [67]). For the narrower channel with height 25 μm, we have found an approximated law for the estimation of the size of the cell-free layer for the different values of Hct and the averaged velocity. Rouleaux, red blood cells stack like coins, are observed in a very narrower channel considered here when the force obtained from Morse potential function is adapted.

Finally, a stretching force test for three-dimensional RBC membrane is performed to tune the elastic parameters based on the comparison with the optical tweezers

experimental data and a coarse-grained model is adopted to study the motion and deformability of a single RBC in three-dimensional microvessels. In a narrow tube Poiseuille flow, a typical parachute shape is obtained as its equilibrium shape when the fluid is driven by a body force, and it can restore to the biconcave resting disk after the removal of the force. Also the lateral migration and equilibrium shape and position of a single RBC in slit Poiseuille flow are studied. For the same cell parameters, the equilibrium shape depends on Re, whereas for the same Re, the change in the morphology depends on the membrane bending constant. The cell sets its equilibrium position between $0.5H$ and $0.6H$. The mass center of the equilibrium shape cell deviates away from the center line of the channel due to its asymmetric slipper shape.

6.2 Future work

Future work would be on the dynamics of a single RBC and many RBCs in three-dimensional blood fluid flow and the interaction of RBCs and particles in three-dimensional blood fluid flow. It is expected that the mathematical modeling and computational simulations can help understand more about the blood flow in microcirculation and facilitate the drug delivery study.

Bibliography

[1] Aarts P., van der Broek S., Prins G., Kuiken G., Sixma J., Heethaar R., Blood platelets are concentrated near the wall and red blood cells, in the center in flowing blood, *Arteriosclerosis*, **6**, 1988, 819-824.

[2] Adachi K., Kiriyama S., and Yoshioka N., The behavior of a swarm of particles moving in a viscous fluid, *Chemical Engineering Science* , **33**, 1978, 115-121.

[3] Adams J., Swarztrauber P., Sweet R., FISHPAK: A package of Fortran subprograms for the solution of separable elliptic partial differential equations, The National Center for Atmospheric Research, Boulder, CO, 1980.

[4] Alexeev A., Verberg R., Balazs A.C., Modeling the interactions between deformable capsules rolling on a compliant surface, *Soft Matter*, **2**, 2006, 499-509.

[5] Bagchi P., Mesoscale simulation of blood flow in small vessels, *Biophysical Journal*, **92**, 2007, 1858-1877.

[6] Bagchi P., and Kalluri R.M., Dynamics of nonspherical capsules in shear flow, *Phys. Rev. E*, **80**, 2009, 016307.

[7] Beaucourt J., Rioual F., Séon T., Biben T., Misbah C., Steady to unsteady dynamics of a vesicle in a flow, *Phys. Rev. E*, **9**, 2004, 011906.

[8] Biben T., Farutin A., and Misbah C., Three-dimensional vesicles under shear flow: Numerical study of dynamics and phase diagram, *Phys. Rev. E*, **83**, 2011, 031921.

[9] Biben T., and Misbah C., Tumbling of vesicles under shear flow within an advected-field approach, *Phys. Rev. E*, **67**, 2003, 031908.

[10] Blackshear J.P., Forstorm R., Dorman F., and Voss G., Effect of flow on cells near walls, *Federal Proceedings*, **30**, 1971, 1600-1609.

[11] Bruinsma R., Rheology and shape transitions of vesicles under capillary flow, *Phys. A.*, **234**, 1996, 249-270.

[12] Canham P.B., and Burton A.C., Distribution of size and shape in populations of normal human red cells, *Cir.Res.*, **22**, 1968, 405-422.

[13] Chen S.D., Pan T.W., and Chang C.C., The motion of a single and multiple neutrally buoyant elliptical cylinders in plane Poiseuille flow, *Phys. Fluids*, **24**, 2012, 103302.

[14] Chorin A.J., Hughes T.J.R., McCrachen M.F., and Marsden J.E., Product formulas and numerical algorithms, *Communications on Pure and Applied Mathematics*, **31**, 1978, 205-256.

[15] Coupier G., Kaoui B., Podgorski T., and Misbah C., Non-inertial lateral migration of vesicles in bounded Poiseuille flow, *Physics of Fluids*, **20(11)**, 2008, 111702.

[16] Crowl L., and Fogelson A., Computational model of whole blood exhibiting lateral platelet motion induced by red blood cells, *International Journal for Numerical Methods in Biomedical Engineering* , **26**, 2009, 471-487.

[17] Danker G, Vlahovska PM, and Misbah C., Vesicles in Poiseuille flow, *Phys. Rev. Lett.*, **102**, 2009, 148102.

[18] Dean E.J., and Glowinski R., A wave equation approach to the numerical solution of the Navier-Stokes equations for incompressible viscous flow, *C.R. Acad. Sc. Paris, Série 1*, **325**, 1997, 783-791.

[19] Dean E.J., Glowinski R., and Pan T.W., A wave equation approach to the numerical simulation of incompressible viscous fluid flow modeled by the Navier-Stokes equations, In *Mathematical and Numerical Aspects of Wave Propagation*, De Santo JA (Ed.), SIAM: Philadelphia, 1998, 65-74.

[20] Deschamps J., Kantsler V., and Steinberg V., Phase diagram of single vesicle dynamical states in shear flow, *Phys. Rev. Lett.*, **102**, 2009, 118105.

[21] Ding E.J., and Aidun C.K., The dynamics and scaling law for particles suspended in shear flow with inertia, *J. Fluid Mech.*, **423**, 2000, 317-344.

[22] Doddi S.K., and Bagchi P., Lateral migration of a capsule in a plane Poiseuille flow in a channel, *Int. J. Multiphase Flow*, **36**, 2008, 966-986.

[23] Dondorp A.M., Angus B.J., Chotivanich K., Silamut, K., Ruangveerayuth R., Hardeman M.R., Kager P.A., Vreeken J., and White N.J., Red blood cell deformability as a predictor of severe falciparum malaria, *American Journal of Tropical Medicine and Hygiene*, **60-5**, 1999, 733-737.

[24] Dupin M.M., Halliday I., Care C.M., Alboul L., and Munn L.L., Modeling the flow of dense suspensions of deformable particle in three dimensions, *Phys. Rev. E*, **75**, 2007, 066707.

[25] Eggleton C., Popel A., Large deformation of red blood cell ghosts in a simple shear flow, *Phys. Fluids*, **10**, 1998, 1834-1845.

[26] Evans E., and Fung Y.C., Improved measurements of the erythrocyte geometry, *Microvasc. Res.*, **4**, 1972, 335-47.

[27] Farutin A., Biben T., and Misbah C., New analytical progress in the theory of vesicles under linear flow , *Phys. Rev. E*, **81**, 2010, 061904.

[28] Fischer T.M., Stöhr-Liesen M.,and Schmid-Schönbein H., The red cell as a fluid droplet: tank tread-like motion of the human erythrocyte membrane in shear flow, *Science*, **202**, 1978, 894-896.

[29] Fischer T.M., Shape memory of human red blood cells, *Biophys. J.*, **86**, 2004, 3304-3313.

[30] Fotosearch.inc, `http://www.fotosearch.com/photos-images.html`, 1998.

[31] Fung Y.C., Stochastic flow in capillary blood vessels, *Microvasc. Res.*, **5**, 1973, 34-48.

[32] Glowinski R., Finite element methods for incompressible viscous flow, In *Handbook of Numerical Analysis*, Vol. IX, Ciarlet PG and Lions JL (Eds.), North-Holland: Amsterdam, 2003, 7-1176.

[33] Glowinski R., Pan T.W., Hesla T., Joseph D.D., and Periaux J., A fictitious domain approach to the direct numerical simulation of incompressible viscous flow past moving rigid bodies: Application to particulate flow, *J. Comput. Phys.*, **169**, 2001, 363-427.

[34] Goldsmith H.L., Red cell motions and wall interactions in tube flow, *Fed. Proc.*, **30(5)**, 1971, 1578-1590.

[35] Haas K.H., Blom C., Ende D., Duits M.H.G., and Mellema J., Deformation of giant lipid bilayer vesicles in shear flow, *Phys. Rev. E*, **56**, 1997, 7132.

[36] Hathcock J.J. , Flow effects on coagulations and thrombosis, *Arerioscl*erosis, *Thrombosis, and Vascular Biolosy*, **26**, 2006, 1729-1737.

[37] Higgins J.M., Eddington D.T., Bhatia S.N., and Mahadevan L., Sickle cell vasoocclusion and rescue in a microfluidic device, *Proc. Natl. Acad. Sci. USA*, **104**, 2007, 20496-20500.

[38] Ho B.P., and Leal L.G., Inertial migration of rigid spheres in two-dimensional unidirectional flows, *J. Fluid Mech.*, **65**, 1974, 365-400.

[39] Huang S., Pan T.W., Chu C.C., and Chang C.C., The dynamics of a neutrally buoyant particle in a simple shear using DLM/FD method, *in preparation.*

[40] Kaoui B., Biros G., and Misbah C., Why do red blood cells have asymmetric shapes even in a symmetric flow, *Phys. Rev. Lett.*, **103**, 2009, 188101.

[41] Kaoui B., Farutin A., and Misbah C., Vesicles under simple shear flow , *Phys. Rev. E*, **80**, 2009, 061905.

[42] Kaoui B, Harting J, and Misbah C., Two-dimensional vesicle dynamics under shear flow: effect of confinement, *Phys. Rev. E*, **83**, 2011, 066319.

[43] Kaoui B., Kruger T., and Hatting J., How does confinement affect the dynamics of viscous vesicles and red blood cells?, *Soft Matter*, **8(35)**, 2012, 9246.

[44] Kaoui B., Ristow G.H., Cantat I., Misbah C., and Zimmermann W., Lateral migration of a two-dimensional vesicle in unbounded Poiseuille flow, *Phy. Rev. E*, **77(2)**, 2008, 021903.

[45] Kaoui B., Tahiri N., Biben T., Ez-Zahraouy H., Benyoussef A., Biros G., and Misbah C., Complexity of vesicle microcirculation, *Phys. Re. E*, **84**, 2011, 041906.

[46] Kantsler V., and Steinberg V., Transition to tumbling and two regimes of tumbling motion of a vesicle in shear flow, *Phys. Rev. Lett.*, **96**, 2006, 036001.

[47] Karnis A., Goldsmith H.L., and Mason S.G., Axial migration of particles in Poiseuille flow, *Nature*, **200**, 1963, 159-160.

[48] Karnis A., Goldsmith H.L., and Mason S.G., The flow of suspensions through tubes: V. Inertial effects *Can. J. Chem. Eng.*, **44**, 1966, 181-193.

[49] Ko T., Patankar N.A., and Joseph D.D., Lift and multiple equilibrium positions of a single particle in Newtonian and Oldroyd-B fluids, *Computers and Fluids*, **35**, 2006, 121-146.

[50] Keller S.R., and Skalak R., Motion of a tank-treading ellipsoidal particle in a shear flow, *J. Fluid Mech.*, **120**, 1982, 27-47.

[51] Kessler S., Finken R., and Seifert U., Swinging and tumbling of elastic capsules in shear flow, *J. Fluid Mech.*, **605**, 2008, 207-226.

[52] Kim Y., and Lai M.C., Numerical study of viscosity on tank-treading and tumbling motions of vesicles under shear flow, *Phys. Rev. E*, **86**, 2012, 066321.

[53] Li H.B., Yi H.H., Shan X.W., and Fang H.P., Shape changes and motion of a vesicle in a fluid using a lattice Boltzmann model, *Europhysics Letters*, **81**, 2008, 54002.

[54] Lipowsky H., `http://www.bioe.psu.edu/labs/Lipowsky-Lab/red_cell_aggregation.html`, 2010.

[55] Liu Y., Zhang L., Wang X., and Liu W.K., Coupling of Navier-Stokes equations with protein molecular dynamics and its application to hemodynamics, *International Journal for Numerical Methods in Fluids*, **46**, 2004, 1237-1252.

[56] Mader M.A., Vitkova V., Abkarian M., Viallat A., and Podgorski T., Dynamics of viscous vesicles in shear flow, *Eur. Phys. J. E*, **19**, 2006, 389-397.

[57] Mills J.P., Qie L., Dao M., Lim C.T., and Suresh S., Nonlinear elastic and viscoelastic deformation of the human red blood cell with optical tweezers, *Mech. Chem. Biosyst.*, **1(3)**, 2004, 169-180.

[58] Misbah C., Vacillating breathing and tumbling of vesicles under shear, *Phys. Rev. Lett.*, **96**, 2006, 028104.

[59] Mohandas N.,Phillips W.M., and Bessis M., Red blood cell defromability and hemolytic anemias, *Semin. Hematol.*, **16**, 1979, 95-114.

[60] Mortazavi S., and Tryggvason G., A numerical study of the motion of drops in Poiseuille flow. Part 1. Lateral migration of one drop *J. Fluid Mech.*, **vol. 411**, 2000, 325-350.

[61] Noguchi H, and Gompper G., Swinging and tumbling of fluid vesicles in shear flow, *Phys. Rev. Lett.*, **98**, 2007, 128103.

[62] Noguchi H., and Gompper G., Shape transitions of fluid vesicles and red blood cells in capillary flows *PNAS.*, **no.40**, 2005, 14159-14164.

[63] Pamme N., Continuous flow separations in microfluidic devices, *Lab on a chip*, **7**, 2007, 1644-1659.

[64] Pan T.W., and Glowinski R., Direct simulation of the motion of neutrally buoyant circular cylinders in plane Poiseuille flow, *J. Comput. Phys.*, **181**, 2002, 260-279.

[65] Pan T.W., Joseph D.D., Bai R., Glowinski R., and Sarin V., Fluidization of 1204 spheres: simulation and experiments, *J. Fluid. Mech.*, **451**, 2002, 169-191.

[66] Pan T.W., and Glowinski R., Direct simulation of the motion of neutrally buoyant balls in a three-dimensional Poiseuille flow, *C. R. Mecanique*, **333**, 2005, 884-895.

[67] Pan T.W., Shi L., and Glowinski R., A DLM/FD/IB method for simulating cell/cell and cell/particle interaction in microchannels, *Chinese Annals of Mathematics, Series B*, **31**, 2010, 975-990.

[68] Pan T.W., and Wang T., Dynamical simulation od red blood cell rheology in microvessels, *International Journal of Numerical Analysis and Modeling*, **6**, 2009, 455-473.

[69] Peskin C.S., Numerical analysis of blood flow in the heart, *J. Comput. Phys.*, **25**, 1977, 220-252.

[70] Peskin C.S., and McQueen D.M., Modeling prosthetic heart valves for numerical analysis of blood flow in the heart, *J. Comput. Phys.*, **37**, 1980, 11332.

[71] Peskin C.S., The immersed boundary method, *Acta Numer.*, **11**, 2002, 479-517.

[72] Pivkin I.V., and Karniadakis G.E., Accurate coarse-grained modeling of red blood cells, *Phys. Rev. Lett.*, **101**, 2008, 118105.

[73] Popel A.S., and Johnson P.C., Microcirculation and hemorheology, *Annual Review Fluid Mech.* 2005, **37**: 43-69.

[74] Pozrikidis C., Numerical simulation of cell motion in tube flow, *Ann. Biomed. Eng.*, **33**, 2005, 165-178.

[75] Pozrikidis C., Axisymmetric motion of a file of red blood cells through capillaries, *Phys. Fluids*, **17**, 2005, 031503.

[76] Secomb T.W., and Skalak R., A two-dimensional model for asymmetric cell, *Microvasc. Res.*, **24**, 1982, 194-203.

[77] Segré G., and Silberberg A., Radial particle displacements in Poiseuille flow of suspensions *Nature (London)*, **189**, 1961, 209-210.

[78] Segré G., and Silberberg A., Behavior of macroscopic rigid spheres in Poiseuille flow, Part 1, *J. Fluid. Mech.*, **14**, 1962, 115-135.

[79] Segré G., and Silberberg A., Behavior of macroscopic rigid spheres in Poiseuille flow, Part 2, *J. Fluid. Mech.*, **14**, 1962, 136-157.

[80] Shi L., Pan T.W., and Glowinski R., Numerical simulation of lateral migration of red blood cells in Poiseuille flows, *Int. J. Numer. Meth. Fluids*, **68**, 2012, 1393-1408.

[81] Shi L., Pan T.W., and Glowinski R., Deformation of a single red blood cell in bounded Poiseuille flows, *Phys. Rev. E*, **85**, 2012, 016307.

[82] Shi L., Pan T.W., and Glowinski R., Lateral migration and equilibrium shape and position of a single red blood cell in bounded Poiseuille flows, *Phys. Rev. E*, **86**, 2012, 056308.

[83] Shin S.J., and Sung H.J., Inertial migration of an elastic capsule in a Poseuille flow, *Phys. Rev. E*, **83**, 2011, 046321.

[84] Skalak R., and Branemark P.I., Deformation of red blood cells in capillaries, *Science*, **164**, 1969, 717-719.

[85] Sui Y., Chew T., Roy P., Cheng Y.P., and Low H.T., Dynamic motion of red blood cells in simple shear flow, Dynamics of vesicles in shear and rotational flows: Modal dynamics and phase diagram, *Phys. fluids*, **20**, 2008, 112106.

[86] Sui Y., Low H.T., Chew Y.T., Roy P., Tank-treading, swinging, and tumbling of liquid-filled elastic capsules in shear flow, *Phys. Rev. E.*, **77**, 2008, 016310.

[87] Sung A., and Skelton R., `http://www.jacobsschool.ucsd.edu/news/news_releases/release.sfe?id=484`, 2005.

[88] Tomaiuolo G., Preziosi V., Simeone M., Guido S., Ciancia R., Martinelli V., Rinaldi C., and Rotoli B., A methodology to study the defromability of red blood cells flowing in microcapillaries *in vitro*, *Ann. Ist. Super. Sanita*, **43**, 2007, 186-192.

[89] Tsubota K., Wada S., and Yamaguchi T., Simulation study on effects of hematocrit on blood flow properties using particle method, *J. Biomech. Sci. Eng.*, **1**, 2006, 159-170.

[90] Tsukada K., Sekizuka E., Oshio C., and Minamitani H., Direct measurement of erythrocyte deformability in diabetes mellitus with a transparent microchannel capillary model and high-speed video camera system, *Mirovasc. Res.*, **61**, 2001, 231-239.

[91] Wada S., and Kobayashi R., Numerical simulation of various shape changes of a swollen red blood cell by decrease of its volume, *Trans. JSME. Ser. A*, **69**, 2003, 14-21.

[92] Wang C.H., Popel A.S., Effect of red blood cell shape on oxygen transport in capillaries, *Math. Biosci.*, **116**, 1993, 89.

[93] Yoshino M., and Murayama T., A lattice Boltzmann method for a two-phase flow containing solid bodies with viscoelastic membranes, *Eur. Phys. J. Special. Topics*, **171**, 2009, 151-157.

[94] Zabusky N.J., Segre E., Deschamps J., Kantsler V., Steinberg V., Dynamics of vesicles in shear and rotational flows: Modal dynamics and phase diagram, *Phys. fluids*, **23**, 2011, 041905.

[95] Zettner C.M., and Yoda M., Moderate-aspect-ratio elliptical cylinders in simple shear with inertia, *J.Fluid Mech.*, **442**, 2001, 241-266.

[96] Zhang J., Johnson P.C., and Popel A.S., Effects of erythrocyte deformability and aggregation on the cell free layer and the apparent viscosity of microscopic blood flows, *Microvascular Research*, **77**, 2009, 265-272.